Dissertation
submitted to the
Combined Faculties of the Natural Sciences and Mathematics
of the Ruperto-Carola-University of Heidelberg, Germany
for the degree of
Doctor of Natural Sciences

Put forward by
Thomas Beyer
born in Leipzig

Oral examination: 26.11.2014

Installation and operation of a
radio-frequency quadrupole cooler and buncher
and offline commissioning of the TRIGA-SPEC
ion beam preparation transfer line

Referees: Prof. Dr. Klaus Blaum
Priv.-Doz. Dr. José Crespo

Installation und Betrieb eines Radiofrequenzquadrupol-Kühlers und Inbetriebnahme der Strahlstrecke zur Ionenaufbereitung von TRIGA-SPEC:

Der Großteil der Elemente, die schwerer sind als Eisen, wurde durch Neutroneneinfangreaktionen in stellarer Nukleosynthese erzeugt. Die Isotopenstruktur dieser Elemente trägt die Spuren der beteiligten Erzeugungsprozesse, und eine große Menge experimenteller Daten ist nötig um deren astrophysikalische Berechnung und Modellierung zu ermöglichen.
Das Ziel des TRIGA-SPEC-Experiments ist, zur Erhebung dieser Daten durch die Messung der Grundzustandseigenschaften neutronenreicher schwerer Nuklide beizutragen. Dazu gehören das Penningfallen-Massenspektrometer TRIGA-TRAP zur Bestimmung von Massen, Q-Werten und Bindungsenergien, sowie der kollineare Laserspektroskopieaufbau TRIGA-LASER zur Bestimmung von Ladungsradien, Kernspins und -momenten. Die gewünschten Nuklide werden im Forschungsreaktor TRIGA Mainz durch die neutroneninduzierte Spaltung eines Actinidentargets erzeugt und in einer on-line Ionenquelle ionisiert.
Im Rahmen dieser Arbeit wurden die beiden Experimente an den Forschungsreaktor angeschlossen, und die Strahlstrecke zur Ionenaufbereitung vervollständigt. Dazu gehörten die Installation und der Betrieb eines Radiofrequenzquadrupols zur Emittanzreduzierung und Akkumulierung der Ionen. Mit erfolgreichen Testmessungen an stabilen Nukliden, die in der on-line Ionenquelle erzeugt wurden, wurde die Funktionalität der Ionenaufbereitung überprüft und bestätigt.

Installation and operation of a radio-frequency quadrupole cooler and buncher and offline commissioning of the TRIGA-SPEC ion beam preparation transfer line:

The dominant fraction of elements heavier than iron was created in stellar nucleosynthesis by neutron-capture reactions. The isotopic compositions of these elements are the fingerprints of the involved processes, and a huge amount of experimental data on these isotopes is required to support corresponding astrophysical calculations and models.
The TRIGA-SPEC experiment aims to contribute to these data by the measurement of ground-state properties of neutron-rich heavy nuclides. It consists of the Penning-trap mass spectrometer TRIGA-TRAP for the determination of masses, Q-values and binding energies, and the collinear laser spectroscopy setup TRIGA-LASER for the determination of charge radii, nuclear spins, and moments. The nuclides of interest are produced by neutron-induced fission of an actinide target inside the research reactor TRIGA Mainz and ionized in an online ion source.
In the context of this thesis, the two experiments were coupled to the reactor, completing the ion beam preparation transfer line. This included the implementation and commissioning of a radio-frequency quadrupole for the emittance reduction and accumulation of the ions. The functionality of the ion beam preparation was verified by successful test measurements of stable nuclides produced in the online ion source.

The wonder is, not that the field of stars is so vast,
but that man has measured it.

Anatole France

Contents

List of Figures

Introduction

The universe is composed of a great variety of elements and their isotopes [BBFH57]. The diverse processes by which these elements were formed and how they contribute to the elemental composition observed in nature is the subject of nuclear and astrophysics. The primordial concentration of the lightest species (^{1,2}H, ^{3,4}He, and ^{7}Li) was synthesized during the cosmological Big Bang [BS85], their interaction with cosmic rays yielded ^{6}Li and ^{9,10,11}Be. The dominant fraction of the heavier elements was produced in stellar nucleosynthesis. The elements up to iron and nickel are mainly the result of charged-particle thermonuclear reactions in stars, or explosive charged-particle nucleosynthesis through the shock heating of supernovae [WW86]. Characterized by the highest binding energies per nucleon, nuclei around iron are the most stable, impeding charged-particle-induced fusion reactions by increasing Coulomb barriers [CTT91]. The observed existence of elements heavier than iron thus implies mechanisms involving neutron-capture reactions[1].

There are two distinct neutron-capture processes responsible for the production of the heavy nuclei: the s-process and the r-process, each of which contributed approximately half to the total amount of stable nuclei above iron [AG89]. In the s- (or *slow*) neutron-capture process, a neutron is captured by an atomic nucleus at a rate that is low compared to the rate of the subsequent β^- decay which increases the atomic number by one. Hence, the path of the s-process moves along the valley of β-stable nuclides [KBW89]. In contrast, the r- (or *rapid*) process operates in an environment of a much higher neutron flux (e.g., a supernova), where the rate of neutron capture greatly exceeds the β decay rate. Thus, the r-process path is located well off the β-stable valley in the neutron-rich region of the chart of nuclides. When the neutron flux is exhausted during the process, stable neutron-rich nuclides that lie off the s-process path like, e.g., ^{96}Zr, ^{130}Te, or ^{186}W can be produced. More generally spoken, the isotopic compositions, especially of the heavy elements, are the "prime fingerprints" of astrophysical nucleosynthesis processes [AGT07].

So far, the exact path of the r-process is not identified yet – moreover, the number of possible r-process nuclides is not clarified [QW07]. Given the variety of available r-process studies, a huge body of nuclear data are potentially needed for the verification or falsification of r-process nucleosynthesis predictions. This includes static properties like masses, matter and charge distributions, and single-particle spectra as well as decay characteristics and reactivity [AGT07]. In recent years, a major effort was put into the measurement of relevant nuclear data by quite a number of

[1] Proton-capture processes running in certain environments, e.g., the rp-process at temperatures above 10^9 K in neutron stars, contribute poorly to the observed elemental composition [SAB$^+$01, TGA$^+$04]

facilities worldwide. In particular, the installation of Penning-trap and storage-ring based mass spectrometers (for masses, Q-values, binding energies) and collinear-laser-spectroscopic installations (for charge radii, nuclear spins and moments, deformation) at the sites of radioactive ion beam facilities led to significant contributions to the required nuclear data [BDN13].

TRIGA-SPEC, installed at the research reactor TRIGA Mainz at the Institute of Nuclear Chemistry of the Johannes Gutenberg University of Mainz, is such an experiment. With new experimental techniques being developed and implemented at TRIGA-SPEC, it acts as a test setup for the MATS and LaSpec experiments at the future FAIR facility [RBN$^+$10]. TRIGA-SPEC consists of the Penning-trap mass spectrometer TRIGA-TRAP and the collinear laser spectroscopy beam line TRIGA-LASER [KKB$^+$08]. Access to neutron-rich nuclides in between the valley of stability and the neutron-dripline is provided by neutron-induced fission of an actinide target (^{235}U, ^{252}Cf) inside the TRIGA reactor core. In addition, elements above uranium can be accessed by the use of various offline sources [SBB$^+$12, EBB$^+$14]. Most notably, TRIGA-SPEC is the only experiment of that kind in the world which is connected to a nuclear reactor. The extraction and preparation of the nuclides of interest are performed by the ion beam preparation transfer line, which is shared by the experimental branches. It involves a gas-jet system to transport the fission products through the biological shield of the reactor, an ion source to ionize the fission products, a dipole magnet for mass separation, and a radio-frequency quadrupole (RFQ) cooler and buncher.

The latter is employed to transform specific properties of the ion beam, such as the energy spread and the temporal structure, in order to match the specific requirements of the experiments. The technique was introduced for the manipulation of radioactive ion beams for the first time at the ISOLTRAP experiment in 2000 [HDK$^+$01]. Because the application of gas-filled RFQs for the accumulation and emittance reduction of ions impressively increased the sensitivity of mass spectrometry and laser spectroscopy [NCB$^+$02], these devices were put into operation at various experimental sites (JYFL, ISOLDE, TRIUMF, SHIPTRAP). In the course of this thesis, an RFQ was incorporated at the TRIGA-SPEC experiment and upgraded with the ability to create ion bunches for the experiments. Chapter 1 covers the theoretical background on emittance reduction techniques and the RFQ, Chap. 2 shows the TRIGA-SPEC setup, the commissioning of the RFQ is presented in Chap. 3. Finally, test measurements at TRIGA-LASER and TRIGA-TRAP to verify the functionality of the ion beam preparation transfer line are presented.

1 Theory

1.1 Emittance of particle ensembles

The emittance is, besides brilliance, widely used in particle physics to embody information about the quality of a particle beam or ensemble. The condensation of quantities like momentum or energy spread into a single measure has the advantage of easy comparability, e.g., when relating it to the acceptance of experimental systems. In this chapter, the concept of phase space will be explained briefly to introduce the emittance term and to show how it reflects the actual properties of particle beams or ensembles. A comprehensive guide to the description of charged particle motion with the concept of phase space can be found in, e.g., the paper by Moore [Moo93], which the introduction will follow partly, or more elaborate in the book by Wollnik [Wol87].

1.1.1 The theorem of Liouville

A particle's kinematics are fully described by its coordinates and momentum in 3D space, defining its position in the so-called "phase space" in the canonical description. By knowing the complete set of a particle's phase space coordinates and acting forces at a certain time, its evolution in time can be calculated analytically (in both directions of time). An ensemble of particles defined by a coordinate and momentum distribution occupies a certain volume in phase space. Since the coordinate and momentum distributions are both three-dimensional, the occupied phase space volume is six-dimensional and the dynamics are described by the motion of the volume in phase space. This concept is particularly useful when describing the transport of a particle ensemble through a set of electromagnetic fields, e.g., in and out of electromagnetic traps or through beam lines. Usually, the transport time is sufficiently short so that particle-particle interactions like Coulomb repulsion are insignificant related to the effects of the applied electromagnetic fields. In this case, it can be shown that the phase space volume of a particle ensemble under the effect of conservative force fields is constant in time (e.g., [Sch06]). This is the statement of the classical theorem of Liouville, which can be expressed in a more generalized way as the preservation of the phase space density [Sch07]:
The time evolution of the occupied phase space volume of a canonical system can be pictured as the flow of an incompressible fluid.
For the particle transport through beam lines, the applied fields mostly result in linear equations of motion. These include the fields of quadrupole traps, uniform magnetic fields, and deceleration, injection and extraction optics [Moo93]. Since the

particle's motion is independent in the three projections of the phase space, each projection can be treated separately. The theorem of Liouville then applies to each 2D phase space separately, preserving their phase space density. An example of such a 2D projection, or "action diagram" (as the area in such a diagram has the units of action, i.e., momentum×displacement or energy×time), is illustrated in Fig. 1.1. It

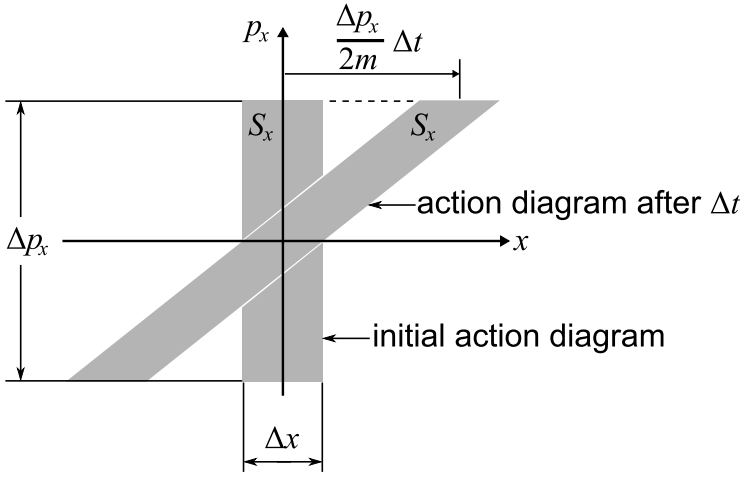

Figure 1.1: Action diagram in the (p_x, x)-plane for a ensemble of particles with mass m moving freely through space, without forces acting on it. With time, the position coordinate x of the particles changes due to their initial momentum p_x. Although the shape of the occupied phase space volume has changed, its area S_x is preserved.

shows an ensemble of identical particles with position spread Δx around the origin, which are moving freely in space with momentum distribution Δp_x around zero central momentum. For simplification, the ensemble initially occupies a rectangular phase space volume with area S_x. After a time Δt, the momentum is unchanged, but the particles moved in space by the product of their velocities and time,

$$x = \frac{p_x}{m}\Delta t. \tag{1.1}$$

The particle ensemble will then fill the parallelogram shown in the figure, that has the same area as the rectangle. Although the spatial volume of the particle ensemble has expanded during Δt, its action area is preserved. This applies in the same way to the coordinate planes of (p_y, y) and (p_z, z), preserving the complete 6D phase space volume, which is the product of the three action areas.

1.1.2 Transverse and longitudinal emittance

The emittance of a moving particle ensemble is defined independently for each phase space projection, but not equal to the preserved action area. Since there are three independent phase spaces, there are also three independent emittance measures,

two transverse (ε_x, ε_y) and one longitudinal (ε_z) with respect to the propagation direction of the particle ensemble.
For the description of a moving beam of particles, a central momentum p_0 in one of the position coordinates, typically z, is added to the definition. The momentum distribution Δp_z is then centered around the central momentum p_{z0}. The parallelogram in the (p_z, z) action diagram will additionally move to the right by the amount $z{=}p_{z0}\Delta t/m$. The action diagrams of (p_x, x) and (p_y, y), describing the transverse action of the particle ensemble, remain unchanged. The focal point of a particle beam propagating in z corresponds to the transverse action diagrams with the lowest position spread (in Fig. 1.1, this would be the initial configuration), as the "widths" of the beam Δx and Δy are minimal. Furthermore, this is the only configuration where the action area is symmetrical in p.
For the characterization of fast beams, the transverse momentum p_x (same holds for p_y) is usually expressed as angular divergence:

$$x' = \frac{p_x}{p_{z0}} = \tan\Phi_x \cong \Phi_x \text{ for small } \Phi_x, \tag{1.2}$$

and the unit is milliradians. Phase space diagrams defined by position spread and angular divergence are called "emittance" diagrams, and the corresponding phase space volume is called the beam "emittance", given in units of mm mrad. The transverse action area S_x is related to the transverse emittance ε_x by

$$S_x = p_{z0}\varepsilon_x. \tag{1.3}$$

Although it is instructive to describe a particle ensemble with a parallelogram, the realistic shape of the beam's phase space volume is typically elliptic, as shown in Fig. 1.2. The emittance of a beam is then given in units of πmm mrad, as the area of an ellipse is π times the semi-major and semi-minor axes.

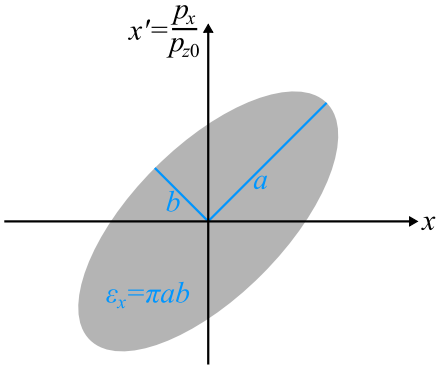

Figure 1.2: Emittance ellipse in the (x, x') phase space. The semi-major and semi-minor axes are labeled a and b, respectively.

The value of the transverse emittance defined in this way is inversely proportional to the forward momentum p_{z0}. Thus, it is not preserved when the particles' longitudinal

velocity v_z is changed. To keep the concept of a conserved emittance, the so-called "normalized" emittance ε_n is usually used in ion source and accelerator designs. It relates to the previously defined emittance ε as [WLL01]

$$\varepsilon_\mathrm{n} = \gamma\beta\varepsilon, \text{ with } \beta = \frac{v_z}{c}, \tag{1.4}$$

and $\gamma{=}1/\sqrt{1-\beta^2}$ being the relativistic Lorentz factor. The action area S can then be expressed in terms of the normalized emittance as

$$S = m_0 c \varepsilon_\mathrm{n}, \tag{1.5}$$

where m_0 is the rest mass of the beam particles and c denotes the speed of light.

When dealing with particle pulses rather than continuous beams, a phase space which is representing longitudinal beam properties is preferred. The axes of the action diagram can be displayed as forward momentum×longitudinal displacement (p_z, z) or energy×time (E, t). For longitudinal beam pulses, in the (E, t) phase space, the units are eVµs. For direct comparison, Fig. 1.3 shows the (p_z, z) and (E, t) action diagrams for the case of a particle pulse that undergoes a longitudinal or "time" focus. At the focal point, the position spread Δz is minimal, resulting in the shortest length of the pulse Δt. Before the focal point, particles that are behind (lower z or higher flight time t) have a higher momentum p_z or energy E. These particles catch up with the others in the focal point and advance past the slower ones at a later time (shown on the right). At the position of the time focus, the longitudinal emittance ε_z is just the product of the energy and time spread of the particle pulse (multiplied by $\pi/4$ as the emittance has an elliptic shape):

$$S_z = \varepsilon_z = \frac{\pi}{4}\Delta E \Delta t. \tag{1.6}$$

For typical beam transports, the central momentum greatly exceeds the momentum spread and the action areas of both diagrams are equal. The relations

$$\Delta E = v_{z0}\Delta p_z;\ \Delta t = \frac{\Delta z}{v_{z0}} \implies \Delta E \Delta t = \Delta p_z \Delta z \tag{1.7}$$

are obtained for non-relativistic velocities [Moo93], with the central velocity v_{z0} of the particle pulse. Using electromagnetic beam manipulation tools like benders, deflectors, or lenses, one can reduce the energy spread of a particle pulse, but only at the expense of its time spread. The action area is conserved, so in principle a particle pulse with a longitudinal emittance of 4 eVµs can be stretched into a 4 µs-long pulse with 1 eV energy spread, or condensed into a 1 µs-long pulse with 4 eV energy spread.

In general, an efficient transmission of a particle ensemble through a beam line requires that the emittance of the ensemble does not exceed the acceptance of each beam line's component. The acceptance is defined in the same way as the emittance and describes the necessary shape of the phase space volume for the transmission

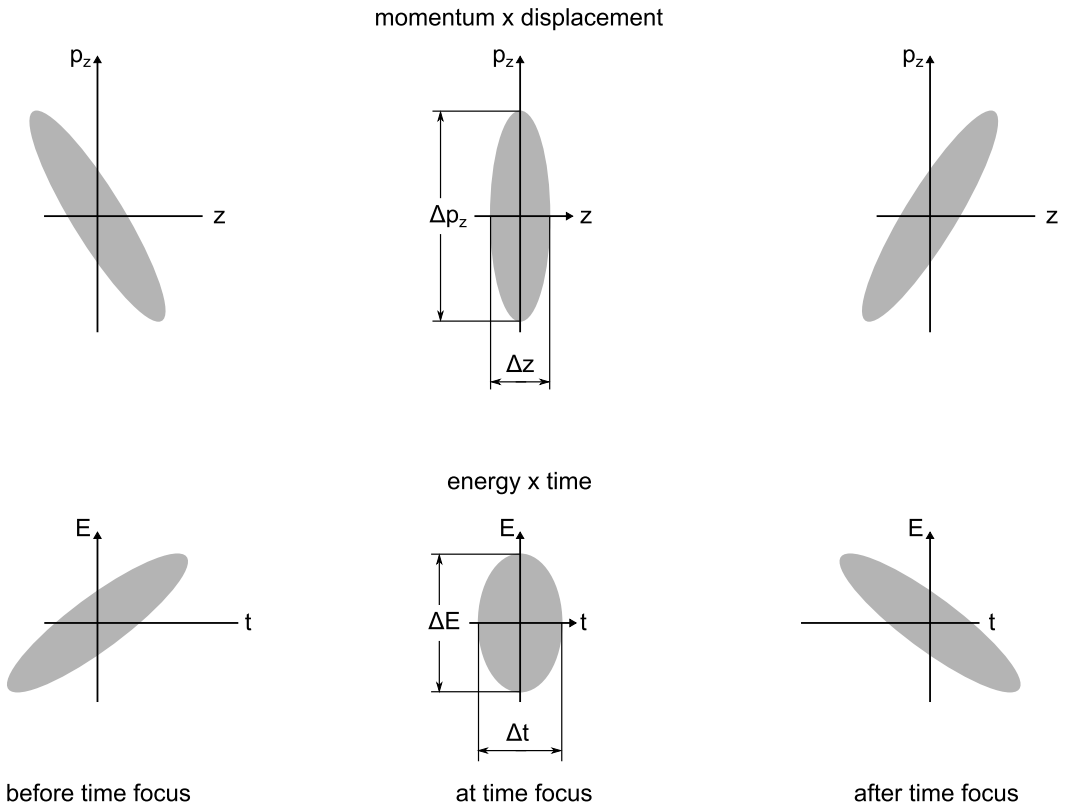

Figure 1.3: Action diagrams for a particle ensemble undergoing a longitudinal (or time) focus. The top diagrams are in the momentum×displacement phase space, and the bottom diagrams show the corresponding energy×time phase space. At the focal point, the two action areas are identical and can be converted into one another (see the text for details).

through that component. For the injection into a Penning trap, it is desirable to form a very short pulse, while a slightly higher energy spread can still be accepted. In contrast, collinear laser spectroscopy could handle longer pulses, but the sensitivity depends critically on the energy spread of the pulse (see Sec. 2.4.1).

1.1.3 Initial emittances of commonly used ion sources

For comparison, typical transverse emittances of commonly utilized ion sources at different facilities worldwide are summarized in Tab. 1.1. Unfortunately, the emittances are not always defined in the exact same way. While it is possible to translate emittances at certain particle energies into normalized emittances, there are differences in the fractions of particles that were counted into the position and angular distributions. The deviations to the action area can be quite significant, dependent on whether e.g. the root mean square, 95%, or 90% of the particles are taken into account. Thus, the emittance is shifted to a statistical measure. Nevertheless, the table provides a firm overview of what can be achieved by today's ion sources.

Experimental Site	**Type of ion source**	**Element**	$\varepsilon_n[\pi\text{mm mrad}]$	$\varepsilon[\pi\text{mm mrad}]$	**Ref.**
LBNL, California/US	AECR-U IS, ECR plasma	O^+	0.1_{rms}		[WLL01]
	VENUS ECR IS	Bi^{23+}-Bi^{41+}	0.08_{rms}		[LLA+05]
	Vacuum arc IS	Gd^{2+}	0.3_{rms}		[LQG+98]
ISOLDE/CERN, Switzerland	Surface ionization IS	K^+	$0.02_{95\%}$	$12\text{-}14_{95\%,30\text{keV}}$	[WLL03]
	Plasma IS	K^+	$0.01_{95\%}$	$8\text{-}10_{95\%,30\text{keV}}$	[WLL03]
	Resonance-ion. laser IS	K^+	$0.02_{90\%}$	$17.6_{90\%,20\text{keV}}$	[LBB+09]
	Resonance-ion. laser IS	Cu^+	$0.01_{90\%}$	$7.5_{90\%,20\text{keV}}$	[LBB+09]
FRL, Canada	Laser desorption IS	C_2^+	0.05		[CBD+93]
SPIRAL2, France	ECR charge breeder	Zn^{11+}	$0.01_{90\%}$	$10_{90\%,19.5\text{keV}}$	[LGST06]
TRIUMF, Canada	ECR IS "Phoenix"	Ar^{11+}	$0.02_{90\%}$	$15\text{-}20_{90\%,15\text{keV}}$	[ABB+06]

Table 1.1: Transverse emittances of various ion sources. Values in blue are calculated from the values given in the references to allow easy comparability.

1.2 Emittance reduction techniques

Liouville's theorem states that the phase space volume of a particle ensemble remains constant under the effects of conservative force fields. As a consequence the phase space volume, representing the action area or normalized emittance of an ion ensemble, can not be reduced by means of ion optical elements. Still, there is a fundamental need for emittance reduction to optimize overall experimental efficiencies and to enable studies on scarce elements. Over the last decades, a handful of techniques have been developed which address this requirement. One can also speak of the thermal energy (in units of eV) or translation temperature (in units of K) of an ion ensemble to reflect the ions' mean velocity in the three spatial directions, defined by [Dem96]

$$\frac{1}{2}m\bar{v^2} = \frac{3}{2}k_{\mathrm{B}}T, \tag{1.8}$$

where k_{B} denotes the Boltzmann constant. Emittance reduction techniques are known as "cooling" techniques as they are decreasing the temperature of the ion ensemble. This chapter provides an overview of feasible cooling techniques that are applicable to, though not exclusively, trapped ions. Overviews of different cooling techniques can be found in, e.g., [BLP+88, IBBW95].

1.2.1 Electron cooling

Electron cooling was first proposed by Budker in 1966 [Bud67]. It was realized ten years later at the NAP-M apparatus in Novosibirsk, where a proton beam in a storage ring was cooled with electrons showing results beyond expectation [BS78]. The technique was so powerful that it quickly spread to Europe and USA to cool proton beams at CERN and FNAL [BCH+81, EKK+83]. Most notably, a second-generation electron cooling device facilitated the production and accumulation of antiprotons at the Low-Energy Antiproton Ring (LEAR) at CERN [HPS+88]. The same technique was applied in a Penning trap shortly after by Gabrielse *et al.* to cool antiprotons below 100 meV [GFO+89]. Nowadays, electron coolers are implemented at a number of storage rings worldwide, e.g., at the TSR in Heidelberg [HBB+89], the CRYRING in Stockholm [AAB+93], the ESR in Darmstadt [SBB+04], or the HIRFL cooling storage ring in Lanzhou [ZXX+10], and are used for atomic, nuclear, medium-energy and heavy-ion physics.

A thorough review explaining the theory and many applications was given by Poth [Pot90]. In principle, the mechanism behind electron cooling is equivalent to the cooling of the hotter species in a two-component plasma [Spi56]. Hence, the cooling of an ion beam circulating in a storage ring is achieved by overlapping the (hot) ion beam with a cold electron beam in a section of the ring. The requirements for effective cooling are a high density and a narrow velocity distribution of the electrons. A typical setup of an electron cooler attached to a storage ring is shown in Fig. 1.4. A heated cathode continuously produces electrons, which are

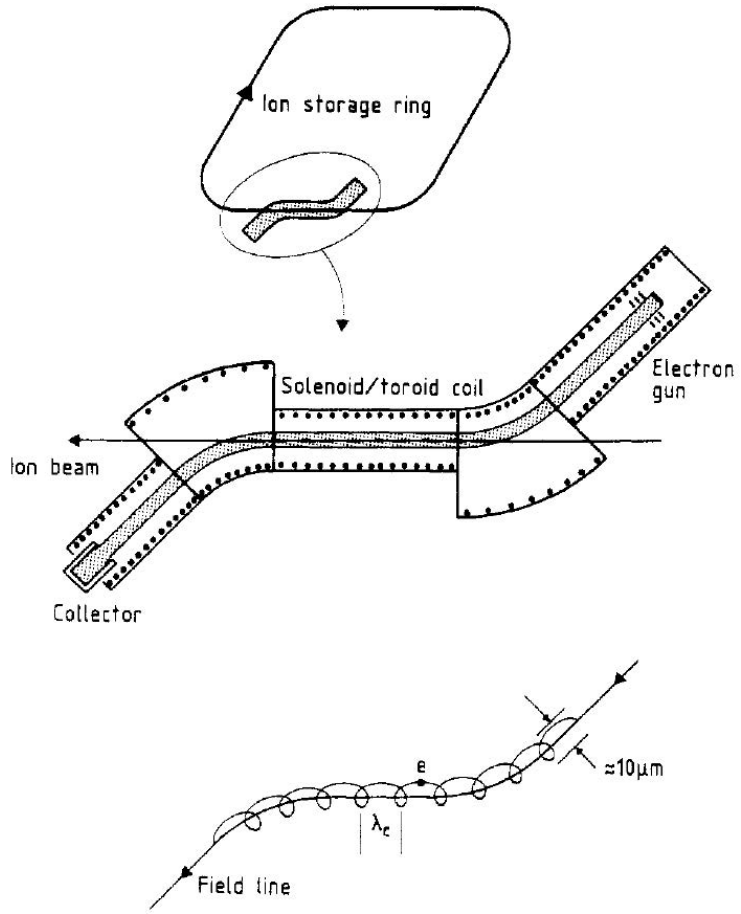

Figure 1.4: Principle of electron cooling in storage rings, taken from [Wol88]. Typical magnetic field strengths are in the order of 0.05 T, and the radius of the electrons' helical motion due to their cyclotron frequency ν_c is around 10 μm. Bottom: the pitch of the helix $\lambda_c = \gamma\beta_0 c/\nu_c$ has to be small compared to the magnetic field curvature for an efficient electron transport.

electrostatically accelerated such that their average velocity $v_0 = \beta_0 c$ matches the circulating ions' velocity. The electron beam transport is realized by a longitudinal magnetic field starting coaxial with the accelerating optics, ensuring high density and small velocity deviations. This is ideally achieved by a toroidal coil that guides the electrons in, through, and out of the storage ring section. In the overlap region, the ions traverse the parallel electron beam under different angles and velocities. Observed from the frame moving with the electrons' velocity, the electrons are at rest and the ions' motion is similar to that of a hot gas: moving in any direction with a variety of velocities. The ion's temperature can be associated with the width of their velocity distribution, which is reduced by Rutherford scattering with the electron "gas". Thus, motional energy is transferred from the ions to the electrons, which are continuously renewed. After a number of cycles, the ions are cooled to

the initial temperature of the electrons. The relaxation time constant was derived by Spitzer [BAB+04],[Spi56]

$$\tau_{\mathrm{i}} = \frac{3 m_{\mathrm{e}} m_{\mathrm{i}} c^3}{8\sqrt{2\pi} n_{\mathrm{e}} Z^2 e^4 L_{\mathrm{C}}} \left(\frac{kT_{\mathrm{e}}}{m_{\mathrm{e}} c^2} + \frac{kT_{\mathrm{i}}}{m_{\mathrm{i}} c^2} \right)^{\frac{3}{2}}, \tag{1.9}$$

where kT_{i} and kT_{e} are the ion and electron energies, respectively, n_{e} is the electron density and L_{C} denotes the Coulomb logarithm[1]. Spitzer calculated the equilibration time for the mixing of two one-component plasmas with different temperatures, long before the development of electron cooling. It can be seen from the equation that the cooling is increasingly efficient for lower kinetic energies, and the proportionality of τ_{i} to Z^{-2} favors high ion charge states.
The heat exchange between hot ions and cold electrons with this technique can also be applied to ions inside traps. The mean velocity of trapped ions is usually around zero, so the electrons do not need to be accelerated anymore. However, the electrons having negative sign of charge have to be loaded into the same trap as the (typically) positive ions to generate a region of overlap. Another challenge arises from the fact that life- and interaction times are much higher, resulting in electron capture as an increasingly important loss mechanism for the ions. The first problem can be solved by the use of nested traps, where the coolant is kept in a smaller trap that is located inside a bigger trap confining the hot ions. To avoid electron capture processes in positive ions, positrons instead of electrons could be used. Unfortunately, the creation of positrons is more complex and expensive than the creation of electrons. Figure 1.5 shows the electric potentials for a nested Penning trap in the case of unlike charges. The Penning trap consists of a longitudinal magnetic field $\vec{B}$ for

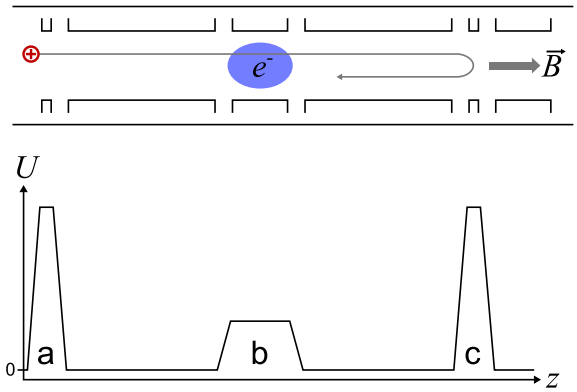

Figure 1.5: Concept of nested Penning traps for the application of electron cooling for trapped ions.

radial confinement and static electric potentials for axial trapping (for more details

[1]The Coulomb logarithm is the ratio of the maximum impact parameter $b_{\max}$ to the classical distance of closest approach $b_{\min}$ in Coulomb scattering, L_{C}=ln($b_{\max}/b_{\min}$). Typically L_{C}≈10–20 [Hub94]

on Penning traps, see chapter 2.3). The cooling process for an ion bunch starts by loading cold electrons into the center trap (position (b) in the figure). Thereby, the electric potential at position (a) has to be lowered. As a next step, the hot ion bunch is injected into the trap, and gets reflected at the exit electrode at position (c). Before the ions can leak out of the trap at its entrance, the potential at (a) is biased. The two species are now completely confined: the electrons within the length of the center electrode (b), and the ions in between the electrodes (a) and (c). The hot ions traverse the cold electron cloud and are cooled. When their longitudinal temperature decreases below the value corresponding to the central electrode's potential, they will no longer pass through the electron cloud. At this point, the potential at the central electrode is lowered by a small fraction, having two effects: the ions can again interact with the electrons, and the hotter electrons escape the trap, thereby cooling the electron cloud (evaporative cooling, see chapter 1.2.2). The decrease of the central electrode's potential is continued until all the electrons are evaporated from the trap, and only the cold ions remain. Penning traps typically use magnetic fields in the order of a few Tesla, therefore electrons are automatically cooled by the emission of synchrotron radiation. The feasibility of cooling highly charged ions (HCI) with electrons was theoretically described by Bernard *et al.* [BAB$^+$04], and an experiment for the cooling of HCI with positrons was developed at RIKEN [OKN$^+$03]. So far, electron cooling in traps has not achieved the "breakthrough" results it brought to storage rings, possibly due to complex mechanisms behind the simultaneous trapping of two species in a Penning trap. However, a "cooler Penning trap", which is a 400-mm long cyclindrical Penning trap consisting of 21 inner electrodes to allow the formation of nested traps, is presently under commissioning at HITRAP/GSI [KBB$^+$08]. Inside Paul traps, electrons and (heavy) ions can not be trapped simultaneously due to different trapping frequencies, so different cooling techniques are favored for trapped ions.

1.2.2 Evaporative cooling

Evaporative cooling can be applied only to trapped particles. A trapped ensemble of particles with a velocity distribution corresponding to its temperature can be cooled by the selective removal of its hottest fraction, i.e., the particles with the highest translational energy. After re-thermalization of the remaining particles through elastic collisions inside the ensemble, a lower mean temperature is reached. The removal is repeated until the ensemble is cooled to the desired temperature or until the lower limit of required particles has been reached. This technique is applicable to a wide range of temperatures, but it requires high initial ion numbers since the cooling is achieved through a substantial loss of particles. It was initially used to cool neutral hydrogen atoms [MDS$^+$88]. However, the cooling process is enhanced in the case of charged particles, as the evaporation and re-thermalization are driven by the Coulomb interaction with its long-range nature. The results are much higher collision rates and thus more efficient cooling in comparison to neutral particles. It is especially favorable to cool highly-charged ions as the collision strength is

proportional to the quadratic charge state which was shown in [LMH+88, PBL+91, KCO01, HSS+11]. Besides laser cooling, evaporative cooling was one of the key techniques to achieve Bose-Einstein Condensation (BEC) [AEM+95, DMA+95], for which Eric A. Cornell, Wolfgang Ketterle, and Carl E. Wieman received the Nobel prize in Physics in 2001 [CKW01]. Recently, the ALPHA Collaboration reported on the evaporative cooling of antiprotons at CERN [AABR+10]. Evaporative cooling has also been applied to Penning traps during the last two decades, e.g., at the SMILETRAP experiment [HSS+11].

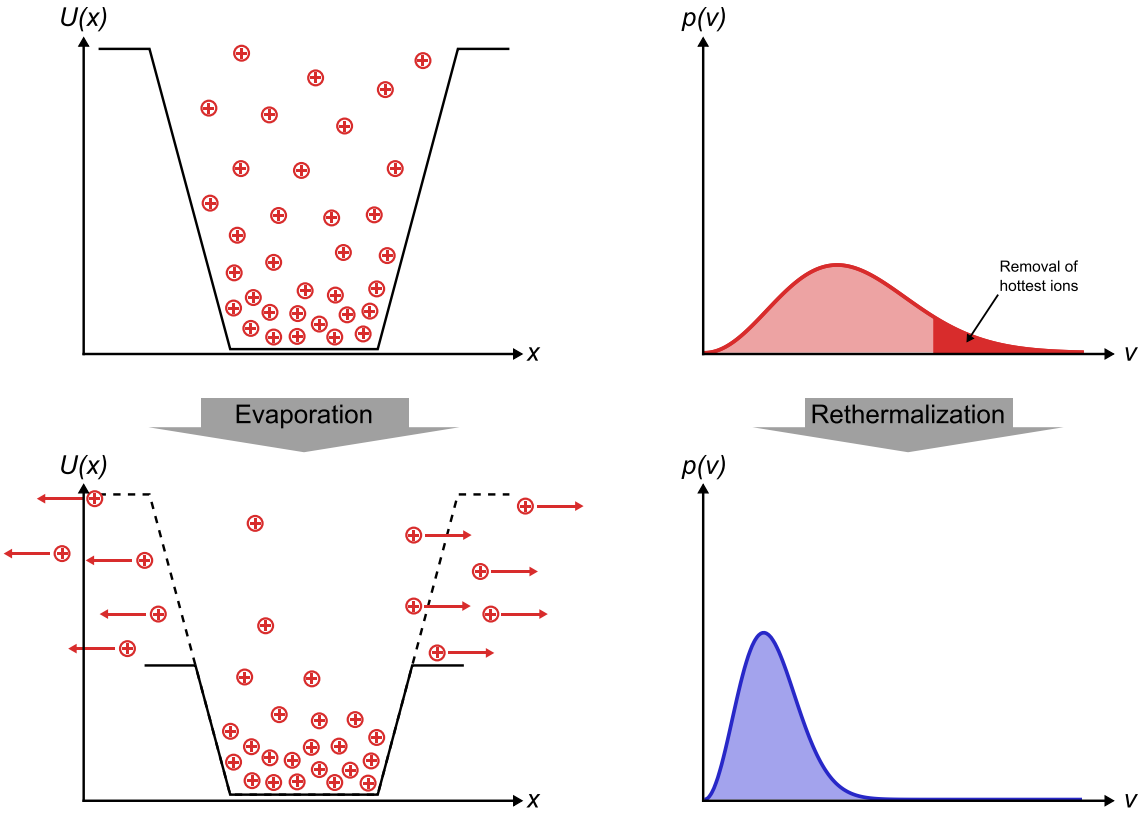

Figure 1.6: Principle of evaporative cooling. For details, see the text.

Figure 1.6 shows the principle of evaporative cooling in the simple case of an ensemble of singly-charged ions trapped inside an electric potential $U(x)$. The ions are thermalized through collisions and their velocity is described by a Maxwell-Boltzmann distribution

$$p(v) = 4\pi \sqrt{\left(\frac{m}{2\pi k_{\mathrm{B}} T}\right)^3} v^2 e^{-\frac{mv^2}{2k_{\mathrm{B}}T}}, \tag{1.10}$$

which is a probability function for the absolute value of the ion's velocity v. After lowering the confining potential $U(x)$, the most energetic particles will leave the trap, and the remaining ions start to re-thermalize to a lower mean velocity. The time constant for this process depends on the Coulomb coupling strength and can

take up to a few seconds. The velocity distribution for the colder and fewer ions is shown on the bottom right of the figure. Concluding, evaporative cooling is best suited for precision experiments on highly abundant species since achievable temperatures are extremely low. For measurements on scarce elements, or elements with low production rates, evaporative cooling is inappropriate due to its immense particle loss.

1.2.3 Collisional cooling

Collisional (or *buffer-gas*) cooling is based on the thermalization of a confined particle species via collisions with a species that has a lower temperature (the coolant). The latter absorbs and dissipates translational energy from the confined species, which enables its trapping in a conservative force field (e.g., an electromagnetic potential). Collisional cooling does not directly depend on the energy level structure or particular charge states of the particles. Instead, it relies on elastic scattering and is applicable to the majority of atoms and molecules. The technique is therefore of similar generality as evaporative cooling [dDF$^+$99]. The lower temperature limit of the species-to-be-cooled after thermalization obviously depends on the initial temperature of the coolant, so the vapor pressure of coolant candidates has to be considered (e.g., at $\approx 1\,\mathrm{K}$, only He has a non-negligible vapor pressure). Depending on the density of the buffer gas, cooling times are typically in the order of 1-100 ms. Negative effects of ion-ion or ion-neutral collisions involve charge exchange or chemical reactions that may lead to the loss of the ion. In certain applications, collisions may also perturb energy levels, but in most cases the advantages outweigh the disadvantages, including the application in Paul traps. For confined ions, the trapping parameters should not be affected by the momentum transfer between the collision partners, i.e., the ions must not leave their stable trapping trajectories. Thus, the mass of the buffer gas particles should be small compared to the trapped ion. Collisions causing small momentum transfers can be modeled as a viscous damping force acting on the ions (for a brief mathematical formulation for viscous damping in Paul traps, see Sec. 1.3.4). Major and Dehmelt proposed buffer-gas cooling for Paul traps and treated collision effects on the secular and micromotion in 1968 [MD68]. Since then, much progress has been achieved (e.g., [BZHS86, VAVB83, LBM92, MTMS93]) and nowadays, the technique is widely utilized in nuclear physics and spectroscopy. Standalone neutral buffer-gas cooling can not be performed in Penning traps, as there is no restoring force in the radial direction (unlike in the Paul trap) [IBBW95]. Thus, collisions would drive the ions out of the trap, unless they are combined with a proper RF sideband excitation [SBB$^+$91] (see Sec. 2.3.2 for the application of buffer-gas cooling at the TRIGA-TRAP Penning trap).
In summary, collisional cooling is a very powerful and robust technique for the quick cooling over a long range of particle numbers (from a few to 10^6 particles). Even the cooling of continuous beams is possible in a section where radial confinement of the beam is provided [LBG$^+$09]. As the lower temperature limit is given by the coolant, cooling to the sub-K regime is not possible. The generality of this technique makes

it applicable to a wide spectrum of particle species.

1.2.4 Laser cooling

The idea of laser cooling is the reduction of the particles' motional amplitudes by the force of light. In contrast to other cooling techniques, laser cooling can be applied to neutral particles. Still, laser cooling of charged particles is feasible and utilized in many experiments. Particles are decelerated by the momentum transfer of an incident photon to the particle. In 1917, Einstein showed that the momentum of a photon $\vec{p}_\gamma$ with wavelength λ is proportional to its energy E by

$$\vec{p}_\gamma = \hbar\vec{k} = \frac{E}{c}\vec{e}_k, \tag{1.11}$$

where $\vec{k}$=$2\pi\vec{e}_k/\lambda$ denotes the wave vector and $\hbar$ the reduced Planck constant. The first observation of the recoil momentum of light was observed by Frisch in 1933 [Fri33], but thermal light sources with their broad energy spectrum were not suitable to advance this technique as the efficiency strongly depends on the statistical probability of the interaction of the photon and the desired particle. This can occur through incoherent scattering of the photon via resonant absorption and spontaneous emission (typically atoms and ions), or by the coupling of the light field to induced or permanent dipole moments (typically molecules). In both cases, only photons of a specific wavelength can interact with the particle. No wonder that by the invention of the laser, experiments based on the deflection of matter by light received a tremendous boost in efficiency, and the first success stories were reported in the early 1970s [SWW72, JLPP73, BDSW74]. Laser cooling of free atoms with laser light was first suggested by Hänsch and Schawlow in 1975 [HS75], and of ions bound in electromagnetic traps by Wineland and Dehmelt [WD75]. The first experimental realization took place about three years later, by Neuhauser *et al.* with trapped Ba ions [NHTD78] and by Wineland *et al.* with trapped Mg ions [WDW78]. The first deceleration of a thermal ion beam was realized by Phillips and Metcalf [PM82]. From there on, laser cooling spread to various fields of physics. Apart from enabling high-precision spectroscopy [WIVDJ83] and fundamental quantum optics experiments [SNBT86], it paved the way to modern fields of physics like quantum state engineering [CPBZ96], entanglement [SKK$^+$00] or quantum information processing [Mon02, NC10]. The significance of laser cooling manifested in the Physics Nobel Prize in 1997, which was awarded to Steven Chu, Claude Cohen-Tannoudji, and William D. Phillips *for (the) development of methods to cool and trap atoms with laser light* [CCTP97]. Thorough reviews summing up the history and required theoretical descriptions for laser cooling can be found in, e.g., [Ste86], [WIBH87], or [EMSKB03].

The cooling of particles with laser light is based on the fact that the spatial direction of a photon released by spontaneous emission in an excited atom or ion is uniformly distributed over the total solid angle, while the direction of the absorbed photon can be controlled. The absorption and emission processes are illustrated in

Fig. 1.7. When the incident photon with energy $h\nu_L$ is resonantly absorbed by the

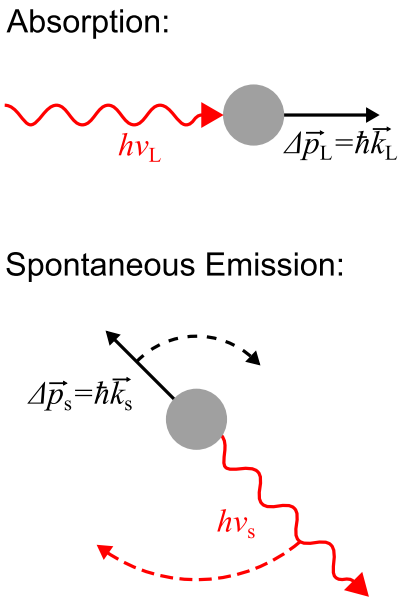

Figure 1.7: Momentum transfer from an incident photon to an atom. $\vec{k}_L$ denotes the wave vector of the incident photon, and $\vec{k}_s$ is the wave vector of the photon created by spontaneous emission. The direction of the spontaneous emission's photon is uniformly distributed over the solid angle.

atom, the momentum change of the atom is, according to Eq. (1.11), $\Delta\vec{p}_L = \hbar\vec{k}_L$. After the absorption process, the atom is in an excited state for a time defined by its life time τ. The atom is then de-excited by spontaneous emission of a photon of energy

$$h\nu_s = \frac{hc}{\lambda_s}, \tag{1.12}$$

with $\lambda_s=2\pi/|\vec{k}_s|$ being its wavelength. The energy exactly matches the level difference of the atomic transition and is not necessarily equal to the energy of the absorbed photon $h\nu_L$ created by the laser. However, to avoid optical pumping into long-living atomic states, cooling transitions are typically selected such that de-excitation leads back to the ground state (*closed transitions*), which means that λ_s and λ_L are similar except for small detunings. The momentum change due to the emitted photon is then $\Delta\vec{p}_s=\hbar\vec{k}_s$. After n absorption and emission processes, the total momentum transferred is [Ste86]

$$\Delta\vec{p}_{\text{total}} = \sum_n \hbar\vec{k}_L + \underbrace{\sum_n \hbar\vec{k}_s}_{\to 0 \text{ for } n\to\infty} . \tag{1.13}$$

The second term vanishes for large numbers of interaction processes due to the uniform distribution of the emitted photon's direction. This results in a net force in

the direction of $\vec{k}_\mathrm{L}$ on the particle of

$$\vec{F} = \frac{\mathrm{d}\vec{p}_\mathrm{total}}{\mathrm{d}t} = n\hbar\vec{k}_\mathrm{L}\frac{\rho_0}{\tau}, \tag{1.14}$$

where $0 \leq \rho_0 \leq 1$ represents the population of the ground state. The effectiveness of the process is strongly dependent on the life time τ of the excited state. If the life time is long compared to the number of incident photons per time unit (i.e., the laser intensity I), the excited state reaches saturation and no more absorption takes place. The probability of the absorption is maximal for zero detuning

$$\delta = \omega_\mathrm{L} - \omega_\mathrm{s}. \tag{1.15}$$

However, high laser intensities near resonance also make induced emission more likely, which cancels the momentum transfer from the absorption. Taking into account saturation and detuning, the force can be written as [MS79]

$$\vec{F} = \hbar\vec{k}_\mathrm{L}\frac{\Gamma}{2} \cdot \frac{I/I_0}{1 + I/I_0 + (2\delta/\Gamma)^2}, \tag{1.16}$$

where Γ denotes the natural line width of the transition and I_0 the saturation intensity. The laser frequency and intensity are therefore critical parameters that have to be matched to the experimental requirements.

For the cooling of an atomic ensemble in place, two counter-propagating lasers can be irradiated into the ensemble in the dimension that has to be cooled. The temperature of the atomic ensemble corresponds to a Gaussian velocity distribution of the atoms. Thus, the ensemble's resonance line width is Doppler-broadened. If the two counter-propagating lasers are slightly red-shifted (see Fig. 1.8), only the high velocity classes of atoms that are moving toward the laser (i.e., away from the ensemble's center) are in resonance and get cooled. This concept is known as

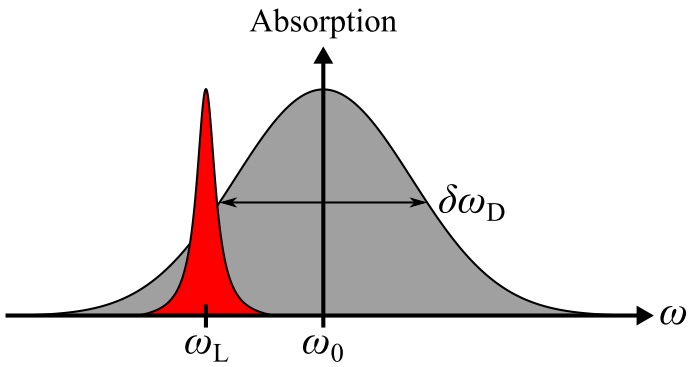

Figure 1.8: Doppler-broadened profile of an atomic ensemble. A red-shifted narrowband incident laser only addresses counter-propagating velocity classes. The Doppler width depends on the temperature of the ensemble $\delta\omega_\mathrm{D} = (\omega_0/c)\sqrt{8k_\mathrm{B}T\ln 2/m}$.

"optical molasses", as the laser fields can be described by a frictional force term in the particle's equations of motion. Very low temperatures can be achieved, and atoms were trapped in a 3D volume, using two counter-propagating red-shifted laser beams in each dimension and a magnetic field, forming a so-called Magneto-Optical Trap (MOT) [RPC+87, DMA+95]. When laser cooling is accomplished by driving a single photon transition, the minimum temperature that can be achieved is given by the Doppler-limit [Dem96]:

$$T_{\mathrm{D}} = \frac{\hbar\Gamma}{2k_{\mathrm{B}}}. \tag{1.17}$$

Therefore, laser cooling is a very powerful technique not only for neutral but also charged particles as temperatures can be decreased to sub-mK scales. However, each atom or ion requires a specific wavelength, if a suitable transition is available at all. This enormously raises the effort for experiments designed for different particle species.

1.3 Radio-Frequency Quadrupoles

1.3.1 The principle of linear Paul traps

The need to trap charged particles with lowest possible kinetic energies requires an electromagnetic field configuration that has its potential minimum (or maximum, depending on the sign of the charge of the particle) in vacuum. One way to achieve this is the superposition of a static electric quadrupole field with a magnetic field (see Sec. 2.3.1). Another possibility is to use an oscillating electric quadrupole field in a suitable electrode geometry. Wolfgang Paul built and named such a device *"quadrupole mass spectrometer"* in 1953 [PS53]. *For the development of the ion trap technique*, he received the Nobel Prize in Physics in 1989, together with Hans Georg Dehmelt and Norman Foster Ramsey [RDP89].

The *linear* Paul trap, or quadrupole ion guide, uses a slightly different design based on the same principle. It consists of four parallel, hyperbolically shaped rods, as it is shown in Fig. 1.9. This geometry allows the confinement of charged particles in the two radial dimensions x and y. The electric potential for the quadrupole field has quadratic dependence on the position coordinates:

$$\Phi(x, y) = \Phi_0 \frac{(x^2 - y^2)}{2r_0^2}, \tag{1.18}$$

with the potential Φ_0 applied to the rods and the minimum distance from the trap center to the rods r_0. The electrical forces on particles with charge e in x- and

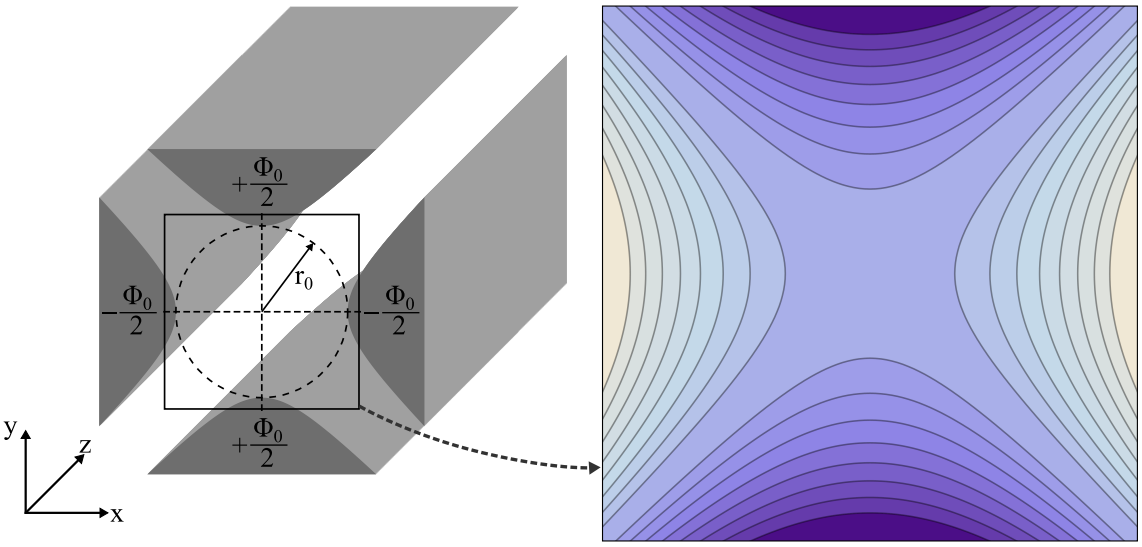

Figure 1.9: Left: configuration of a quadrupole ion guide with hyperbolical electrodes. Right: corresponding equipotential lines.

y-direction

$$F_x = -e\nabla_x\Phi(x,y) = -e\Phi_0\frac{x}{r_0^2}, \tag{1.19}$$

$$F_y = -e\nabla_y\Phi(x,y) = e\Phi_0\frac{y}{r_0^2} \tag{1.20}$$

have opposite sign and depend linearly on the particle's displacement from the center of the quadrupole. The potential creating the quadrupole field is a superposition of a DC and an AC potential

$$\Phi_0 = U + V_{\mathrm{RF}} \cdot \cos(\omega_{\mathrm{RF}} t), \tag{1.21}$$

where U is the amplitude of the DC potential and V_{RF} the amplitude of the AC potential oscillating with frequency ω_{RF}. Each rod is 180° out of phase with its neighboring rods. This results in a net force towards the trap center for a charged particle, which can be visualized by regarding the effect of one full cycle of the oscillating electric field on the particle. Consider a particle in the x-plane at the position x_1 away from the trap center, which is being attracted by the electrode for half a cycle with the force $F_x(x_1)$, causing it to move towards the electrode by the length ϵ. During the next half of the cycle, it will be repelled by the electrode and pushed towards the trap center with the (stronger) force $F_x(x_1+\epsilon) > F_x(x_1)$. This will slowly drive the particle towards the trap center over the course of many cycles. The analytical approach assumes hyperbolically shaped electrodes, but according to a semi-analytical calculation by Lee-Whiting and Yamazaki [LWY71], the quadrupole symmetry of the equipotential lines can be realized to a good approximation also with circular arcs if

$$\frac{R}{r_0} = 1.14511, \tag{1.22}$$

with R being the radius of the rods. While circular rods therefore retain the field geometry, their manufacturing is quite simple, making them the most popular choice for quadrupole ion guides.

1.3.2 Equations of motion for charged particles

The equation of motion for a particle with mass m and charge e inside an electric field in vacuum derives from equating Newton's second law with the Lorentz force:

$$m\ddot{x} = eE_{\mathrm{x}}, \tag{1.23}$$

$$m\ddot{y} = eE_{\mathrm{y}}. \tag{1.24}$$

For the quadrupole field of Eq. (1.18) and the potential defined in Eq. (1.21), the equations of motion become

$$\ddot{x} + \frac{e}{mr_0^2}(U + V_{\mathrm{RF}} \cdot \cos(\omega_{\mathrm{RF}} t))x = 0, \tag{1.25}$$

$$\ddot{y} - \frac{e}{mr_0^2}(U + V_{\mathrm{RF}} \cdot \cos(\omega_{\mathrm{RF}} t))y = 0. \tag{1.26}$$

The introduction of two dimensionless parameters

$$a = \frac{2eU}{\frac{1}{2}mr_0^2\omega_{\mathrm{RF}}^2},\ q = \frac{eV_{\mathrm{RF}}}{\frac{1}{2}mr_0^2\omega_{\mathrm{RF}}^2} \tag{1.27}$$

and the substitution of time $\tau{=}\frac{1}{2}\omega_{\mathrm{RF}}t$ simplify the equations of motion to

$$\frac{d^2x}{d\tau^2} + (a + 2q \cdot \cos 2\tau)x = 0, \tag{1.28}$$

$$\frac{d^2y}{d\tau^2} - (a + 2q \cdot \cos 2\tau)y = 0. \tag{1.29}$$

These are the Mathieu equations [McL47] in their canonical form. The Mathieu equation is a linear ordinary differential equation of second order, its properties are well-established [AS64].

1.3.3 Radial confinement and stability diagram

The solutions to the Mathieu equations can be divided into groups of stable and unstable solutions, referring to the evolution of the particle's motion in the radial plane. If the motional amplitude of the particle is limited to and does not exceed r_0 for all times t, the solution is called stable. For radial confinement inside the linear Paul trap, this criterion has to be fulfilled for both the x- and y-plane. The regions of stability can be plotted in dependence of a and q yielding the so-called stability diagram, which is shown in Fig. 1.10. It can be seen in the left plot that the region with x- and y-stability is limited to very small parts of the individual regions of x- or y-stability. The right side of Fig. 1.10 shows that the linear Paul trap can be used as a mass filter for $a{\neq}0$. On a constant a/q-line, particles with specific values of m that are located inside the region of stable solutions (m_1, m_2) will be confined in the trap. Particles with unsuitable mass and therefore unstable solutions (m_3) will not be trapped and consequently get lost after some time. For illustration, the time evolution of the motional amplitudes of a charged particle is simulated in Fig. 1.11 for exemplary values of a and q, resulting in stable (top) or unstable (bottom) solutions. The plots on the left display particle trajectories in quadrupole ion guides, where $a{=}0$, thus $U{=}0$ (so-called *RF-only* mode). In that case, the Paul trap is insensitive to differences in the particle mass (still, the motion is stable only for $q{\leq}0.908$). The right side shows the trajectories for $a{\neq}0$, when the Paul trap is employed as a mass filter. For stable trapping conditions, the total motion is a superposition of oscillations with frequency [Kim97, MD68]

$$\omega_n = \left(n + \frac{\beta}{2}\right)\omega_{\mathrm{RF}}, \text{with } n \in \mathbb{N}, \tag{1.30}$$

where $\beta{=}\beta(a,q)$ defines the border between stable and unstable regions of the stability diagram (for $0{\leq}\beta{\leq}1$, the motion is stable) [Car72]. For low values of β ($q{\leq}0.5$), higher orders of ω_n ($n{\geq}2$) can be neglected and the total motion can be described

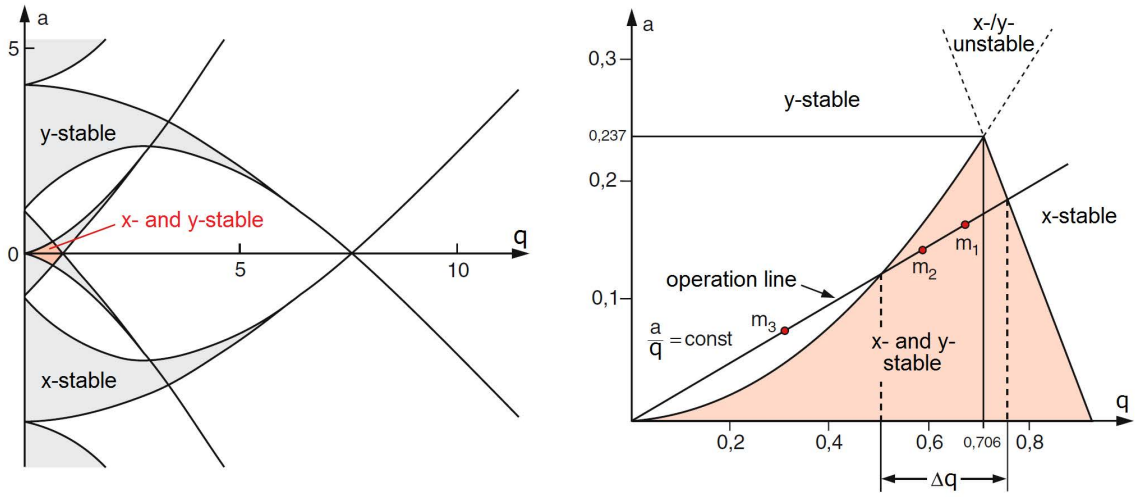

Figure 1.10: Left: regions of stability in x and y, plotted in the a-q diagram, taken from [Dem96]. Right: magnified view on the $q \leq 1$ region. On the operation line, the linear Paul trap can be used as a mass filter by tuning its overlap with the stability region via the a/q-ratio.

as a composition of two distinct motions (with frequencies $\omega_{n=0}$ and $\omega_{n=1}$). The high-frequency motion

$$\omega_1 = \left(1 + \frac{\beta}{2}\right) \omega_{\mathrm{RF}} \tag{1.31}$$

is called the micromotion and is caused by the high-frequency field oscillations generated by the AC voltage V_{RF}. The amplitude of this motion has a linear dependence on the particle's extent from the trap center. The low-frequency motion, *secular motion*, or *macromotion*, is the 0^{th}-order component of Eq. (1.30). Its amplitude represents the distance of the particle to the trap center, averaged over one AC cycle. For small q, it is large in relation to the amplitude of the micromotion. A smart approach is to understand the macromotion as a harmonic oscillation in a pseudo-potential well, which was proposed by Dehmelt [Deh67] and worked out by Dawson *et al.* [Daw76]. According to their work, the effective pseudo potential in the x- and y-plane can be written as

$$D(r) = \frac{qV_{\mathrm{RF}}}{4r_0^2} r^2, \tag{1.32}$$

with $r = \sqrt{x^2 + y^2}$. A charged particle then oscillates in the pseudo-potential well with its macromotion frequency

$$\omega_0 = \frac{\beta}{2}\omega_{\mathrm{RF}} \simeq \frac{q\omega_{\mathrm{RF}}}{2\sqrt{2}} \tag{1.33}$$

while moving along the z-axis through the structure. For $q > 0.4$, the amplitude of the micromotion is not anymore small compared to the macromotion's amplitude,

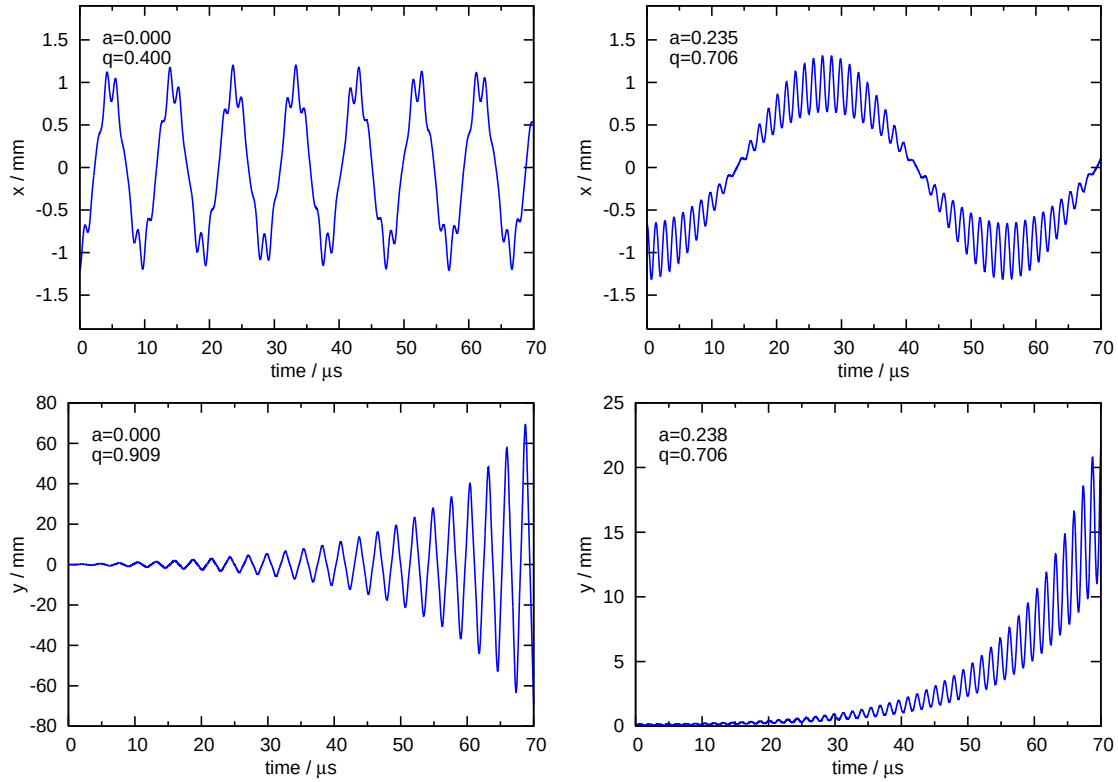

Figure 1.11: Simulation of charged-particle trajectories inside an electric quadrupole field in vacuum. The figures have the same starting conditions, particles enter the field at (x,y)=$(-1\,\mathrm{mm},0\,\mathrm{mm})$. Top: stable solutions of the Mathieu equation lead to limited motional amplitudes, enabling trapping. Bottom: outside the stability region, the particles' amplitude quickly exceeds the spatial boundaries of the trap electrodes. Note the changes in the ordinate axis.

thereby adding terms of higher order to Eq. (1.30). Hence, the pseudo-potential approximation is no longer applicable.

1.3.4 Collisional cooling in linear Paul traps

The application of a cooling method to the Paul trap makes it an even more powerful device for ion beam manipulation. Among the cooling techniques described in Sec. 1.2, collisional cooling is by far the most suitable and easiest one when dealing with tens of thousands of particles at the same time. Therefore, a buffer gas medium is introduced into the linear Paul trap, which will cause the trapped particles to interact with the buffer gas atoms. Essentially, an energy transfer between the two collision partners through elastic scattering occurs. This energy transfer between a charged particle of mass m and a neutral particle of mass m_r was investigated by

Major and Dehmelt [MD68]. Regarding the effect on the kinetic energy of the ion, they distinguished between three different cases. For $m \ll m_\mathrm{r}$, they showed that the elastic scattering of the ions on the much heavier neutrals resulted in a gain of kinetic energy, due to their highly energetic micromotion. If $m = m_\mathrm{r}$, there is a zero net increase of the ion's energy when averaged over one macrooscillation. For the case of $m \gg m_\mathrm{r}$, collisions will result in a viscous drag, decreasing the kinetic energy of the ion exponentially. Hence, it is advisable to select the atomic species of the buffer gas sufficiently light in relation to the trapped ion species to avoid large disruptions of the ion trajectory after a collision. Therefore, a high buffer-gas purity is also advisable, as contaminant atoms or molecules have typically larger masses. In principle, the ion's kinetic energy could be decreased to the point where it is in thermal equilibrium with the surrounding buffer gas (for room-temperature buffer gas, this would be $E_\mathrm{therm}{\approx}25\,\mathrm{meV}$).
In a simple approach, the cooling process can be modeled as a viscous damping force of the buffer gas acting on the trapped ion. This approach, however, does not cover all mechanisms and effects that may occur, like particle-particle interactions, particle loss, or RF heating, which can be studied in a microscopic treatment. Both kinds of calculations have been performed and compared in literature, e.g., by Lunney *et al.* [LM99] or Schwarz [Sch98]. To describe the cooling of heavy ions in a much lighter buffer gas, the viscous-damping approach delivers sufficiently accurate results [HDK$^+$01]. An average viscous damping force can be written as

$$\vec{F} = -Km\vec{v}, \tag{1.34}$$

where m denotes the mass of the ion and $\vec{v}$ its velocity vector. The dimensionless damping coefficient K includes the temperature T and the pressure p of the buffer gas, normalized to standard values T_N and p_N), and the reduced ion mobility K_0 (with dimension $\mathrm{m^2/Vs}$):

$$K = K_0 \frac{T}{T_\mathrm{N}} \frac{p_\mathrm{N}}{p}. \tag{1.35}$$

If the linear Paul trap is used as a quadrupole ion guide (without mass selectivity), then a=0 and Eq. (1.25) simplifies a bit. By adding the viscous damping force, the equation of motion becomes

$$\ddot{x} = \frac{e}{m}\left(-\frac{V_\mathrm{RF}\cdot\cos(\omega_\mathrm{RF}t)}{r_0^2}x - \frac{\dot{x}}{K} + \frac{v_\mathrm{therm}}{K_\mathrm{therm}}\cos(\omega_0 t)\right). \tag{1.36}$$

The last term includes the velocity v_therm of the ion at the environmental temperature (e.g., 293 K), with K_therm representing the corresponding mobility. Equation (1.36) implies that the cooling of the particle is faster for higher pressures. However, experimental constraints can restrict the maximum buffer gas pressure, which will be discussed in Sec. 3.3. A simulation of the damped ion trajectory with a=0 and q=0.5 is shown in Fig. 1.12. As time elapses, the amplitude of the ion's macromotion decreases significantly until the thermal velocity v_therm is reached. The amplitude of

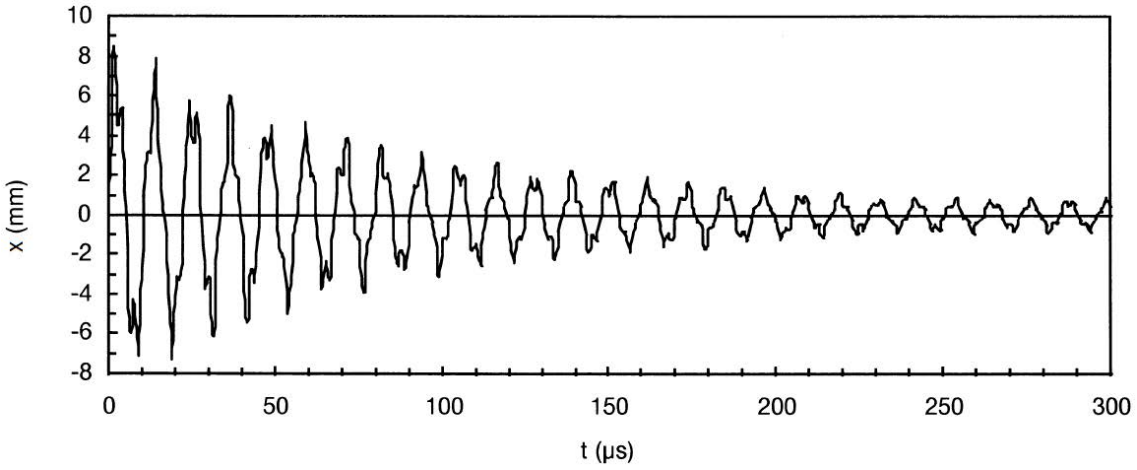

Figure 1.12: Simulation of a $^{133}Cs^{+}$ trajectory through a linear Paul trap with viscous damping inside a $4.4{\cdot}10^{-2}$ mbar He buffer gas atmosphere, from [LM99]. The initial axial and transverse energy are 130 eV and 8.5 eV, respectively. The transversal motional amplitude is cooled to a large extent after about 100 µs.

the micromotion cannot be cooled since it is constantly driven by the high-frequency oscillation V_{RF}; however, due to the reduced spatial distribution of the ions around the trap center, the radius-dependent micromotion is also reduced [IBBW95]. The viscous-damping approach is only valid if the influence of collisions with the buffer-gas atoms on the ion trajectory is negligible. This is only true if the mass of the ions is large compared to the mass of the buffer-gas atoms. The microscopic model does not have this restriction and is discussed in, e.g., [Sch98].

1.3.5 Creation of ion bunches

When using the linear Paul trap as a quadrupole ion guide with collisional cooling, it can reduce the emittance of continuous ion beams of several nanoamperes. For example, the former MISTRAL quadrupole ion guide named COLETTE (cooler for emittance elimination) was able to reduce the transverse emittance of a 20 keV $^{14}N^{+}$ beam by a factor of $\sim$8 [LBG^{+}09]. Its rods were 15-fold segmented to provide a DC potential gradient with negative slope along the symmetry axis that guided the ions toward the exit. COLETTE was later transferred to TRIGA-SPEC [KKB^{+}08, BBB^{+}14] with a focus on bunching cooled ions.

To realize the creation of bunches, a temporary trapping in all three dimensions has to be implemented to accumulate ions for the desired time period. As the quadrupole ion guide provides the confinement of ions in the (radial) x and y plane, confinement in the (axial) z-plane has to be added, which can be provided by a DC potential well along the z-axis. On each rod segment, a specific DC potential $U(z)$ is applied while still maintaining the same AC potential along the rod needed for

radial confinement. The axial DC potential well is ideally positioned close to the exit. As an example, the potential shape for the TRIGA-SPEC RFQ is shown in Fig. 1.13. Ions enter the structure from the left, their kinetic energy being slightly

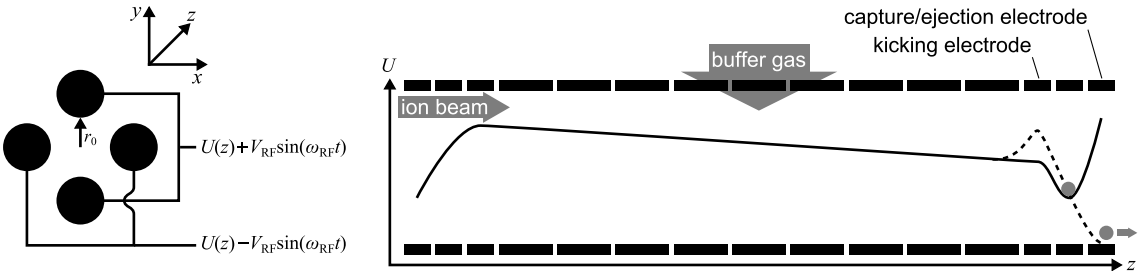

Figure 1.13: Left: Sketch of the rods and their supply voltages along the symmetry axis. Right: schematic cross section of the 15-fold segmented rods of COLETTE. The DC potential along the z-axis is drawn in between the rods: The solid line represents the potential during ion accumulation, while the dashed line represents the ejection potential. From [BBB+14].

above the applied DC potential (solid line) on the left RFQ segments. They are repelled by the higher potential on the last ("capture/ejection") electrode and reflected back to the RFQ entrance. However, the buffer-gas cooling reduced their kinetic energy already to a point where they are not able to pass the entrance potential again. The ions are therefore axially trapped and get accumulated in the potential minimum ("bunched"), which is in the case of Fig. 1.13 positioned at the second-to-last electrode. The process is finished once the ions are in thermal equilibrium and further cooling does not affect their kinetic energy anymore. The required time for this process is called the *cooling time*, which depends on several parameters such as buffer-gas pressure and species, ion species, initial kinetic energy, and DC potential shape. Typical cooling times are in the order of a few milliseconds and gas pressures are in the range of 10^{-5} to 10^{-2} mbar. During the cooling time, the injection of additional ions into the quadrupole structure is preferably interrupted, as lately injected ions would not be cooled to full extent. When the cooling time has passed, the ion's emittance and averaged spatial position stay constant. Then, the two electrodes adjacent to the potential minimum are switched simultaneously: the kicking electrode to a higher potential and the capture/ejection electrode to a lower one. This changes the potential well minimum to a negative slope at the position of the accumulated ions (i.e., *ion bunch*), resulting in an electrostatic ejection of the ion bunch. The time of the switching process should be fast in relation to the ion's axial frequency to avoid a longitudinal broadening of the emitted ion bunch. Devices capable of accumulating and bunching ions are called *radio-frequency quadrupole (RFQ) bunchers*, as the typical operation frequency is in the RF regime.

1.3.6 Space-charge limitations and RF heating

Following [MD68] (and discussed in Sec. 1.3.4), ions in a quadrupole ion guide are cooled to the temperature of the surrounding gas through collisional cooling. This was stated for quadrupole ion guides but in the same way holds for RFQ bunchers. Strictly speaking, this approach is only correct if ion-ion interactions are neglected. When there are two or more ions with the same sign of charge in an ensemble, a repulsive Coulomb force will tear them apart and counteract the attractive force created by the pseudo-potential. Therefore, the ion ensemble occupies a certain physical volume around the trap center. Individual ions having the highest average distance from the trap center will have an increased micromotion amplitude, which leads to an increase of their kinetic energy. The additional kinetic energy is then dissipated in the ensemble, heating it up as a whole. This effect is called RF heating and results in an ion ensemble always having a higher temperature than the surrounding buffer gas. The effect of space charge has been investigated by Todd *et al.* [TWM80], but the predicted densities for cooled macromotions have not been reached, presumably due to RF heating [WIVDJ83]. The RF heating mechanism was described in [CD69] and computer-simulated for a system of many interacting ions in [BKQW89]. If the ion density becomes low enough and their motions independent from each other, the RF heating vanishes. For higher densities, the collisional cooling will compensate for the RF heating in the equilibrium state, as it is depicted in Fig. 1.14. The RF heating gets stronger for higher ion numbers N

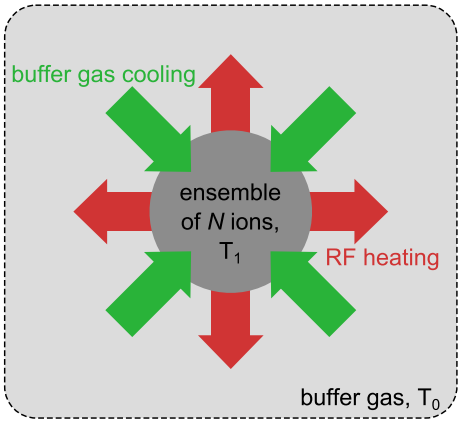

Figure 1.14: Physical volume occupied by the ion ensemble inside an RFQ buncher. The volume is initially defined by the equilibrium of the counteracting forces of space-charge and pseudo potential, but buffer gas cooling will decrease the ion's temperature (and thus the volume), while RF heating has the opposite effect.

in the trap, because the ions will initially occupy a larger physical volume in the trap. It was shown by Lunney *et al.* [LBM92] that the ion ensemble's temperature above the buffer-gas temperature is proportional to $N^{\frac{2}{3}}$. In the case of increasing numbers of accumulated ions, the kinetic energy of the ensemble will increase to a

point where its spatial extent reaches the physical limits of the trap. The ions with the highest kinetic energy inside the ensemble will then hit the electrodes and get lost. Thus, no further ions can be stored as their addition to the ensemble would immediately result in ion loss. This can be regarded as a hard limit of the number of ions stored inside an RFQ buncher. However, the phase space volume and shape of this ion ensemble will be unacceptably large in most practical cases so that much lower ion numbers with essentially smaller phase space volume are desired instead.

2 Experimental Setup

2.1 The TRIGA-SPEC experiment

The TRIGA-SPEC experiment aims to provide model-independent nuclear ground-state data of neutron-rich radioactive nuclides obtained via mass spectrometry and laser spectroscopy [KKB+08, BBB+14]. TRIGA-SPEC is installed at the research reactor TRIGA Mainz at the Institute for Nuclear Chemistry of the Johannes Gutenberg-University of Mainz. TRIGA-SPEC consists of two experimental branches, namely TRIGA-TRAP and TRIGA-LASER, as shown in Fig. 2.1. The Penning-trap mass spectrometer TRIGA-TRAP is used routinely to determine masses and mass differences, i.e., Q-values, of various nuclides with a relative precision of about 10^{-8} [KAB+11, SBB+12], using the well-established time-of-flight ion-cyclotron-resonance technique (TOF-ICR) [KBK+95]. TRIGA-TRAP is presented in Sec. 2.3. At the collinear laser spectroscopy beam line TRIGA-LASER, nuclear spins, moments, and charge radii of stable and short-lived nuclei will be determined [KKB+08]. The technique is based on the collinear superposition of a narrow bandwidth laser beam with an atom (or in some cases an ion) beam. Fluorescence spectra are obtained by applying a post-acceleration voltage to the optical detection unit (ODU) to tune the Doppler-shifted laser frequency into resonance with the moving atoms [Kau76]. TRIGA-LASER is presented in Sec. 2.4. The two branches share the experimental section for ion beam production and preparation, the so-called ion beam preparation transfer line. Here, a 30-keV ion beam provided by the on-line ion source is accumulated, cooled, and bunched prior to the delivery to the experimental branches. A photograph of the experimental site inside the reactor hall is shown in Fig. 2.2.

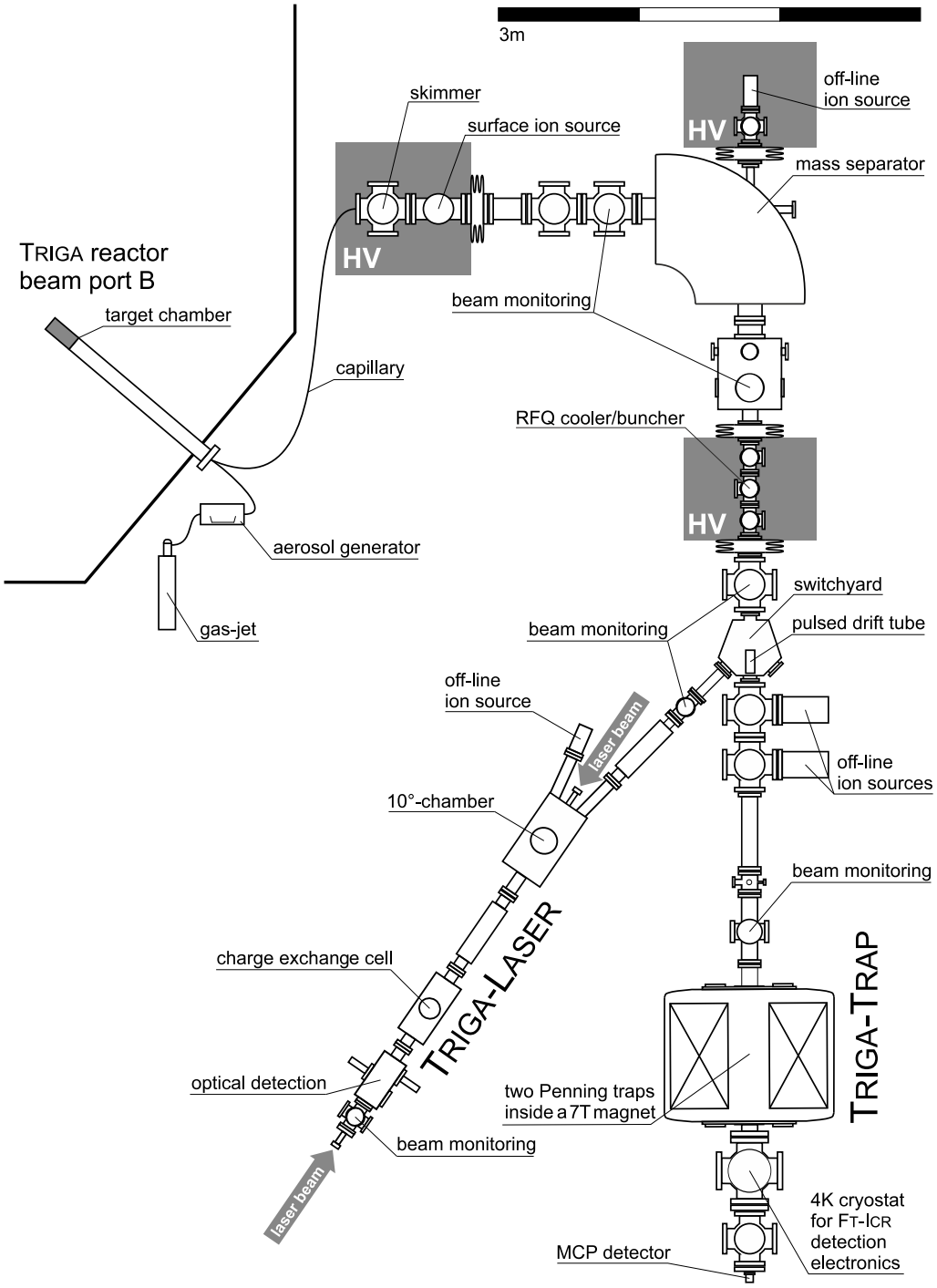

Figure 2.1: Sketch of the TRIGA-SPEC experiment. The two branches TRIGA-TRAP and TRIGA-LASER share the section for ion beam production and preparation.

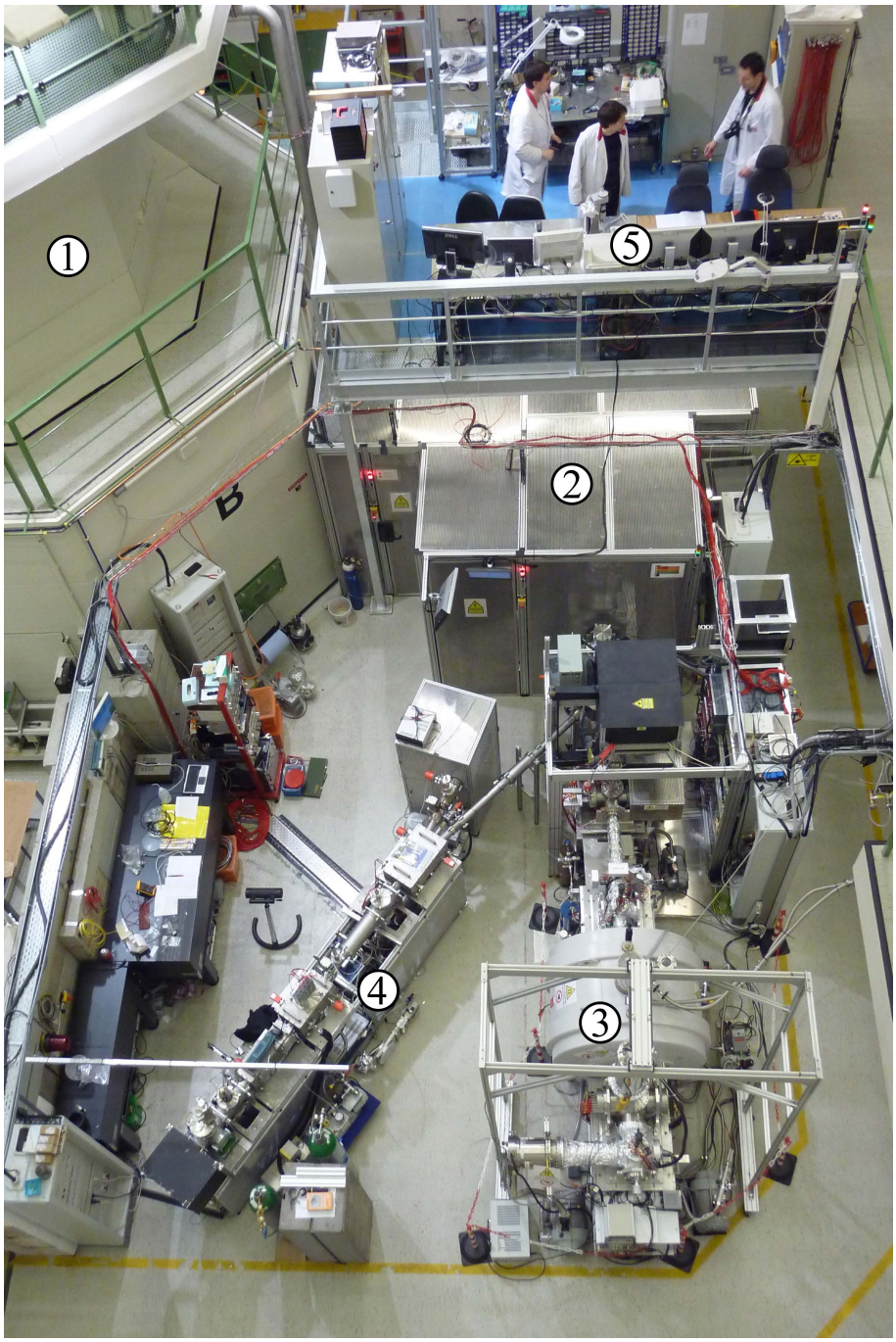

Figure 2.2: Photograph of the TRIGA-SPEC experiment at the location of the TRIGA Mainz reactor (1). The ion beam preparation transfer line (2) is enclosed by a high-voltage safety cage. TRIGA-TRAP (3) and TRIGA-LASER (4) follow subsequently. The setup can be controlled from the platform (5).

2.2 The ion beam preparation transfer line

2.2.1 Production of radioactive nuclides in the TRIGA Mainz research reactor

The radioactive nuclides that are under investigation by the TRIGA-SPEC experimental branches are produced by neutron-induced fission of an actinide target inside a TRIGA (**T**raining, **R**esearch, **I**sotopes, **G**eneral **A**tomic) reactor. This reactor type is the most widely used type of research reactor in the world, with steady-state power levels ranging from $20\,\mathrm{kW_{therm}}$ to $20\,\mathrm{MW_{therm}}$ [EK00, HET06]. TRIGA research reactors are light-water reactors, and the fuel elements consist of an uranium-zirconium-hydride (UZrH) alloy, containing $8\,\mathrm{wt\,\%}$ uranium enriched to 20% in ^{235}U [KTM$^+$58]. The ZrH acts as the main moderator. It has the special property of a less efficient moderation at higher temperatures [McR58]. Thus, the reactor operation features a negative temperature coefficient of reactivity, making it inherently safe. This enables a pulsed operation of the reactor: the sudden removal of a boron-carbide[1] control rod from the reactor core starts a chain reaction of an increased amount of promptly emitted neutrons, leading to a peak power of the reactor of $250\,\mathrm{MW_{therm}}$. The fuel elements are heated, causing an increase in the neutron temperature due to an increase in the probability that neutrons will gain energy from the excited hydrogen atoms in the ZrH lattice [NMRW58]. The increased fraction of speeded-up neutrons causes an increased thermal neutron leakage from the core and an increase in the relative number of neutrons captured in the water. The temperature coefficient caused by this process is approximately $-2{\cdot}10^5/^\circ\mathrm{C}$ at 20°C and strongly increases with temperature [KTM$^+$58]. Due to the increased water temperature, the chain reaction is stopped within a few milliseconds, and the reactor returns to normal operating levels. The pulse width of the power peak (FWHM) is about 30 ms, and the pulse frequency is limited to about one per 10 min to avoid damage to the fuel rods caused by thermal stress. In the steady-state mode, the reactor provides up to $100\,\mathrm{kW_{therm}}$ power for an almost unlimited time of operation.

Figure 2.3 shows a sketch of the TRIGA reactor. Access to the reactor core is provided by various systems, e.g., a rotary rack with 80 irradiation positions that can be loaded with samples, pneumatic transfer tubes for a quick transfer of samples in and out of the core, or beam tubes in the biological shield of the reactor that reach close to the core. The latter are used for stationary experiments like TRIGA-SPEC, which require a gap-free connection to the core. The measurement candidates are produced by the fission of an actinide target, located close to the reactor core in one of the beam ports. The fission targets typically consist of ^{235}U, ^{239}Pu or ^{249}Cf, electrodeposited on a titanium or aluminum backing [EK00]. Given the thermal neutron flux Φ_n at the position of the target and the fission yields (taken from [ER95, LBN14]), the production rates of the radioactive nuclides $\Gamma(Z, N)$ by

[1] Boron carbide has the ability to absorb neutrons without forming long-lived radionuclides

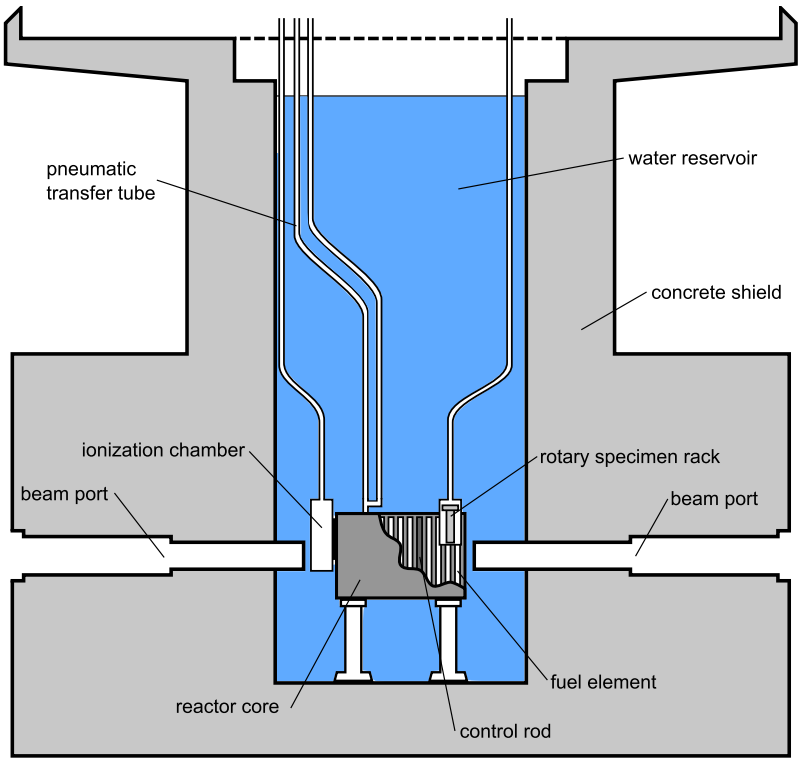

Figure 2.3: Sketch of the TRIGA reactor. TRIGA-SPEC is connected at one of the beam ports.

neutron-induced fission can be calculated according to

$$\Gamma(Z,N) = N_\mathrm{t}\,\sigma_\mathrm{f}\,\Phi_\mathrm{n}\cdot P(Z,N). \tag{2.1}$$

Approximately, $\Phi_\mathrm{n}{=}1.8\cdot10^{11}\,\mathrm{n/(cm^2 s)}$ at $100\,\mathrm{kW_{therm}}$ steady-state mode at beam port B, where TRIGA-SPEC is connected, and Φ_n is a factor of $\approx$2500 higher for a reactor pulse. The production rate of a specific nuclide with (Z,N) depends on the number of fissionable atoms in the target N_t, the fission cross section of the target material σ_f, and Φ_n, multiplied by the individual production probability of the nuclide $P(Z,N)$ [ER95, LBN14]. A graphical representation of the production rates is given in Fig. 2.4.

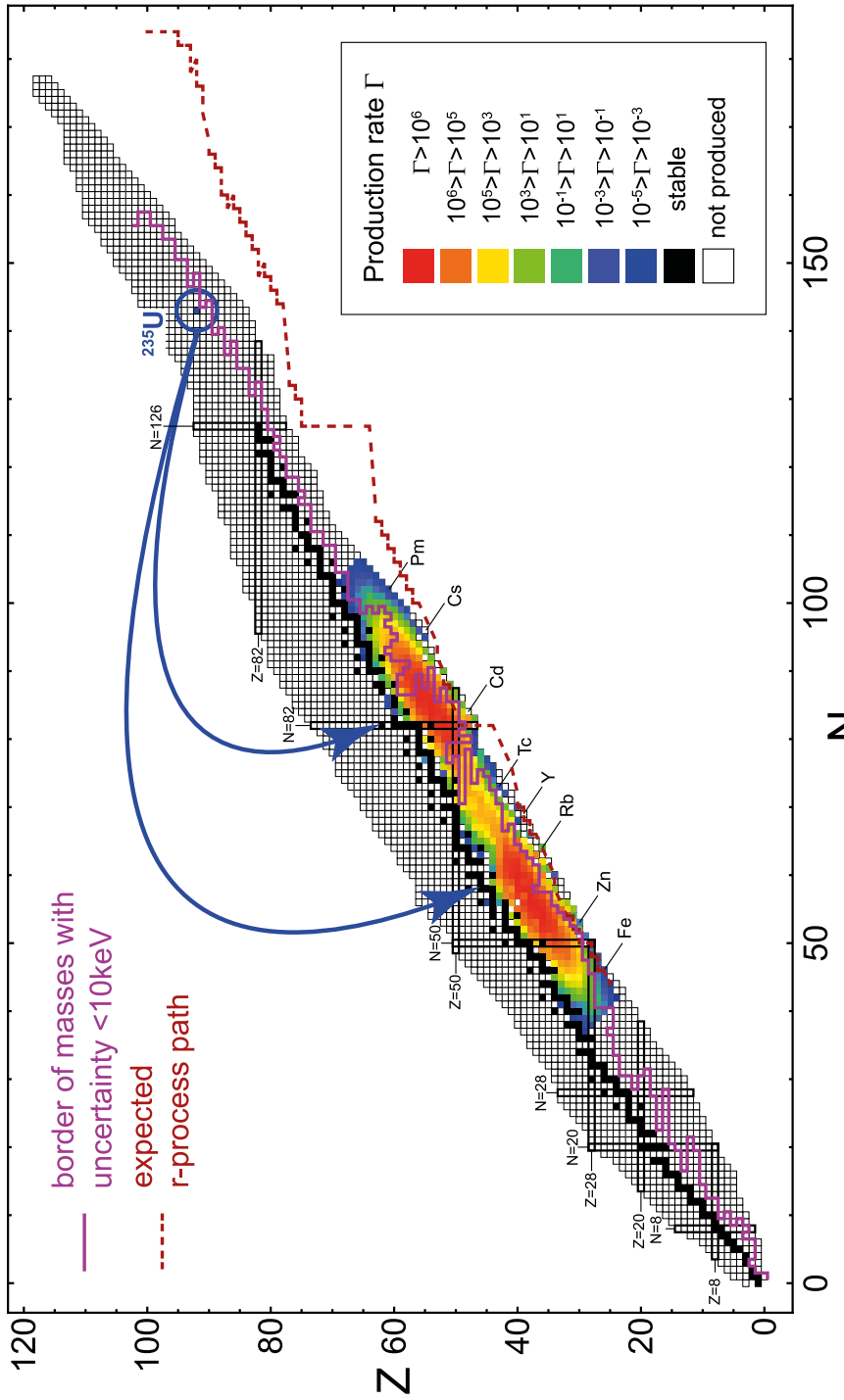

Figure 2.4: Radioactive nuclide production rates for a 310 µg ^{235}U target at beam port B of the TRIGA Mainz reactor. The border of well-known masses and the expected r-process path are included. The graph is taken from [Eib13], the data used to generate the graph are taken from [ER95, LBN14].

The target material fissions into two fragments. The fission fragment's mass distribution is asymmetric: one of the fragments retains a doubly-magic core corresponding to 82 neutrons and 50 protons, making the asymmetric fission energetically favorable [New61]. Thus, for the case of a ^{235}U target, the production yield centers around mass A=138 (*heavy branch*) and A=100 (*light branch*). For heavier target materials, the light branch shifts towards heavier masses, until for ^{258}Fm the fission becomes symmetric [ER95]. By the mass measurement of the fission products, TRIGA-TRAP will further push the border of masses and Q-values that are known with uncertainties lower than 10 keV towards the neutron-rich region. The produced fission products also open the door to a variety of laser-spectroscopic measurements for the TRIGA-LASER experiment, investigating deformation and nuclear structure of these elements.

2.2.2 Extraction of the nuclides with a gas-jet system

The actinide target used for the production of the radioactive nuclides is located inside a pressurized gas chamber, close to the reactor core. The radionuclides are emitted from the target isotropically, with kinetic energies in the order of 100 MeV owing to the energy release during the fission process. Therefore, the fission products have to be decelerated before they are absorbed by geometrical boundaries (i.e., the walls of the target chamber). The chamber is filled with the transport gas, its pressure can be controlled by the incoming gas flow. The stopping power, or energy loss ($-dE/dx$) of a charged particle in a medium can be calculated using the Bethe-Bloch formula [Bet30]. For the design of a target chamber that is able to stop the emitted fission products, the range $R(E)$ as the integral over the reciprocal stopping power has to be calculated

$$R(E) = \int_0^E \left(\frac{-dE'}{dx}\right)^{-1} dE'. \tag{2.2}$$

Ranges and stopping powers for various elements in different media were tabulated by Northcliffe and Schilling [NS70]. The optimum shape for the target chamber was found to be conical [Brü83], the inner volume of the chamber depends on the transport gas (e.g., N_2 has a higher stopping power than He) and its pressure. Additional requirements arise for the practical operation at the research reactor, e.g., the transport medium must not be activated by thermal neutrons[2], and the transport efficiency for carrier molecules has to be as high as possible. Different gas species, their stopping powers and transport efficiencies were studied for isotope separation experiments by Zude [Zud86] at the reactor site. If required, a thin layer of aluminum (typically a few micrometer) can be used to cover the actinide

[2]For example, the noble gas argon can not be used although its relatively high mass would create a high stopping power. ^{42}Ar is produced by neutron capture, which is a β^- emitter with $t_{1/2}$=109 min that has to be collected and disposed of according to nuclear-facility safety protocols.

target, thereby decelerating or suppressing nuclides with corresponding mass numbers A. If the proper thickness of the aluminum layer is chosen, the heavy branch of the fission products around A=130 can be completely blocked, while the light branch suffers from medium losses [Brü83] (see also Sec. 4.3). A schematic view of the installed target chamber is pictured in Fig. 2.5, where also the extraction of the fission products from the chamber to the experimental area by the use of a gas-jet system is illustrated. The limited tube diameter of the reactor's beam ports (ap-

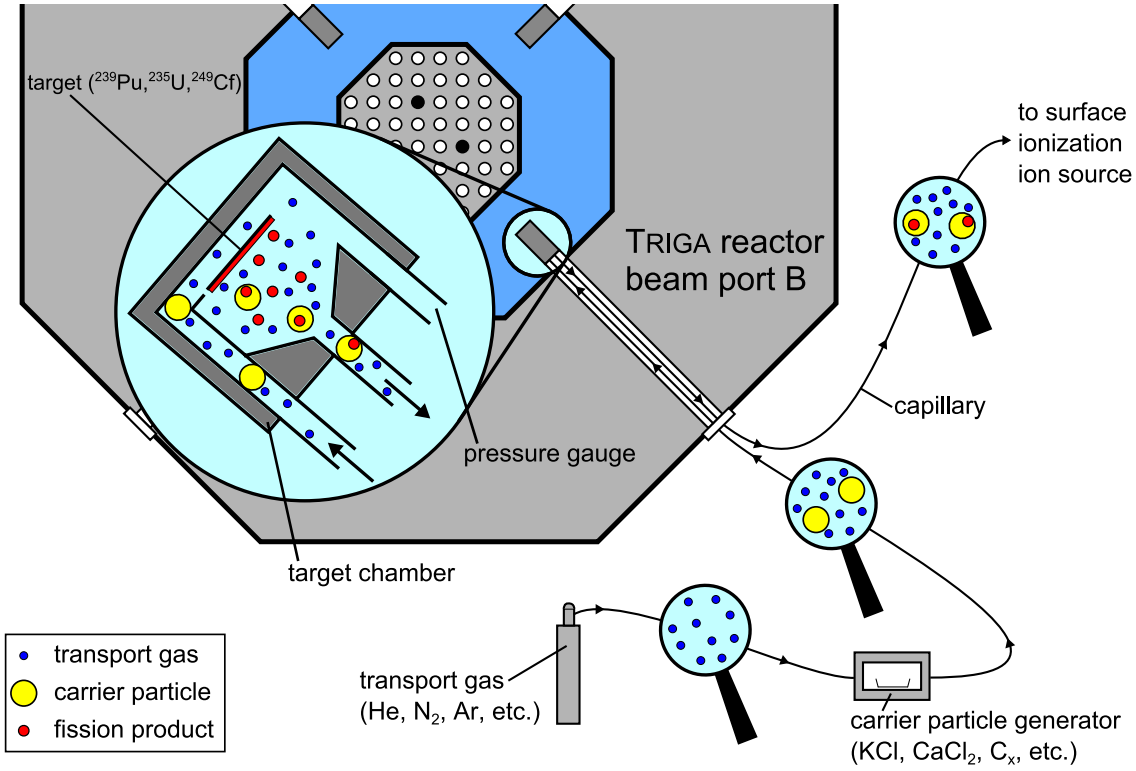

Figure 2.5: Illustration of the gas-jet system at TRIGA-SPEC.

proximately 20 cm) requires a space-saving extraction system. Nevertheless, short transport times and a continuous extraction are mandatory for the operation of TRIGA-SPEC, aiming to measure short-lived nuclides in short measurement cycles. A gas-jet transport system has proven to fulfill the requirements. Its concept was developed already decades ago [MGOT69, GNA$^+$74, Wol76] and it has been utilized at the reactor site for radio-chemical experiments [STH80, MWK$^+$80]. The idea is to move large cluster molecules inside a gas stream through a capillary, thereby passing the target chamber and picking up the fission products. The pick-up takes place after the thermalization of the fission products due to van-der-Waals interaction, Coulomb interaction, or chemisorption [Bau67]. The technique was adapted to TRIGA-SPEC by Eibach *et al.* [EBB$^+$10], initially employing a He transport gas with carbon clusters (C_x) of roughly 90 nm in diameter as carrier particles. Up to now, additional types of transport gases and carrier particles have been investigated.

The most efficient while still practicable combination turned out to be clusters of KCl in an N_2 jet (see Fig. 2.5). The transport gas is supplied by a gas bottle with an attached gas-flow controller. The stream of gas then passes a ceramic bowl that is filled with solid KCl and heated to ∼660°C. Sublimated KCl condensates to clusters and is dragged with the stream of the transport gas. The mixture enters the target chamber through a capillary with a diameter of 4 mm, where the fission products attach to the KCl clusters. The gas jet containing the fission products is guided in a capillary of 1.6 mm inner diameter through the concrete shield of the reactor to the experimental area, where it enters the surface ionization ion source. Regarding the particle transport in a gas jet, three effects impact the transport efficiency: diffusion, sedimentation, and the Bernoulli force. Diffusion is due to inter-particle collisions and depends on the transport-gas density. Sedimentation causes particles to sink in the direction of the gravitational force, depending on the viscosity of the transport gas. Diffusion has a stronger effect on light particles, while sedimentation mainly affects heavy particles [Kul11]. The third effect drives particles back to the capillary center. It is caused by the different velocities of the transport gas inside the capillary

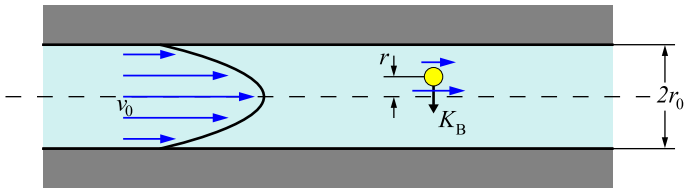

Figure 2.6: Illustration of the velocity distribution across a capillary for a laminar gas flow. Due to the Bernoulli's law, a force K_B is acting on a cluster particle (yellow) as a consequence of the different transport gas velocities on its two sides [Wol76].

as depicted in Fig. 2.6. For a carrier particle of mass m, the gas velocity on the side of the particle towards the capillary center is higher than on the opposing side. Due to Bernoulli's law, a force quadratic in the distance from the capillary center r

$$K_B \propto m^{4/3} v_0^2 r^2 \rho, \tag{2.3}$$

where v_0 denotes the gas velocity on the axis and ρ the density of the transport gas, acts on the particle forcing it back to the center. As the force depends on v_0^2, high transport speeds are favorable if losses become a problem. It was shown for different particle and transport-gas combinations that capillary lengths of several tens of meters are achievable without noticeable particle losses [Wol76]. Moreover, carrier particles tend to exit the capillary very close to the center, which is highly favorable if a skimmer system is added. For KCl clusters as carrier particles and N_2 transport gas, several hundreds of meters traveling distance through a capillary of 2 mm inner diameter were demonstrated [GJB+91].
Absolute yields and transport efficiencies were investigated also at TRIGA-SPEC for different capillary diameters, transport gas flows, carrier particle species and

carrier particle sizes [Ren15, Gru14]. Carrier particles with greater size tend to transport fission products more efficiently, but the transport efficiency normalized to the particle mass falls off after reaching a maximum. The carrier particle mass causes a heavy load on the surface ionizer and is ideally kept low to avoid the choking of the ionizer. The particle size and mass can be controlled by the gas flow and the temperature of the solid KCl. The incident gas flow also affects the pressure inside the target chamber, thus influencing the stopping power of the gas. The optimum values for a capillary of 1.6 mm inner diameter were found to be: a gas flow of 400 ml/min resulting in a pressure inside the target chamber of 1450 mbar and a KCl temperature of 653°C resulting in a mean carrier particle diameter of (135±3) nm [Gru14]. The transport efficiency of fission products was determined by γ-measurements of particle collections to ∼30 %.

2.2.3 The online surface-ionization ion source

It is required by the experiments that the radionuclides under investigation are charged particles, if only for the manipulation of the kinetic energy of atoms before neutralization (i.e., at TRIGA-LASER). Besides, charged particles are much easier to manipulate in a transfer line, in particular by electromagnetic fields. Although the nuclides created by fission show a broad ionic charge distribution [WLD$^+$78], they neutralize in the moment they attach to the carrier particle. Thus, they have to be re-ionized in an ion source. At TRIGA-SPEC, different approaches are under investigation. First tests with a 2.45-GHz ECR ion source, separating the radionuclides from the carrier particle and ionizing them in-flight in an electron plasma, did not provide the required efficiency [Smo12]. Today, a surface ionization ion source is utilized, as it was developed in the 1980ies by Brügger *et al.* [BHK$^+$85]. The carrier particles with the attached radionuclides enter a hot tungsten tube, where they stick to the tube surface. The carrier particles break apart and the attached radionuclides are released. Depending on the work function W of the ionizer material and the ionization potential Φ of the atomic species, surface ionization takes place. The efficiency is predicted by a form of the Saha-Langmuir equation [LK25]. Hence, the ratio of the flux of ions n_+ to the flux of atoms n_0, leaving the surface is given by [Dre68]

$$\frac{n_+}{n_0} = \frac{g_+}{g_0} \exp^{(W-\Phi)/(k_\mathrm{B}T)}, \tag{2.4}$$

where g_+ and g_0 denote the statistical weights of the ionic and atomic states, respectively, k_B is Boltzmann constant and T the equilibrium temperature of the system. The ionization potentials for all elements are shown in Fig. 2.7. According to Eq. (2.4), atoms having a lower ionization potential Φ are easier to ionize. If Φ is too high (or W too low), a large fraction of the vaporized atoms will be neutral. The fractional amount of ionization for the major part of the elements is actually very little. Still, alkali metals and alkali earths (Li, Na, K, Rb, Cs, Ca, Sr, Ba, etc.) on hot refractory metals (Ta, W, Re, Ir, Pt, etc.) yield adequate ionization ratios.

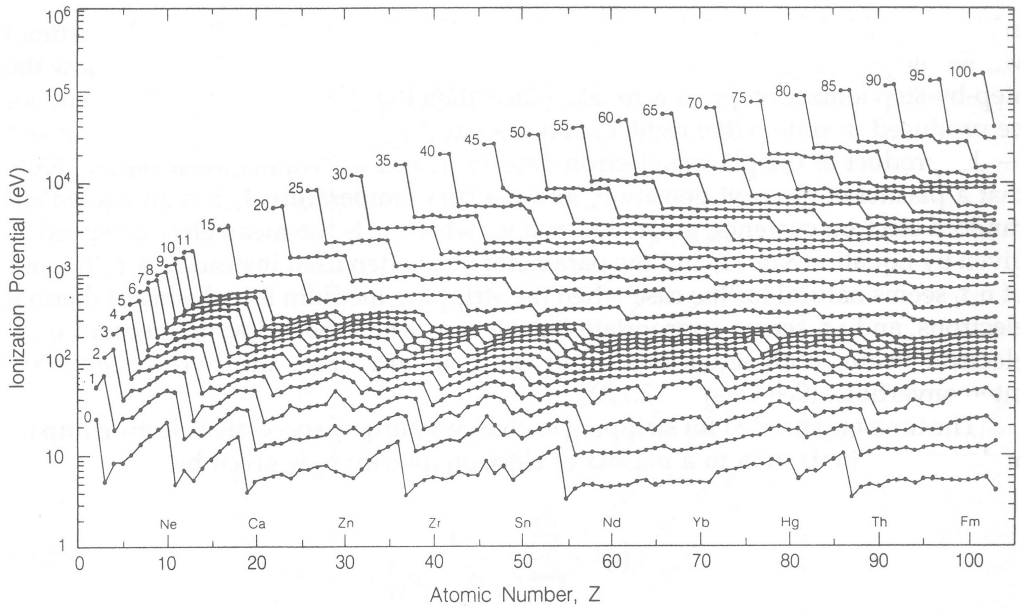

Figure 2.7: Calculated ionization potentials for all charge states of all elements, taken from Ref. [Wol95]. The data plotted in the figure were calculated by Carlson *et al.* [CJWM70].

The ionization efficiency $P_+ = n_+/(n_0 + n_+)$ [Wol95] is shown in Fig. 2.8 for K, Ca, Rb, and Sr on the ionizer materials W and Re. These elements are selected because they were mostly utilized during the commissioning phase of the TRIGA-SPEC ion beam preparation transfer line (Sec. 3). It can be seen that the ionization efficiency of Rb and K, although close to 1, degrades slowly for higher temperatures. This is a result of the shorter time that these atoms stick to the surface if the temperature is too high, increasing the number of neutral vaporized atoms n_0.

The surface ionization ion source is illustrated in Fig. 2.9. The gas jet enters the vacuum system from the left through the capillary. The angular divergence of the particle stream is a function of the particle mass, i.e., lighter particles exhibit a larger angular divergence when they exit the capillary. Thus, the use of a skimmer with a small entrance orifice greatly reduces the injection of light particles (the transport gas) into the ionizer. The vacuum chamber in front of the skimmer is connected to a large Roots pump that removes the transport gas. The heavy carrier particles are moving close to the capillary axis and may enter the ionizer through the skimmer orifice. The tungsten ionizer is heated by a tungsten filament through electron bombardment, it is floated in order to attract the electrons. It is mounted on a boron-nitride insulator, which features a high electrical resistivity ($10^9\,\Omega$cm) and a low thermal conductivity (35 W/mK). A titanium heat shield prevents the radiative heating of the vacuum chamber, and a grounded metal shield impedes the extraction of electron-impact-ionized residual-gas particles. The ionized fission products and carrier particles are extracted through a small orifice at the end of the

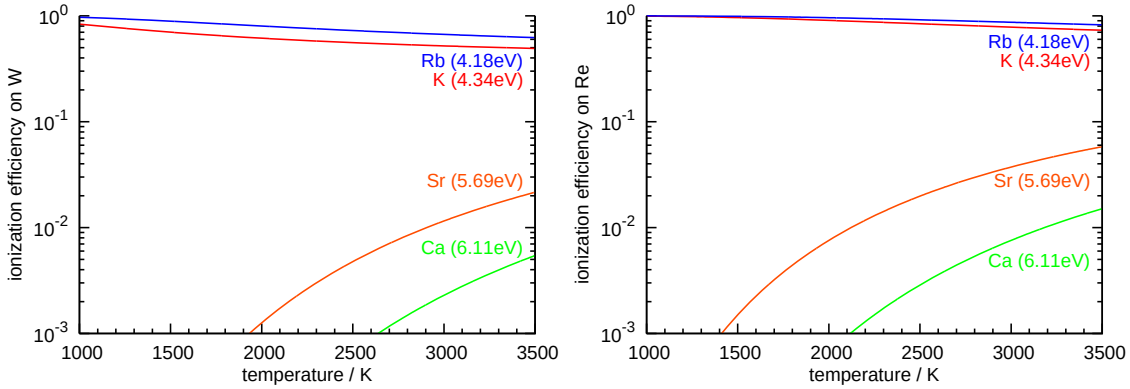

Figure 2.8: Ionization efficiencies for selected alkali metals and alkali earths on W (W_{W}=4.54 eV) and Re (W_{Re}=4.85 eV). The ionization potentials and work functions were taken from [Alt93, Wol95]. Ta can in general be used as an ionizer, but its work function is lower (4.12 eV). The work functions of Pt (5.32 eV) and Ir (5.40 eV) are very high, but their melting point is too low for practical operation.

ionizer by means of an electrostatic field (∼500-1000 V/cm). The continuous ion beam, including abundant amounts of the singly-charged carrier particle material (K^+, Ca^+, C^+, or else), is accelerated stepwise to 30 keV and guided to a dipole magnet for mass separation.

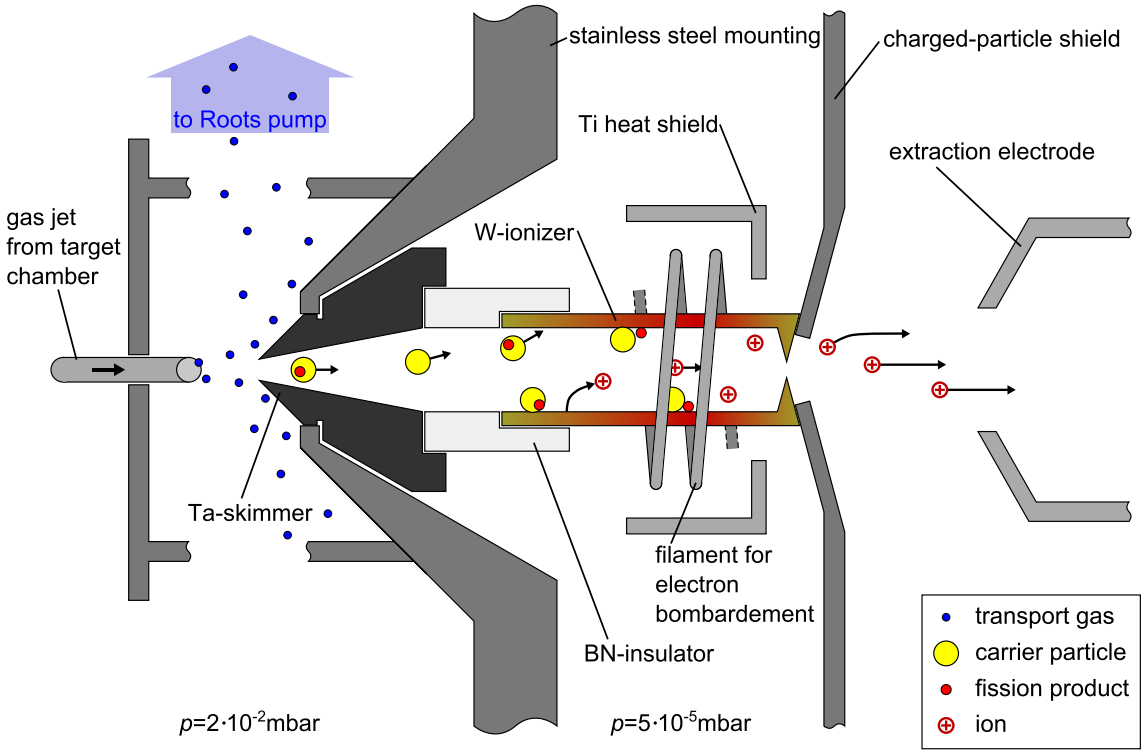

Figure 2.9: Illustration of the TRIGA-SPEC surface ionization ion source, the design was copied from the former HELIOS experiment [BHK+85].

2.2.4 The dipole magnet for isobaric separation

The ion beam generated by the surface ionization ion source contains a variety of ions, and the abundances of certain nuclides show huge differences (several orders of magnitude). It is requested by the experiments that the nuclide of interest has very little contamination for the feasibility of the measurement. Particles of different mass-to-charge ratio m/q but identical kinetic energy $E_{\mathrm{kin}}=\frac{1}{2}mv^2$ can be separated by means of a magnetic field $\vec{B}$, according to the Lorentz force acting on moving, charged particles

$$\vec{F}_{\mathrm{L}} = q\vec{v} \times \vec{B}. \tag{2.5}$$

After leaving the ion source, the ions are accelerated by a static electric potential U_{HV}=30 kV. A subsequent dipole magnet with bending radius ρ_0 and magnetic field strength $\vec{B}$ transmits ions with mass-to-charge ratio

$$\frac{m}{q} = \frac{B^2\rho_0^2}{2U_{\mathrm{HV}}} \tag{2.6}$$

on the reference trajectory. The TRIGA-SPEC dipole magnet is a 90° magnet which has a bending radius ρ_0=500 mm and supports magnetic field strengths of up to B_0=1.12 T, a photograph is shown in Fig. 2.10. It can be used for 30 keV kinetic-energy ions with m/q up to 500 u/e. The mass resolving power of the magnet

$$R = \frac{m}{\Delta m}, \tag{2.7}$$

where Δm denotes the FWHM of the transmitted mass peak, is an important characteristic. It defines the minimum separation needed to distinguish between two neighboring mass peaks. Its value depends on the bending radius, the field homogeneity (the TRIGA-SPEC magnet is specified for $\Delta B/B$=10^{-3}), and the properties of the ion beam. The TRIGA-SPEC magnet is double-focusing, causing a horizontal and a vertical focusing of the beam on its edge [Hin08]. Edge focusing of bending magnets is illustrated in Fig. 2.11. By adjusting the edge angle β, the focal planes of the horizontal and vertical plane can be superposed. The focal planes of the TRIGA-SPEC magnet are 500 mm in front and behind the magnet. To achieve the maximal mass resolving power, a vertical slit is typically installed at the exit focal point of the magnet, transmitting only one q/m trajectory. Due to space restrictions at TRIGA-SPEC, a slit could not be placed at exactly this position. Nevertheless, a movable vertical slit system is installed for optimization and commissioning purposes of the ion sources. Mass spectra of the dipole magnet are discussed in Sec. 3.1.

2.2.5 The TRIGA-SPEC RFQ cooler and buncher

The radio-frequency quadrupole (RFQ) cooler and buncher serves to reduce the emittance of the incoming continuous beam, to accumulate ions, and to prepare bunches of ions. A schematic drawing of the RFQ setup is shown in Fig. 2.12, a photograph of the installed device shows Fig. 2.13.

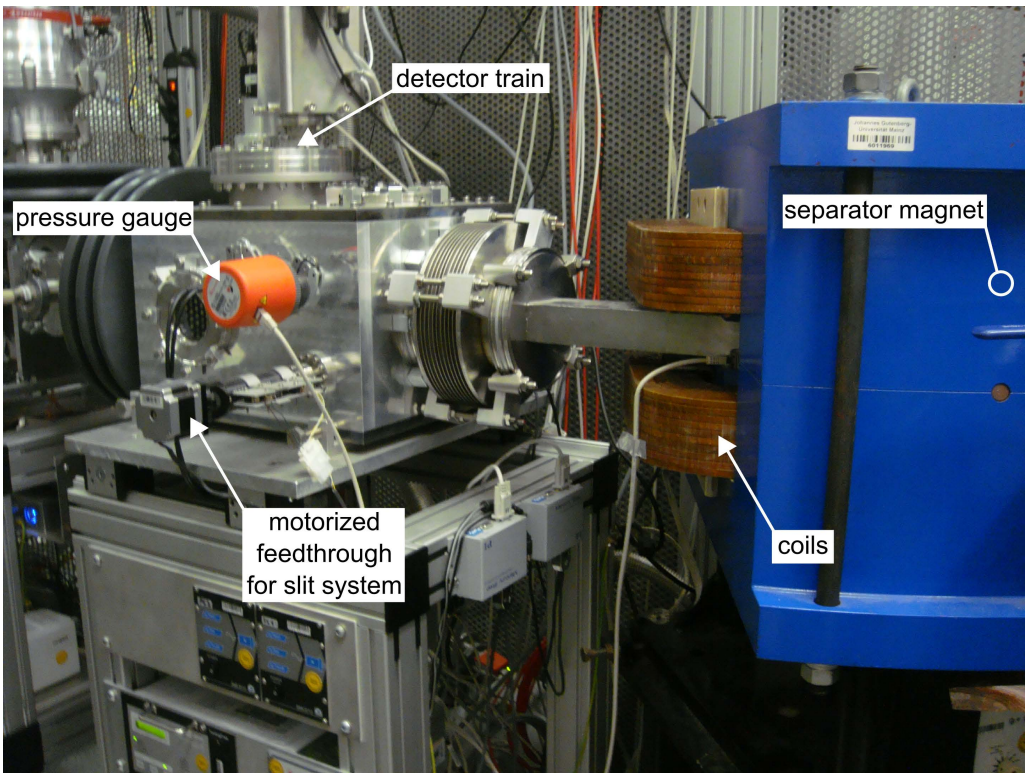

Figure 2.10: Photograph of the TRIGA-SPEC separator magnet and the subsequent slit chamber containing a motorized slit system and one of the ion beam diagnostics.

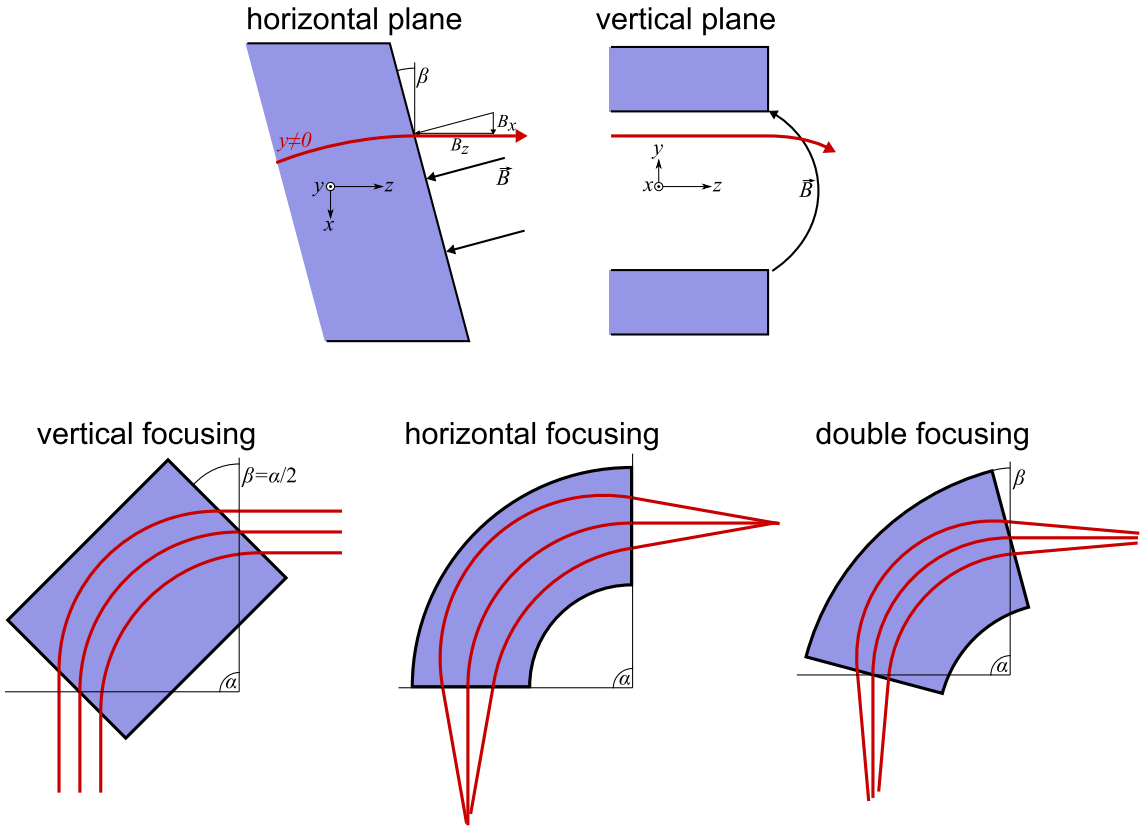

Figure 2.11: Different edge designs of α=90° bending magnets. Particles with small horizontal deviations from the reference trajectory have different path lengths inside the magnetic field, leading to horizontal focusing. Different angles of the magnet's edge β lead to vertical focusing for trajectories with $y \neq 0$ due to the x-component of the fringe field B_x.

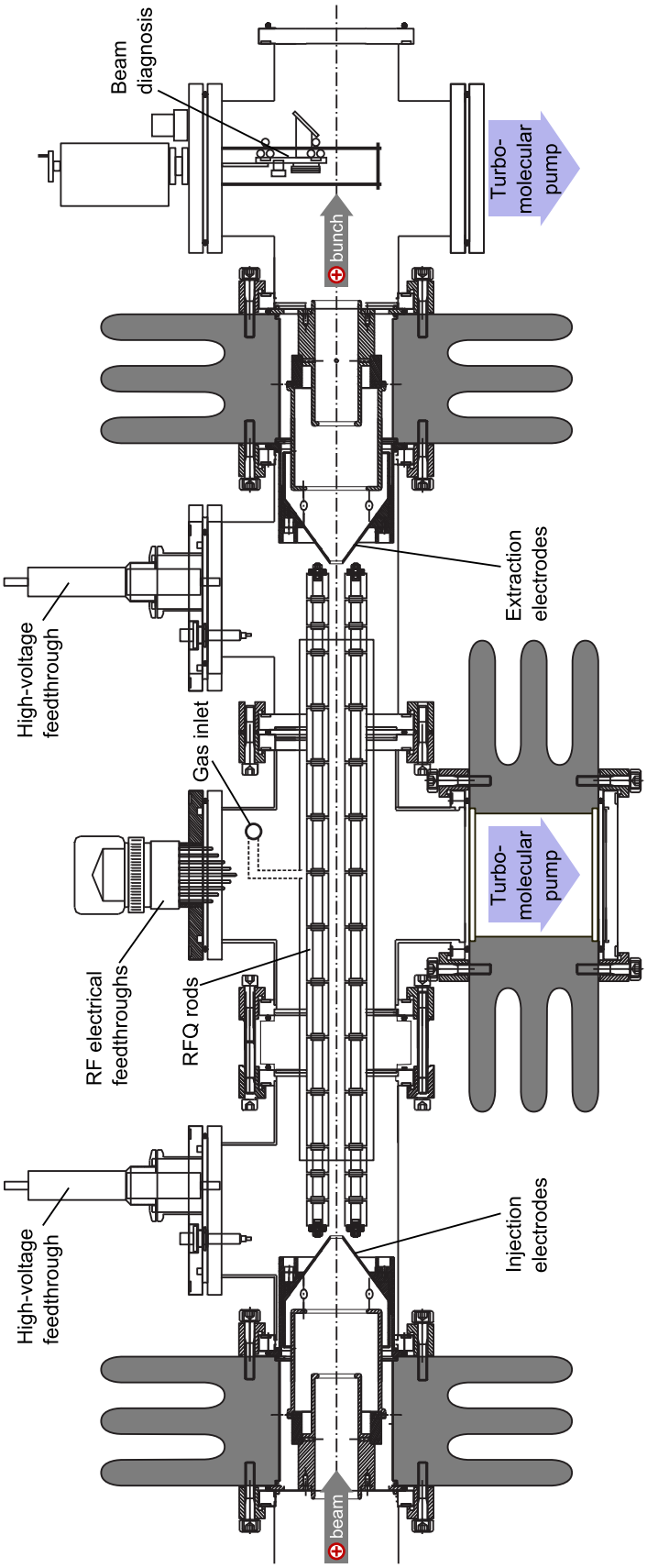

Figure 2.12: Schematic drawing of the TRIGA-SPEC RFQ [LBG+09]. Located between the gray insulators, the RFQ can be floated on high voltage (30 kV).

The hardware design follows the one of [LM99]. Ions enter the structure from the left, passing deceleration and focusing lenses for efficient injection into the central quadrupole section. The extraction and re-acceleration section mirrors the injection section. After ejection, the ion can be observed with a detection unit, or guided to the experiments. The four rods of the RFQ, separated by $2r_0$=14 mm, are seg-

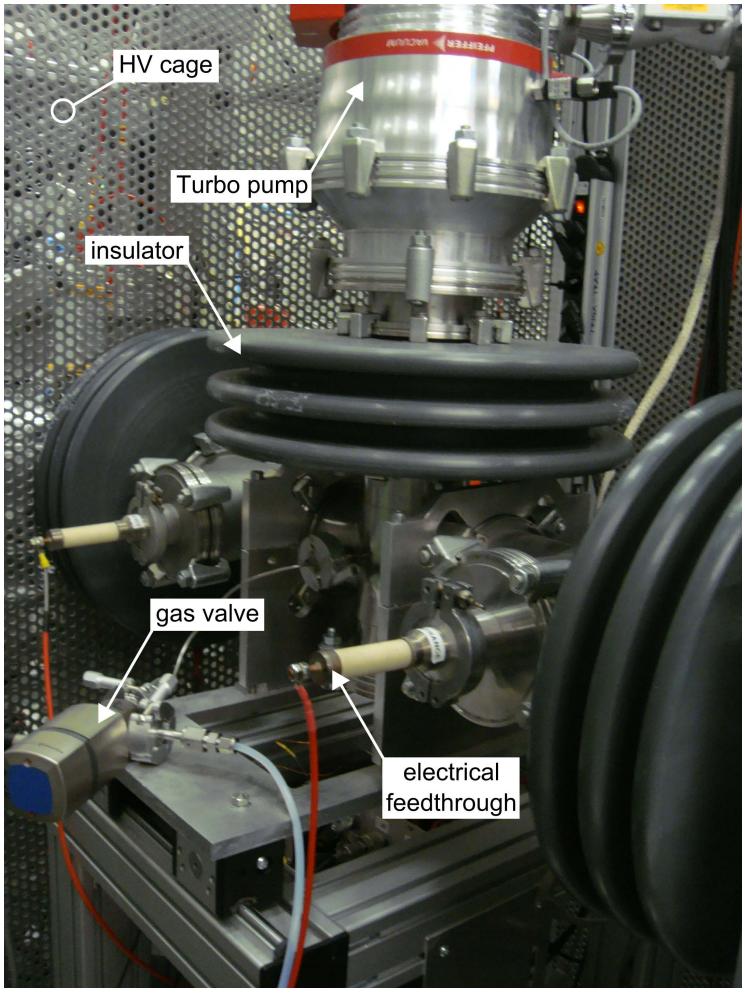

Figure 2.13: Photograph of the TRIGA-SPEC RFQ, installed at the ion beam preparation transfer line. The RFQ is located inside a high-voltage safety cage.

mented into 15 pieces each. The nine segments in the RFQ center have a length of 40 mm, while the first three and the last three segments only 20 mm. The total length of the Paul trap is 504 mm. The segmentation of the rods allows the application of DC voltages, defining an electric field gradient along the RFQ axis. Thus, radially confined ions are guided to the potential minimum. However, with an initial kinetic energy of 30 keV, the ions cannot be captured in the longitudinal potential which is only a few tens of Volts deep. Therefore, the ions are decelerated to energies on the order of 10 eV by floating the RFQ on a potential slightly below the

beam energy, with the drawback of enlarging their transverse emittance $\varepsilon_{x,y}$ in this process. To match the beam emittance to the RFQ acceptance, a pair of focusing electrodes were implemented at the entrance side. Previously the RFQ was installed at the MISTRAL experiment at ISOLDE/CERN from 2005-2009 [LBG+09], where it reduced the transverse emittance of a 60-keV beam. At TRIGA-SPEC, however, certain upgrades were added in the context of this thesis to enable the accumulation and bunching of ion beams in addition to cooling.

According to Eq. (1.32), the pseudo-potential well depth $D(r)$ for charged particles in a linear Paul trap depends on the parameters of the applied radio frequency V_{RF} and ν_{RF}. To optimize $D(r)$ for the particles of interest, V_{RF} and ν_{RF} have to be adapted according to their mass m (the charge is typically +1e after the mass separator). Stable trapping conditions can be defined by a minimal pseudo-potential well depth at the border of the trapping region, e.g., $D(r_0)\geq 6\,\mathrm{eV}$. As stated before, the Mathieu q-parameter defined in Eq. (1.27) should be ≤ 0.4 for the pseudo-potential approximation to be applicable. Applying these restrictions, the allowed combinations of V_{RF} and ν_{RF} can be translated into a contour plot for each isotope, as it is shown in Fig. 2.14. The isotopes were chosen for the following reasons: $^{40}Ca^{+}$ was

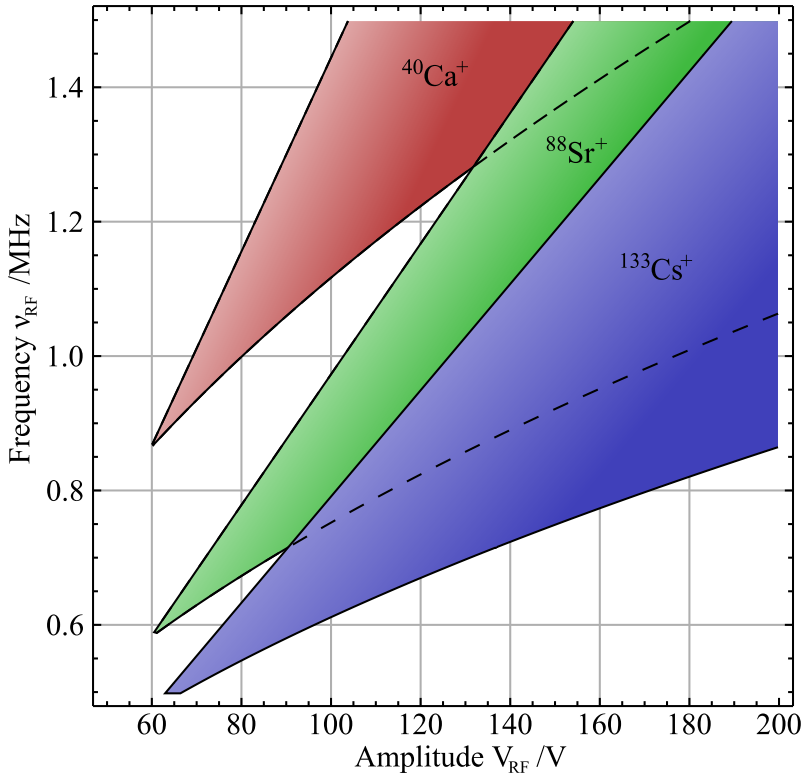

Figure 2.14: Stable trapping regions with a pseudo-potential well depth $D(r_0)\geq 6\,\mathrm{V}$ for $^{40}Ca^{+}$, $^{88}Sr^{+}$, and $^{133}Cs^{+}$ in an RFQ structure with r_0=7 mm. The color gradient denotes deeper pseudo-potential wells (i.e., darker color means deeper well).

used to characterize the RFQ cooler and buncher (Sec. 3.3). $^{88}Sr^{+}$ and $^{133}Cs^{+}$ were taken from the center of the light and heavy fission branches of the radionuclide production, respectively (Fig. 2.4). The objective of the RFQ is to provide stable trapping conditions for every possible isotope produced in the neutron-induced fission (not simultaneously, though). In the design of the RF supply circuits, a high amplification was favored over a high bandwidth to obtain the required RF amplitudes. The tuning of the RF circuit requires the commitment to a specific resonance frequency in the hardware. By the evaluation of Fig. 2.14, the resonance frequency was set to ν_{RF}=1.0 MHz. The peak-to-peak amplitude of the RF supplies can reach up to 400 V_{pp} (that is an amplitude of 200 V in the figure), enabling stable trapping conditions over the desired mass range by adjusting the RF amplitude only. Thereby, the drawback of a limited bandwidth is neglected.
Another important aspect in operating an RFQ structure is the application of the total electric potentials to the electrodes. The challenge is to simultaneously create an axial DC potential together with the radial RF potential. The TRIGA-SPEC RFQ uses a scheme where a superposition of a DC and an RF voltage is applied to each of the electrodes separately (other schemes are also possible, e.g., two sets of four rods can be used, where the DC and RF voltages are applied to a separate set of rods). The RF signal on each electrode segment has to be identical in amplitude, frequency, and phase, with a 180° shift in phase between neighboring rods (see Fig. 1.13 in Sec. 1.3). Because of feedback between the neighboring electrodes along the rod, the RF supply has to be tuned in amplitude and phase. The signal on the electrodes, tapped by an RF probe, is shown in Fig. 2.15.

When the RFQ was operated in the continuous mode at the MISTRAL experiment, a constant axial electric field gradient was employed. Within this thesis, the bunching mode has been implemented: the RFQ electronics were modified, and a potential minimum was created at the second-to-last electrode. As depicted in Fig. 2.16, the last (15) and third-to-last (13) electrodes were equipped with individual voltage supplies, custom ferrite-core RF transformers and fast transistor switches (Behlke GHTS 30[3]), enabling a fast switching of their DC potentials. The switching time of these electrodes directly translates into the temporal width of the ejected ion bunch. To accomplish short switching times, their DC potential is applied to the secondary side of the RF transformer. The RF transformers are driven by a modified KL-500 linear RF amplifier[4] to amplify their output signal. Switching times of approximately 50 ns were achieved (Fig. 2.17). The DC potentials for the remaining electrodes are applied through a resistor chain along the RFQ axis. Their RF signal is created by a similar RF transformer, driven by an ENI 2100L RF power amplifier. The mixing of the DC and the RF signals is realized through a low-pass and a high-pass filter, respectively. For a better DC voltage stability at the moment of ejection, the capture/ejection electrode (15) can be cut off from the RF supply (as shown on the right in Fig. 2.15). This upgrade enables the RFQ to cool *and*

[3]http://www.behlke.de/pdf/ghts.pdf
[4]http://www.rmitaly.com

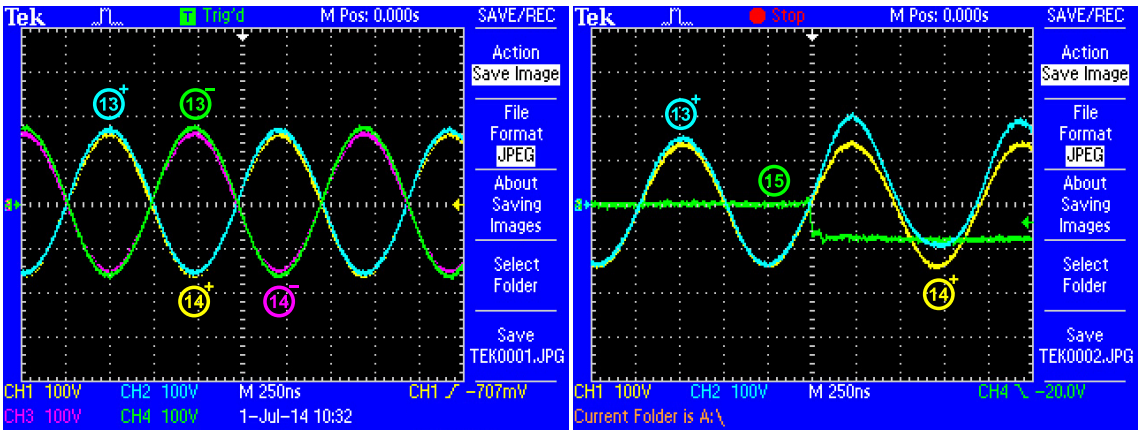

Figure 2.15: Left: RF signal applied to the electrodes of the RFQ cooler and buncher. The plot shows four signals which represent the two opposite-phase parts of the third-to-last electrode ((13)$^{+,-}$) and the second-to-last electrode ((14)$^{+,-}$). Right: Mixed DC and RF signal applied to the electrodes (13), (14), and (15). (15) is switched from $+25\,\mathrm{V_{DC}}$ to $-40\,\mathrm{V_{DC}}$ for pulse ejection. At the same time, the DC part of (13) is switched to $+40\,\mathrm{V_{DC}}$ to create a symmetric DC gradient around (14), held at $0\,\mathrm{V_{DC}}$.

accumulate an incident continuous ion beam. After the time for ion accumulation and cooling, both being defined by experimental requirements and typically on the order of a few tens of ms, the potential well around the second-to-last electrode is changed to a high electric field gradient by switching the kicking and capture electrodes as depicted in Fig. 2.16, thus ejecting the accumulated ions. The ejection frequency is therefore limited by the cooling time, in case there is sufficient supply of the ions of interest, and can be adapted to the experimental requirements. The TRIGA-LASER experiment relies on high ejection rates to improve statistical uncertainties (see Sec. 2.4). The measurement cycle of TRIGA-TRAP, however, is on the timescale of a few seconds (depending on the excitation scheme in the Penning trap, see Sec. 2.3), requiring essentially less ions per time unit.

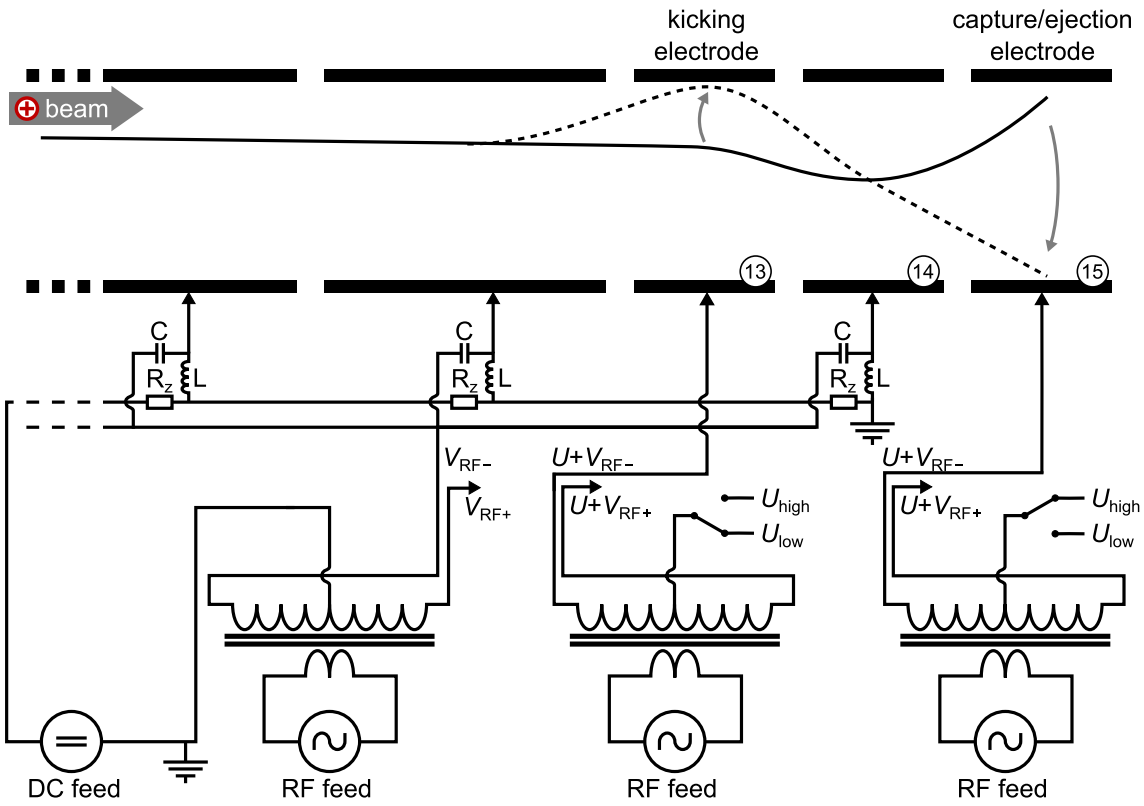

Figure 2.16: RF and DC voltage supply of the RFQ electrodes. The last (15) and third-to-last (13) electrodes, being referred to as *capture* and *kicking* electrodes, can toggle between a DC_{high} and a DC_{low} state through fast transistor switches. The values are: C=10 nF, L=390 µH, and R_z=100 kΩ.

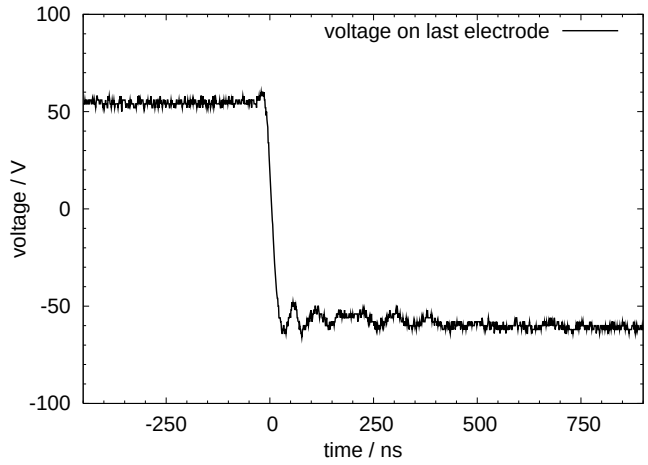

Figure 2.17: Switching pulse on the last electrode. No RF is present, thus only the DC voltage is switched.

2.2.6 Instruments for ion beam diagnosis

To optimize an ion beam and to match the beam transport system to the requirements of the experiments, instruments for ion beam diagnosis are required. Relevant beam parameters are

- Ion current
  - Ion beam current for continuous ion beams
  - Bunch current, or number of ions/bunch, for bunched ions
- Beam profile
  - Intensity distribution in transverse direction
  - Shape of the beam
- Transverse emittance
- Energy spread
- Bunch length, longitudinal emittance (bunched ions only)

Although there are still more parameters for the description of particle beams [Str92], these are important for the ion beam preparation transfer line of TRIGA-SPEC. After the ions have been created in the ion source, they form a continuous ion beam. The ion beam current is the most fundamental measure, especially after the separator magnet, to determine the presence or absence of the expected ion species in the beam. Moreover, a rough adjustment of the ion optics can be performed when the current is monitored on or after an orifice in the beam line. The design of a Faraday cup for ion beams of several tens of keV kinetic energy is rather simple: the ions are collected in an electrically insulated metal cup that is connected to ground (GND) through a calibrated resistor (typically 10^9–$10^{11}\,\Omega$). The drain of the deposited charge through the resistor can then be measured by an appropriate electronic circuit, e.g., an electrometer or voltage amplifier. To avoid the emission of secondary electrons (that will add up to the deposited positive charges on the cup), a negative-biased "suppressor" electrode can be installed to force the electrons back to the cup (another way is to bias the cup together with the measurement electronics). The principle is illustrated on the left of Fig. 2.18. The Faraday cup's sensitivity is limited mainly by the read-out electronics, the typical lower limit for the ion beam current is around 1 pA. However, the Faraday cup is a very robust device, and not prone to damage originating from high ion currents. For ion currents lower than 1 pA, multichannel plate (MCP) detectors can also be used. The principle is illustrated in Fig. 2.18, on the right. The MCP is an array of 10^4–10^7 miniature parallel electron multipliers (each has 10–100 µm inner diameter, the ratio of channel length over diameter L/d is 40–100) [Wiz79]. The channels are perpendicular to the surface, biased by a small angle ($\sim 8°$), and are typically fabricated from semiconducting lead glass. The front and rear surfaces are metal coated to serve as

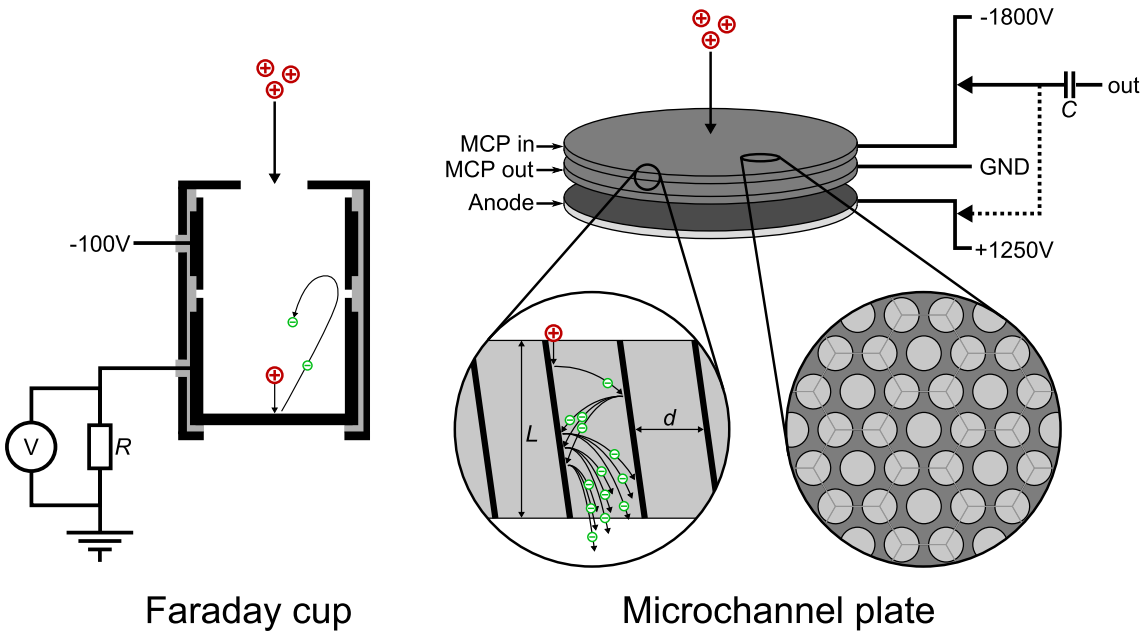

Figure 2.18: Left: principle of a Faraday cup. The repeller voltage forces the secondary electrons back to the cup. Thus, the charge drain is caused only be the incident ions. Right: principle of an MCP detector. The voltages to the MCP plates and the anode can also be applied in different ways. The avalanche created by an incident ion on the MCP causes a voltage drop equal to the charge that the electrons carry away towards the anode. This signal can be measured by a capacitive coupling to the supply cable.

input and output electrodes, the total resistance of the plate is in the range of 30–150 MΩ. If the proper voltage is applied between the two surfaces, an incident particle hitting the channel walls produces secondary electrons that are accelerated along the channel and set off an avalanche. The total gain is the number of emitted electrons per incident particle. It is in the order of 10^3 depending on the applied voltage and the channel geometry. In chevron assembly, two plates are mounted on top of each other, with the channel bias angle at inverse orientation. Thereby, the total gain is increased to 10^6, making the signal easy to detect with conventional electronics. After the release of an avalanche, the MCP channels need some time to recharge ($\sim 10^{-2}$ s per channel, yielding $\sim 10^{-7}$ s of effective dead time provided the incident flux is uniformly distributed over the active area). Thus, the MCP is best suited for single-particle detection, or count rates up to 10^7/s (corresponding to a continuous beam of ∼1.6 pA). The detection efficiency of an MCP for positive ions depends on their kinetic energy. For the transport energy of TRIGA-SPEC (30 keV), the detection efficiency is about 70–80% [Fra02]. However, the absolute ion beam current can not be determined with MCPs due to the channel's dead time.

At TRIGA-SPEC, three detector units involving a moveable detector wagon are installed. They combine a Faraday cup with an MCP detector, which is equipped with a phosphor screen for a visual beam detection. The wagon has three positions:

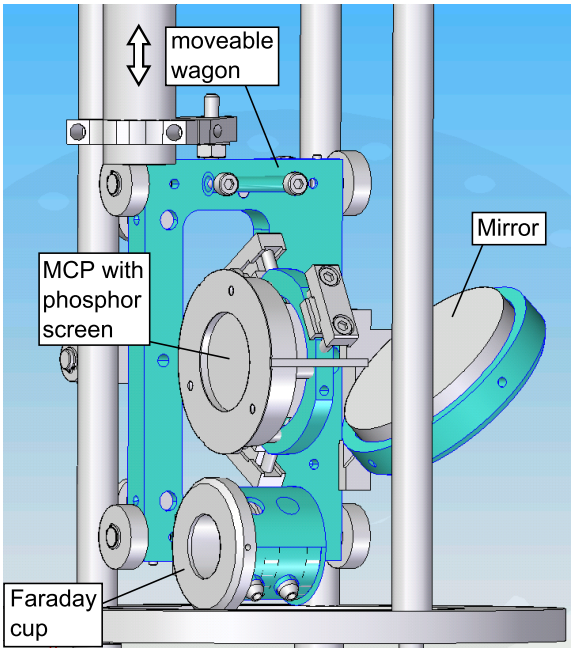

Figure 2.19: The detector wagon used at TRIGA-SPEC. For details, see the text.

the Faraday cup is in the beam line, the MCP detector is in the beam line, or the detectors are out of the beam line for full beam transmission. Two of these detection units are installed at the ion beam preparation transfer line, the third is installed at TRIGA-LASER.

With this unit, several parameters of continuous and bunched beams can be measured. The intensity of continuous beams is typically measured with the Faraday cup, both after the separator magnet for the recording of mass spectra and for the determination of the cooling efficiency after the RFQ cooler and buncher. Low-intensity continuous beams can be detected by measuring the count rate on the MCP detector. Of particular interest is the visual beam detection with the phosphor screen. For every electron impinging on its surface, several hundred fluorescence photons are emitted, creating a picture of the beam's intensity distribution. For ease of use, the picture is recorded by a CCD camera outside of the vacuum chamber via a mirror. In principle, also the transverse emittance can be determined by measuring the beam diameter at two subsequent positions in the beam line. The visual detection is also possible for ion bunches, although the camera has to be triggered for proper detection. The size of the bunch, i.e., the number of ions in one bunch, can be measured on the Faraday cup in combination with a calibrated charge amplifier at the Faraday cup's readout electronics.

The detection techniques mentioned so far are destructive regarding the ions. Non-destructive methods for ion detection are possible at TRIGA-LASER, as the energy spread and the length of an ion bunch can be measured using laser-spectroscopic methods. Additionally, there are detection techniques utilized at TRIGA-SPEC that involve the detection of radioactive isotopes. As an example, a 30 keV continuous beam can be implanted on an aluminum foil for a specified period of time. By measuring the energy and intensity distribution of photons emitted from the foil afterward, the radioactive isotopes can be identified by their spectroscopic lines, and the number of radioactive ions that were implanted can be calculated by their intensities.

2.2.7 The 45° electrostatic switchyard

The last section of the ion beam preparation transfer line has the task to distribute the well-prepared ion bunches to the experiments TRIGA-TRAP and TRIGA-LASER. This is done be the switchyard, of which a 3D model is shown in Fig. 2.20. The switchyard has three exits, one straight ahead (used by TRIGA-TRAP) and two with a total bending angle of 45° to the right (TRIGA-LASER) or left (not in permanent use; can be used for, e.g., additional beam diagnosis). The switchyard

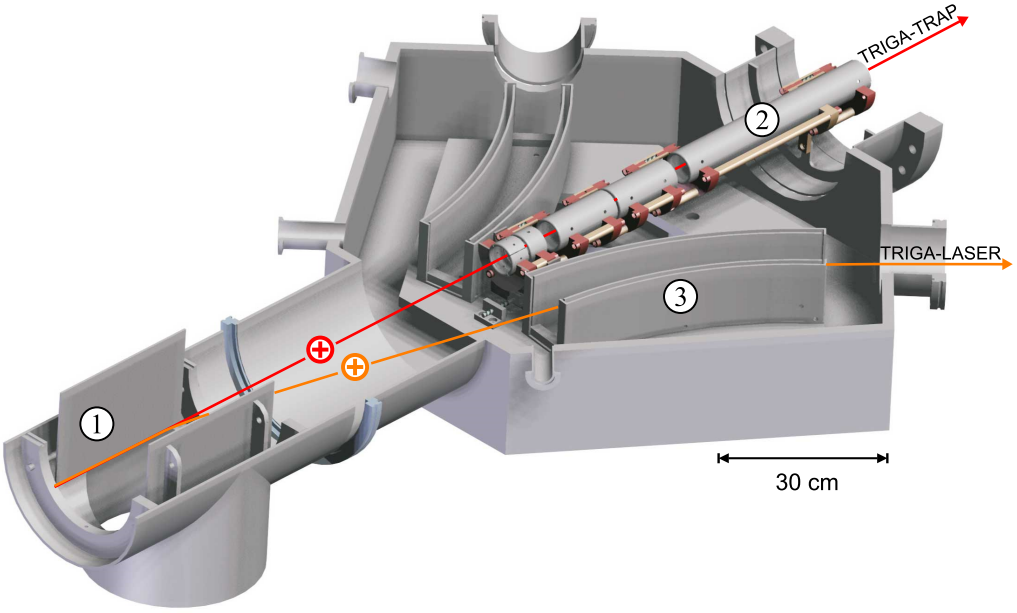

Figure 2.20: 3D model of the TRIGA-SPEC switchyard, adapted from [Smo12]. It consists of a two-stage deflection unit: the pre-kicker (1) and the main deflector (3). The straightforward deceleration stage (2) is required for the injection of ions into the Penning traps.

was designed with long, curved main deflectors to provide sufficiently strong electrostatic fields for the deflection of 30-keV ion bunches [Krä10]. One aspect of the

switchyard is to allow parallel operation of the two experiments, i.e., the direction of the ions can be alternated on the timescale of the RFQ ejection frequency. Therefore, a pair of electrodes acting as horizontal "pre-kicker" determines the entrance location to the switchyard chamber by an 8° deflection. Afterward, the curved main deflectors make for the remaining 37°. They are electrically shielded toward the rest of the chamber, thus their potentials can stay applied when the ions are directed to a different path. The ions' direction is solely controlled by the deflection of the pre-kicker, a comparably small electrode with low capacitance that can be switched by standard high-voltage switches in the order of microseconds. The switchyard chamber also contains an electrostatic deceleration stage, which is required for the TRIGA-TRAP experiment only (Sec. 2.3.3).

2.3 The Penning-trap mass spectrometer TRIGA-TRAP

The Penning-trap mass spectrometer TRIGA-TRAP is used routinely to determine masses and mass differences of various nuclides with a relative precision of about 10^{-8} [KAB+11, SBB+12]. These measurements are performed using the well established time-of-flight ion-cyclotron-resonance technique (TOF-ICR) [KBK+95]. Comprehensive reviews on the progress and achievements of Penning-trap mass spectrometry (PTMS) can be found in [Bla06, BNW10, BDN13]. Generally spoken, Penning-trap mass spectrometers are leading in both mass resolving power and mass accuracy, sharing the fame only with storage rings for mass spectrometry like the ESR at GSI/Darmstadt [HAB+00, LGR+05]. The fundamental advantage of Penning-trap and storage-ring mass spectrometry is the conversion of the mass measurement into a frequency measurement, a quantity that can be determined with utmost precision [SD56]. The fundamental principle of PTMS is given in this section, a good review on storage-ring mass spectrometry is the one by Franzke *et al.* [FGM08].

2.3.1 Principles of Penning-trap mass spectrometry (PTMS)

The Penning trap is in some respect similar to the Paul trap discussed in Sec. 1.3: particles of interest are spatially confined in a 3D trap. While this is accomplished by alternating electric fields in the Paul trap, it is done by the superposition of a homogeneous magnetic field for radial confinement and an electrostatic quadrupole field for axial confinement in the case of the Penning trap. The principle of Penning traps is well covered in literature, but the basics will be presented to understand the mass measurement process. Well-established textbooks on the topic are the ones by Ghosh [Gho95] or Major *et al.* [MGW05], detailed review articles on (singly-) charged-particle storage in Penning traps are those by Brown and Gabrielse [BG86] or Kretzschmar [Kre92b, Kre92a]. TRIGA-TRAP was described in detail in the theses of Ketelaer [Ket10], Smorra [Smo12], and Eibach [Eib13].

Like in a dipole magnet, an ion of charge-to-mass ratio q/m and a non-zero velocity component perpendicular to the direction of the magnetic field experiences the Lorentz force (Eq. (2.5)). If the magnetic field is sufficiently strong and electric fields are absent, the ion is confined in the radial direction perpendicular to the field lines of $\vec{B}=\vec{B}_z$, performing a circular motion on the so-called cyclotron orbit with the free cyclotron frequency

$$\omega_\mathrm{c} = \frac{q}{m}B. \tag{2.8}$$

The confinement in the direction of the magnetic field z is realized by the addition of an electric quadrupole potential of the form

$$\Phi(z,r) = U_0\frac{z^2 - r^2/2}{2d^2}, \tag{2.9}$$

expressed in cylindrical coordinates (in contrast to the linear Paul trap, the Penning trap is axially symmetric). U_0 denotes the applied DC voltage, where $qU_0{>}0$ for a confining potential, and d the characteristic trap dimension given by

$$d^2 = \frac{1}{2}(z_0^2 + r_0^2/2), \tag{2.10}$$

with z_0 and r_0 being the minimum distance between the center of the trap and the endcap and ring electrodes, respectively (see Fig. 2.21). In a classical approach, the

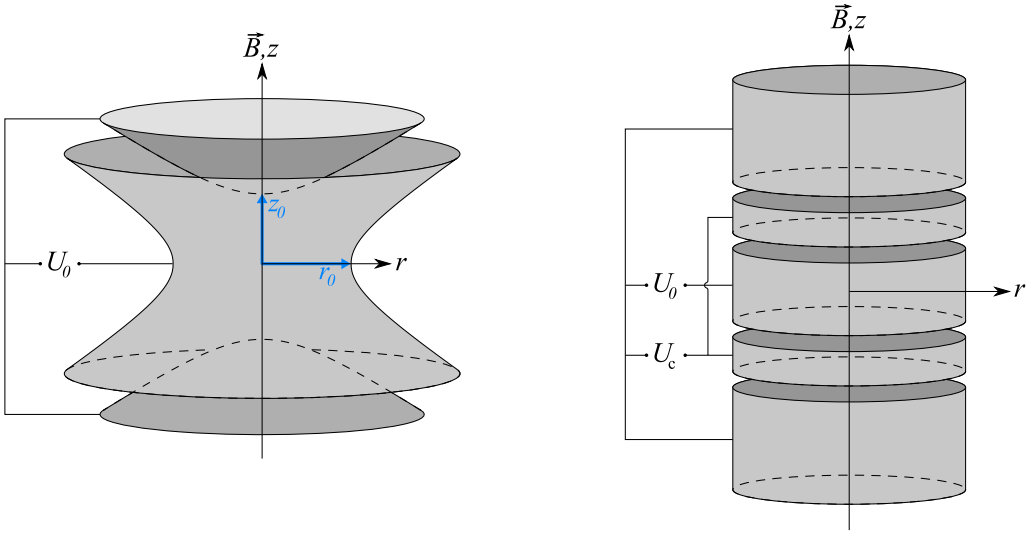

Figure 2.21: Possible electrode geometries for Penning traps. Left: hyperbolic trap, the shape of the endcap is given by the hyperbola of revolution $z^2{=}z_0^2{+}r^2/2$ and the shape of the ring electrode by $z^2{=}(r^2{-}r_0^2)/2$. Right: cylindrical trap with correction electrodes.

axial motion of a charged particle is a simple harmonic motion, decoupled from the magnetic field. Thus, the equation of motion can be written as

$$m\ddot{\vec{z}} = q\vec{E}_z, \text{ where } \vec{E}_z = -\frac{U_0}{d^2}\vec{z}. \tag{2.11}$$

The radial motion of the charged particle is described by

$$m\ddot{\vec{r}} = q(\vec{E}_r + \dot{\vec{r}} \times \vec{B}), \text{ where } \vec{E}_r = \frac{U_0}{2d^2}\vec{r}. \tag{2.12}$$

$\vec{E}_r$ denotes a *repulsive* radial potential created by the electric quadrupole field, having three consequences. First, the frequency of the cyclotron motion ω_c (Eq. (2.8)) is reduced, because the centripetal force is decreased. Second, the cyclotron orbit is superimposed upon a much slower, circular magnetron orbit. Therefore, the total motion is a compound motion of three independent modes, as illustrated in Fig. 2.22: (1) the harmonic oscillation along the trap axis with oscillation frequency

ω_z (axial frequency), (2) the cyclotron motion at the reduced cyclotron frequency ω_+ (modified cyclotron frequency), and (3) the magnetron motion at the magnetron frequency ω_-. Third, the magnetron motion is unbound, as it is an orbit around the

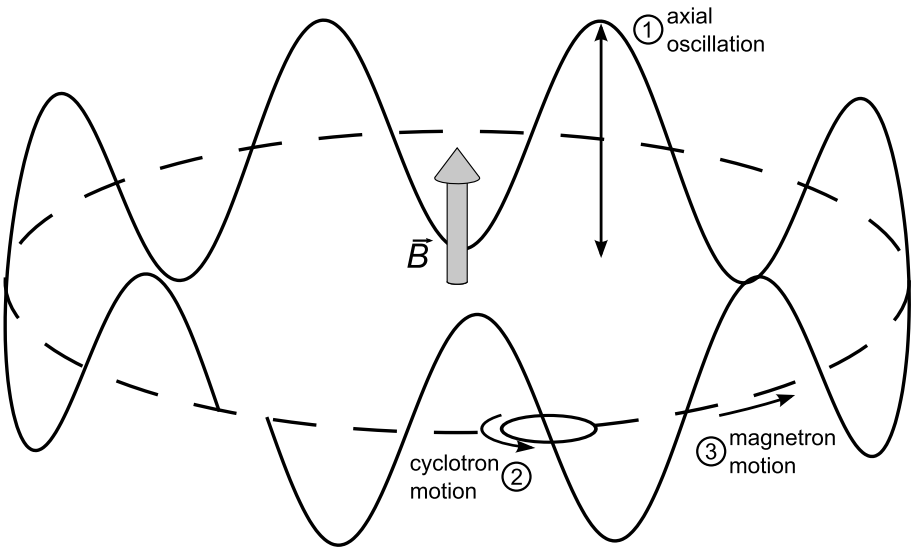

Figure 2.22: Orbit of a charged particle in a Penning trap. The three independent eigenmotions of the particle are shown (not to scale).

top of a radial potential hill. Any dissipative process (i.e., processes that remove energy from the magnetron motion) will cause the magnetron radius to increase until the particle hits the ring electrode. Due to its low frequency, the magnetron motion is effectively stable against radiation damping (thus, the particle does not get lost in the ideal Penning trap for years) [BG86], but artificially introduced dissipative forces (like the application of collisional cooling) have to consider the magnetron motion's unbound nature. For an ideal Penning trap in the non-relativistic case, the three eigenfrequencies are

$$\omega_z = \sqrt{\frac{qU_0}{md^2}}, \tag{2.13}$$

$$\omega_+ = \frac{1}{2}\left(\omega_\mathrm{c} + \sqrt{\omega_\mathrm{c}^2 - 2\omega_z}\right) \approx \omega_\mathrm{c} - \frac{U_0}{2d^2B}, \tag{2.14}$$

$$\omega_- = \frac{1}{2}\left(\omega_\mathrm{c} - \sqrt{\omega_\mathrm{c}^2 - 2\omega_z}\right) \approx \frac{U_0}{2d^2B}, \tag{2.15}$$

where $\omega{=}2\pi\nu$. For a bound particle motion, the roots in Eqs. (2.14)-(2.15) must be real, so

$$\omega_\mathrm{c}^2 - 2\omega_z > 0. \tag{2.16}$$

Combining Eq. (2.8) and Eq. (2.13) into Eq. (2.16) yields the conditions for stable confinement of charged particles (the second equation was stated earlier in the text)

A /u	ν_+ /MHz	ν_z /kHz	ν_- /kHz
40	2.669	129.6	3.149
85	1.254	88.93	3.153
88	1.211	87.40	3.153
133	0.800	71.10	3.158

Table 2.1: Eigenfrequencies ν_i=$\omega_i/2\pi$ of singly charged ions (the nuclides of Fig. 2.14 and $^{85}Rb^+$) for the TRIGA-TRAP hyperbolic Penning trap ("precision trap"). The trap parameters are B=7 T, U_0=7 V, d=5.03 mm.

$$B > \sqrt{\frac{2mU_0}{qd^2}},\ qU_0 > 0. \tag{2.17}$$

The following relations apply to the eigenfrequencies in an ideal Penning trap

$$\omega_c = \omega_+ + \omega_-, \tag{2.18}$$
$$\omega_z^2 = 2\omega_+\omega_-, \tag{2.19}$$
$$\omega_c^2 = \omega_+^2 + \omega_z^2 + \omega_-^2, \tag{2.20}$$

where the last one is the so-called *invariance theorem* [BG82] and retains its validity even under certain deviations from the ideal trap. Typical field parameters induce a hierarchy for the magnitude of the eigenfrequencies:

$$\omega_c > \omega_+ \gg \omega_z \gg \omega_-. \tag{2.21}$$

2.3.2 The Penning-trap setup at TRIGA-TRAP

For the trap parameters of TRIGA-TRAP, the magnitudes of the frequencies ν_+, ν_z, and ν_- are listed in Table 2.1. The free cyclotron frequency ω_c has to be determined to extract the mass from Eq. (2.8), however, ω_c is not an eigenfrequency of the Penning trap. Thus the Eqs. (2.18)-(2.20) are used to derive the free cyclotron frequency from the eigenfrequencies of the trap. Finally, the strength of the B-field has to be determined with high precision. It is therefore calibrated with a cyclotron frequency measurement of an ion of well-known mass m_{ref} under identical conditions. The mass of the atom of interest m_{atom} is then obtained by

$$m_{atom} = (m_{ref} - m_e)\frac{\omega_{c,ref}}{\omega_{c,ion}} + m_e, \tag{2.22}$$

where m_e denotes the electron mass, $\omega_{c,ref}$ and $\omega_{c,ion}$ the cyclotron frequencies of the reference ion and the ion of interest, respectively, and B has canceled out under the assumption that the magnetic field stayed constant during the time of the measurements.

The hyperbolic geometry of a Penning trap has advantages and drawbacks. On the one hand, hyperbolic electrodes are equipotentials of the desired ideal quadrupole potential. On the other hand, precise manufacturing of a hyperbolic trap is very challenging. There are significant deviations from the pure quadrupole potential due to surface imperfections, misalignment, and holes in the electrodes for particle in- and ejection. Thus, the precision trap of TRIGA-TRAP is equipped with correction electrodes to compensate for these imperfections (Fig. 2.23 shows a 3D model of the precision trap on the right). As a simple alternative to the hyperbolic trap geometry, Tan and Gabrielse [TG89] proposed a compensated 5-pole cylindrical Penning trap, as depicted in Fig. 2.21 on the right. The axially symmetric electrodes have identical inner diameter, their lengths are mirror-symmetric w.r.t. the trap center. Obviously, cylindrical electrodes can be machined to higher precision. Their electrostatic properties can be calculated analytically: for a cylindrical trap, Eq. (2.9) is extended, yielding the potential near the trap center [TG89, KEH+14]

$$\Phi(r',\theta) = U_0\frac{z^2 - r^2/2}{2d^2} + \frac{1}{2}U_0 \sum_{k\geq 0\,\text{even}}^{\infty} C_k \left(\frac{r'}{d}\right)^k P_k(\cos\theta). \tag{2.23}$$

The second term represents the unwanted additions to the trap potential of order k (where k is even due to the mirror symmetry), expressed in spherical coordinates (r',θ) and Legendre polynomials $P_k(x)$. The trap parameters (d, U_0, and U_c) are chosen in a way that orders of C_k with $k > 2$ are minimized (a Penning trap where the parameters are chosen such that $C_{4,6}$=0 is called *compensated*). Cylindrical Penning traps also have the advantage of open endcaps, making the loading of ions into the trap easier. TRIGA-TRAP is a double Penning-trap setup, with a cylindrical Penning trap used for isobaric cleaning and a hyperbolic Penning trap for the actual mass measurement. A hyperbolic trap has, compared to a cylindrical trap, a larger inner volume without field inhomogeneities (in cylindrical traps, $C_{k>6}$ cannot be suppressed simultaneously with $C_{4,6}$=0), enabling larger unperturbed radii of ion orbits.

The double Penning-trap system is shown in Fig. 2.23. At TRIGA-TRAP, the cylindrical Penning trap consists of seven electrodes providing two more degrees of freedom for the tuning of the quadrupole field. The quadrupole field of the hyperbolic trap can be adjusted with four additional correction electrodes.

Ion manipulation in Penning traps

It is necessary to manipulate the ion's eigenmotions in the trap for the cyclotron frequency measurement process. This can be accomplished by the application of AC potentials. For example, the axial frequency ω_z can be excited by applying an AC potential to the endcap electrodes. For the excitation of the radial motions, however, the center electrode of the Penning trap has to be segmented, as it is shown in Fig. 2.24. A single eigenmotion in the Penning trap can be excited by a resonant dipole AC field. The field can be created by an AC potential at two

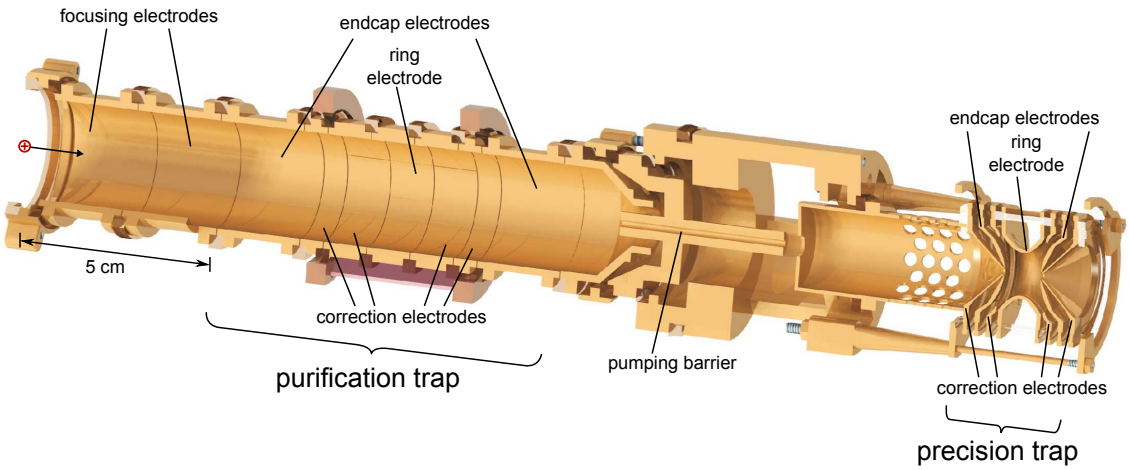

Figure 2.23: 3D model of the Penning traps of the TRIGA-TRAP experiment, adapted from [Smo12]. Ions enter the cylindrical purification trap from the left, where isobaric cleaning is performed. The high vacuum in the precision trap on the right is protected from the purification trap's buffer gas by the pumping barrier.

opposite segments of the center electrode with amplitude V_d, frequency ω_d, and a ϕ_d=180° shift between the segments. The field is then of the form [BG86]

$$\vec{E}_x = -\frac{\kappa}{2r_0} V_\mathrm{d} \cos(\omega_\mathrm{d} t + \phi_\mathrm{d}) \hat{x}, \tag{2.24}$$

where κ denotes a dimensionless constant of order unity that depends on the geometry of the trap (κ=1 if the opposing electrode segments were flat plates with no screening from other electrodes). Thereby, the radial motions can be excited mass-selectively, however, the magnetron motion is almost mass-independent according to Eq. (2.15). The excitation of the magnetron motion thus affects all ion species simultaneously.
The quadrupole excitation at the sum of two individual eigenfrequencies can couple the eigenmotions, for example ω_c=ω_++ω_- (Eq. (2.18)). The coupling is achieved by a quadrupole potential, applied to the segments of the ring electrode as depicted in Fig. 2.24 on the right. Derived from a potential like the one in Eq. (1.18), the field is of the form

$$\vec{E}_x = -\frac{2\kappa^2}{r_0^2} V_\mathrm{q} \cos(\omega_\mathrm{q} t + \phi_\mathrm{q}) x, \tag{2.25}$$

$$\vec{E}_y = +\frac{2\kappa^2}{r_0^2} V_\mathrm{q} \cos(\omega_\mathrm{q} t + \phi_\mathrm{q}) y. \tag{2.26}$$

If ω_q=ω_c, a full periodic conversion between the radial motions is obtained [KBK+95]. Figure 2.25 shows the calculated trajectory of an ion excited by a quadrupole field at frequency ν_c, starting from a pure magnetron motion. After the conversion time

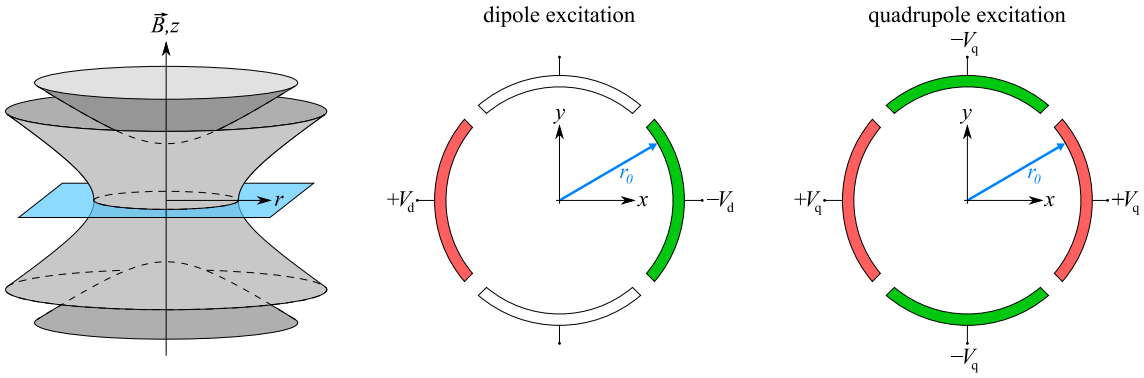

Figure 2.24: Segmented center electrode of a Penning trap, shown in the r-plane. The colors red and green mark 180° phase shifts of the applied AC voltages V_d and V_q, respectively.

period

$$T_{\text{conv}} = \frac{4\pi r_0^2 B}{\kappa^2 V_q}, \tag{2.27}$$

the magnetron motion is completely converted into cyclotron motion, with the cyclotron motion's amplitude being equal to the former magnetron amplitude.

Measurement of the TOF-ICR at TRIGA-TRAP

The purpose of the cylindrical purification trap is to free the ion ensemble from contaminant ion species that can perturb the eigenfrequencies of the nuclide of interest due to ion-ion interactions [BKK+92]. To this end, collisional cooling by the introduction of a buffer gas into the purification trap is utilized as proposed by Savard [SBB+91]. The principle of collisional cooling was presented in Sec. 1.2.3, and the description as a viscous drag force was treated in Sec. 1.3.4. The viscous damping force is velocity-dependent (Eq. (1.34)), thus ion motions with higher angular velocities $|\vec{v}| \propto \omega$ like the modified cyclotron frequency are cooled more efficiently. However, also the magnetron motion is damped, resulting in a growing magnetron radius (as it is unbound). The growing radius is counteracted by the application of a quadrupole field at the sum frequency of $\nu_+ + \nu_-$. Thus, the magnetron motion is converted into the quickly cooled cyclotron motion. Effectively, all three eigenmotions are cooled until the ions are in thermal equilibrium with the buffer gas and centered in the trap (in the case of TRIGA-TRAP, the He buffer gas is cooled by liquid nitrogen to 77 K). Due to the quadrupole excitation that involves the modified cyclotron frequency ω_+, the process is mass-selective, making it extremely useful for the preparation of high-precision measurements. Depending on the excitation time and the strength of the damping force, the mass resolving power is in the range of 10^4-10^5 for A=120 u ions [GBB+11].

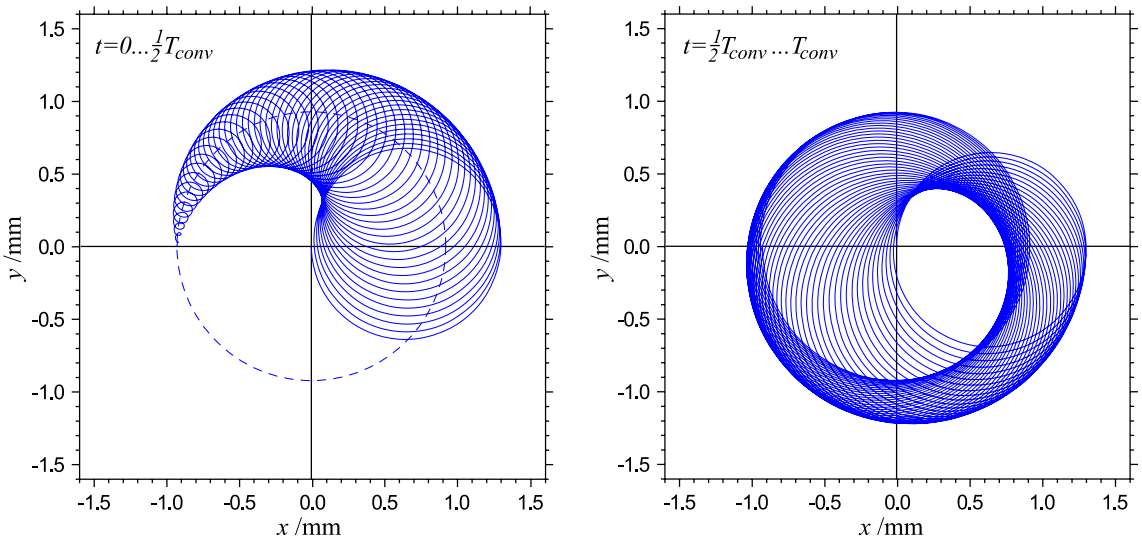

Figure 2.25: Calculated conversion of a pure magnetron motion into a pure cyclotron motion, caused by quadrupole excitation at frequency ν_q=ν_c. The left and right graph each show one half of the conversion cycle. The dashed line on the left shows the initial magnetron orbit for comparison. Adapted from [Bla06].

The ions with desired mass can be transferred through the small orifice of the pumping barrier into the precision trap. For the determination of the cyclotron frequency, the time-of-flight ion-cyclotron-resonance (TOF-ICR) technique is applied [GKT80]. It is based on the magnetic moment of the ion inside the magnetic field of the Penning trap. The magnetic moment $\vec{\mu}$ created by an electric charge on a circular orbit is given by

$$\vec{\mu} = \frac{q}{2}\vec{r} \times \vec{v} = \frac{q}{2} r^2 \vec{\omega}, \tag{2.28}$$

where $\vec{\omega}$ denotes the angular frequency of the charge q. In a Penning trap, ω can consist of ω_-, ω_+, or a superposition of the two. When the ions are ejected from the trap and transported towards a detector at the end of the beam line , they pass a magnetic field gradient as illustrated in Fig. 2.26. The magnetic field gradient creates an axial force acting on the ion that is proportional to its magnetic moment:

$$\vec{F}_{\nabla B} = -\vec{\mu}\left(\vec{\nabla}\vec{B}\right) \propto r^2\omega. \tag{2.29}$$

As the magnetic field gradient is negative, the axial force on the ion is positive and will accelerate it, changing the time of flight to the detector depending on ω. A full measurement cycle of the TOF-ICR is the following:

1. the Penning trap is loaded with the cooled and cleaned ion species,

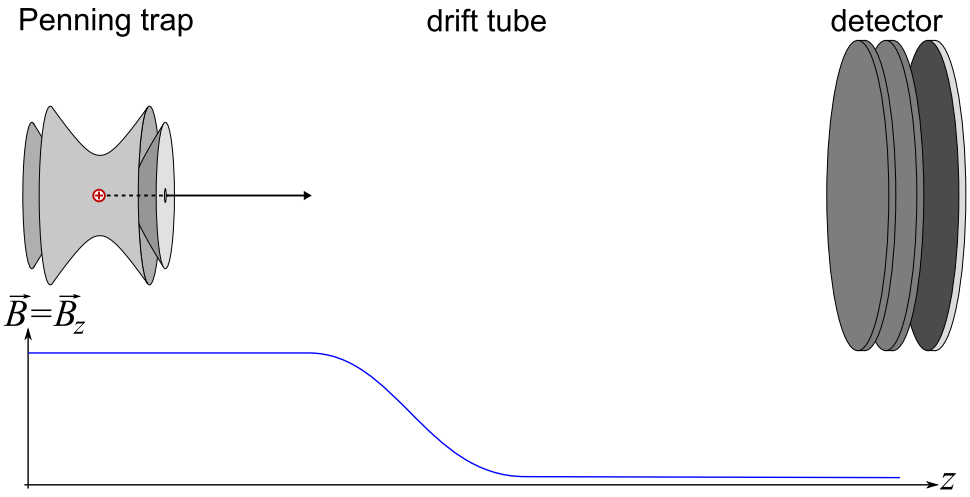

Figure 2.26: Illustration of the TOF-ICR measurement technique. For details, see the text.

2. the ions are prepared at a well-defined magnetron orbit with radius r_- via dipole excitation at $\nu_\mathrm{d}=\nu_-$,

3. the magnetron motion is converted into cyclotron motion by quadrupole excitation, depending on how close ν_q is to $\nu_+ + \nu_-$,

4. the ion is ejected from the trap and passes the magnetic field gradient,

5. the time of flight from the ejection to the moment of detection is recorded.

The measurement process is repeated multiple times while ν_q is varied around $\nu_+ + \nu_-$. While ν_q is off-resonant, zero or partial conversion takes place. On resonance, however, the motion is completely converted and the ion circulates at ν_+. Since $\nu_+ \gg \nu_-$ and $\vec{F}_{\nabla B} \propto \omega$, resonantly excited ions experience a stronger force resulting in a shorter time of flight. A typical time-of-flight spectrum is shown in Fig. 2.27. The theoretical line shape is determined by the Fourier transformation of the excitation profile and follows the quadratic *sinc* function $\sin^2(x)/x^2$. Its line width is Fourier limited by the duration of the quadrupole excitation pulse T_q [KBK+95]

$$\Delta\nu(\mathrm{FWHM}) \approx \frac{k}{T_\mathrm{q}}, \tag{2.30}$$

where the constant k is close to 1. To improve the precision of the acquired cyclotron frequency, different excitation pulse shapes can be used. By the implementation of Ramsey's method of time-separated oscillatory fields [Ram90], the continuous excitation pulse is split into two shorter pulses with a defined waiting time in between. The amplitude of the field is adjusted such that a full conversion from magnetron to cyclotron motion still takes place for $\nu_\mathrm{q}=\nu_+ + \nu_-$. By using this excitation scheme,

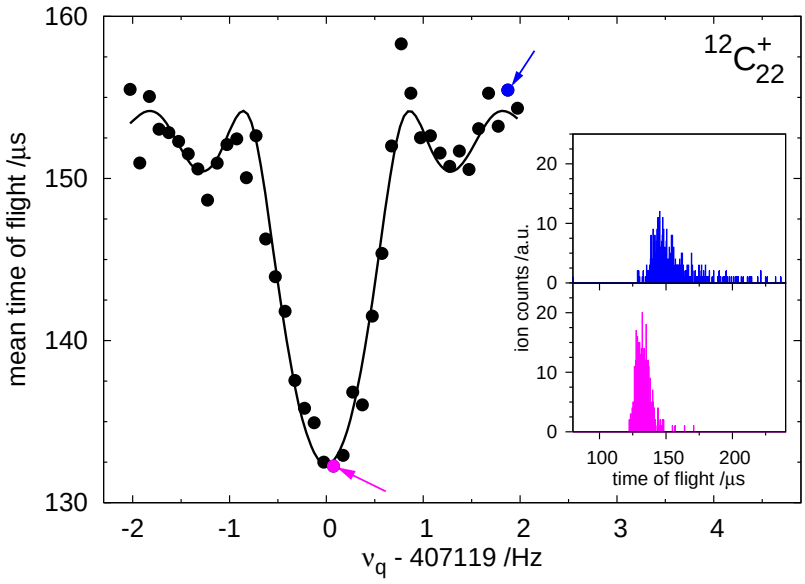

Figure 2.27: Time-of-flight spectrum for the cyclotron resonances of $^{12}C^+_{22}$, recorded during $\vec{B}$-field calibration at TRIGA-TRAP. The inset shows the time-of-flight spectra for off- (blue) and on-resonant (purple) excitation frequencies ν_q.

the statistical precision can be improved by a factor of three compared to the continuous excitation [GBH+07, EBB+11].
The TOF-ICR technique strongly relies on the validity of Eq. (2.18). Strictly spoken, this is only the case for an ideal Penning trap (without, e.g., field imperfections or trap misalignment). However, calibration measurements and error-budget assessment can minimize systematic errors for mass measurements [KBB+10, Smo12, Eib13]. The TOF-ICR technique is a destructive detection technique, as the ion of interest is lost upon arrival at the detector. It is therefore necessary that the supply of ions is sufficient to generate the required number of measurements N for the statistical precision aim which is proportional to $1/\sqrt{N}$.

Advanced ICR detection techniques for PTMS

The determination of the cyclotron frequency can also be performed in other ways. As an example, the detection of image charges in the segmented ring electrodes caused by the circulating charge is a non-destructive measurement technique. The full frequency spectrum can be analyzed without the need to reload the trap for each step assuming a long enough storage time. This reduces the time and the number of ions required to record a resonance tremendously. However, the life time of the ion has to be sufficiently long. The image charge is detected on two opposing ring electrode segments, as shown in Fig. 2.28. It can be recorded with a spectrum analyzer, however, the magnitude of the image charge is extremely low (in the order

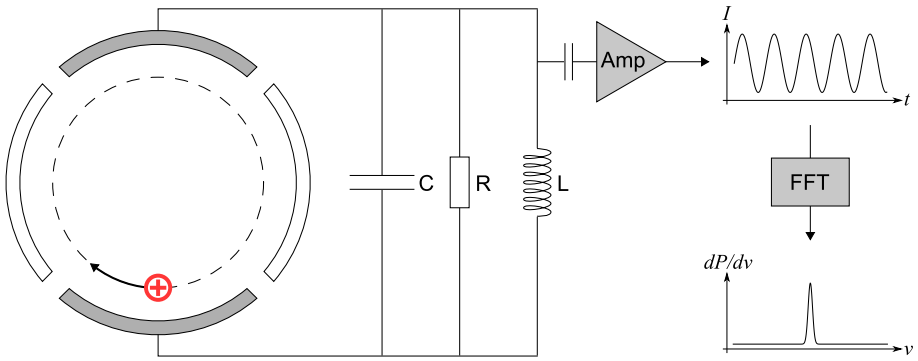

Figure 2.28: Principle of the FT-ICR measurement technique. The tank circuit can be cooled to the temperature of liquid He to reduce thermal noise.

of 10^{-15} A), and noise makes a direct signal tap impossible. In order to improve the signal-to-noise ratio, a tank circuit that is tuned to the revolution frequency of the ion ($\sim\nu_c$) is attached to the ring electrode segments, acting as a band pass filter. The signal is then capacitively coupled to a low-noise amplifier stage that can be cooled to cryogenic temperatures for the reduction of thermal noise. The resulting signal is Fourier-transformed to reveal the revolution frequency of the ion, giving the technique the name *Fourier-transform ion-cyclotron resonance* FT-ICR. This technique relies on possibly high radii of the ion orbit to increase the image charge, which requires a large volume of high field homogeneity (a hyperbolic trap geometry is in principle favored). FT-ICR will also be implemented at TRIGA-TRAP, first tests are reported in the thesis of Eibach [Eib13].
Another amazing method is the *phase-imaging ion-cyclotron-resonance* detection PI-ICR. The idea is to project the phase of the radial ion motion in the trap onto a position-sensitive detector [EBC+09], illustrated in Fig. 2.29. In the precision trap,

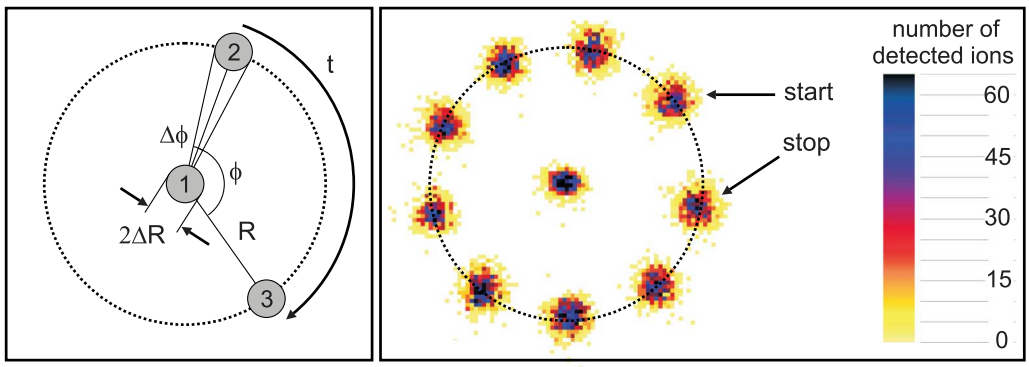

Figure 2.29: Left: Principle of the PI-ICR measurement technique. Right: Experimentally recorded signal on the position-sensitive detector of SHIPTRAP. Adapted from [EBB+13].

a phase-sensitive dipole excitation on ν_- is applied to bring the ions to a well-defined

magnetron radius. An immediate ejection would result in the detection of the ions on a certain spot on the detector (position (2) in Fig. 2.29). If the ejection is delayed by the time t, the phase Φ of the magnetron motion evolves freely in the trap and the ions will be detected on another spot (3). The total accumulated phase is then given by

$$\Phi + 2\pi n = 2\pi\nu_- t, \tag{2.31}$$

where n denotes the number of full revolutions that the ion undergoes during the time t. The measurement of Φ on the detector yields the magnetron frequency by solving Eq. (2.31) for ν_-. In the same way ν_+ can be determined, with the only difference that the initial dipole excitation is performed with frequency ν_+ and a quadrupole excitation on $\nu_+ + \nu_-$ converts the cyclotron into magnetron motion prior to ejection (without this step, the detector image would be smeared due to the substantially higher revolution frequency ν_+ and the required time to switch the upper endcap for ion ejection). The free cyclotron frequency (and thus the mass of the ions) is then determined via $\nu_c = \nu_+ + \nu_-$, as before. The use of this technique provides a 40-fold increase in the resolving power and a factor of four gain in precision [EBB+13], or a measurement time reduction of an order of magnitude compared to the Ramsey method.

2.3.3 Electrostatic deceleration stage

In order to capture an ion bunch created by the RFQ cooler and buncher in the purification trap, it has to be decelerated from the transport energy of 30 keV to a few tens of eV, which is the feasible voltage range for the axial DC potentials in the purification trap. There are two possible approaches for the deceleration: either the whole Penning-trap setup (including the superconducting magnet and the subsequent detection systems) is biased to 30 kV, or the ion bunch is decelerated in an electrostatic deceleration stage. For TRIGA-TRAP, the second approach is followed. A 3D model of the deceleration stage is shown in Fig. 2.20, the principle is illustrated in Fig. 2.30. Such deceleration stages are also utilized at other Penning-trap experiments, e.g., at ISOLTRAP [HDK+01]. The bunch enters the cylindrical electrode structure from the left with 30 keV. Almost the same voltage (28.9 kV) is applied to the long electrode of the deceleration stage, thus the bunch is decelerated from 30 keV to 1.1 keV. In this step, the transverse emittance, which is inversely proportional to the forward momentum p_{z0} (Eq. (1.3)), increases by a factor of $\sqrt{E_{\mathrm{high}}/E_{\mathrm{low}}}$ as $p \propto \sqrt{E}$. When the ion bunch has reached the center of the long electrode, the electrode's potential is switched from 28.9 kV to −1.1 kV (a high-voltage switch of type *Behlke HTS 301-03-GSM* switches the potential in less than 200 ns). Thereby, the potential energy of the ion bunch is reduced by

$$\Delta E_{\mathrm{pot}} = q(U_{\mathrm{high}} - U_{\mathrm{low}}) \tag{2.32}$$

so that it is not re-accelerated by leaving the electrode. The remaining transport optics towards the purification trap are biased at −1.1 kV and the trap itself is

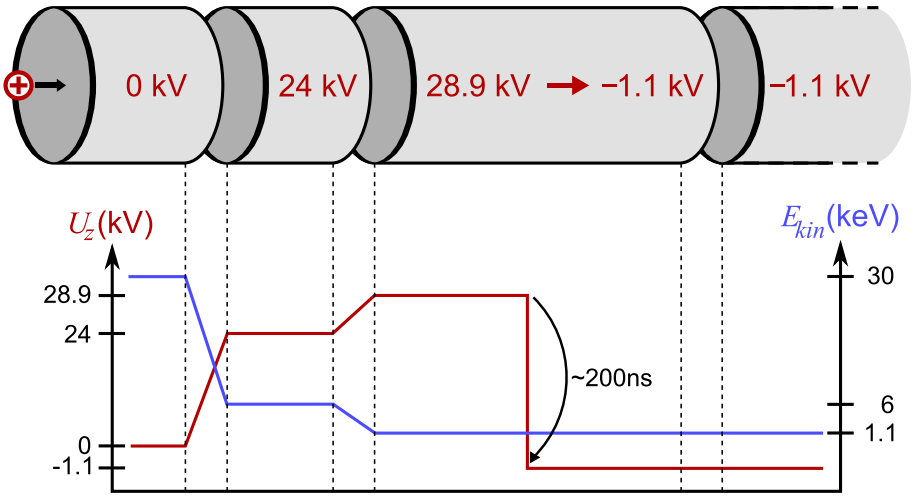

Figure 2.30: Principle of the TRIGA-TRAP electrostatic deceleration stage. The cylindrical electrodes are shown on the top of the figure, the ion bunch enters from the left. The applied voltages are plotted under their corresponding electrodes (red line). The resulting kinetic energy of the ion bunch is shown in blue.

operated at a few tens of Volts above ground potential.
The deceleration stage is described in the thesis of Smorra [Smo12], its commissioning has been done later, i.e., within this thesis. Therefore, an offline Cs^+ ion source is connected to the setup via the dipole magnet (see Fig. 2.1). The source is the subject of the diploma thesis of Nießen [Nie12]. A bunch of $^{133}Cs^+$-ions is accumulated in the RFQ cooler and buncher, and ejected towards the Penning-trap mass spectrometer (corresponding to the straight direction in the switchyard). A flight-time spectrum of a decelerated ion bunch is shown in Fig. 2.31. The flight time of the ion bunch is recorded from RFQ ejection to the moment of detection on an MCP detector in front of the purification trap. As stated before (Sec. 2.2.6), the signal of an MCP is not quantitative and its detection efficiency depends on the kinetic energies of incident particles. The graph shows a small peak around ∼28 µs and a large peak around ∼63 µs. The small peak is generated by ions that have failed the reduction of their potential energy. The large peak shows a considerably higher flight time and is caused by ions that successfully reduced their potential energy. The flight times for both peaks match the calculated ones with respect to their kinetic energies and travel distances.

2.3.4 Offline sources for mass measurements

TRIGA-TRAP is operational since 2008 [KKB+08], years before it was connected to the reactor. Since then, lots of successful mass measurements were completed, for which the ions were produced in offline ion sources [KAB+11, SBB+12, EBB+14]. The ion source mostly used is a laser ablation ion source, which was constructed by

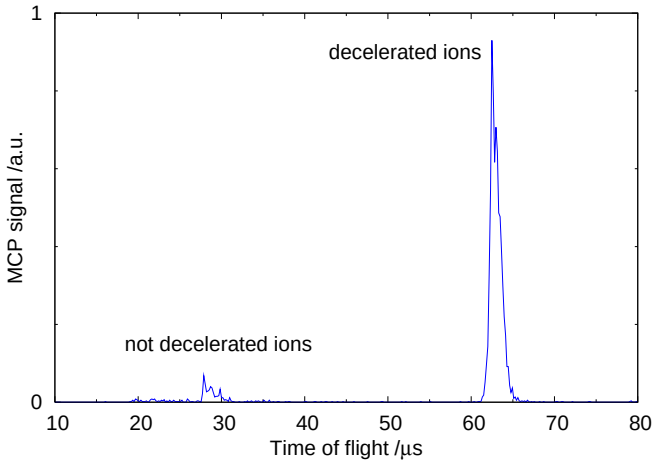

Figure 2.31: Flight-time spectrum of a $^{133}Cs^{+}$ bunch that is partially decelerated in the TRIGA-TRAP electrostatic deceleration stage. Non-decelerated ions are identified by their low flight time (around 28 µs).

Smorra [Smo08, Smo12] and recently upgraded with a miniature RFQ to boost its efficiency [Eib13]. Most of the direct mass measurements performed at TRIGA-TRAP relate the measured cyclotron frequency to the current mass standard, ^{12}C, or cluster molecules $^{12}C_x$ ($2 \leq x \leq 22$) thereof, as demonstrated by Blaum *et al.* [BBH+02]. For future mass measurements, this method will most likely be continued. The preparation of carbon clusters in the offline source will be performed in parallel to the radioactive-nuclide production as the carbon clusters are not produced in the fission process.

2.4 The collinear laser-spectroscopy beam line TRIGA-LASER

2.4.1 Principles of collinear laser spectroscopy

The idea of laser spectroscopy is to probe properties of atoms and molecules through the interaction of their electronic shell with an applied laser field. Laser spectroscopy seems to be restricted to the examination of electronic states and therefore to the investigation of the atomic structure. However, also nuclear structure information can be extracted, as laser spectroscopy is sensitive to changes in the atomic properties that are induced by electron-nucleus interactions. An introduction to the topic including further references was given by Billowes and Campbell [BC95], and an extensive textbook on the topic is the one by Demtröder [Dem07]. *Collinear* laser spectroscopy is the application of laser spectroscopy to a moving particle ensemble with (anti-) collinear propagation vector. The successful application of collinear laser spectroscopy for more than three decades and its on-going developments are reviewed in, e.g., [CF10, BDN13].

The interaction of light and matter is most easily explained by Einstein's rate model. The interaction takes place if a particle (an atom, molecule, or ion) has a spatial overlap with a light field and the light field has an energy $h\nu$ matching one of the energy level differences of the particle. As depicted in Fig. 2.32, absorption

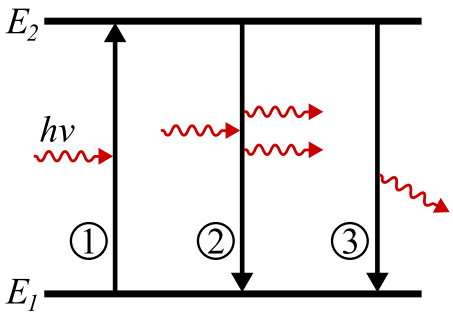

Figure 2.32: Simple atomic two-level scheme and its interaction with a laser field. Three types of processes can occur: absorption (1), induced emission (2), and spontaneous emission of a photon (3).

and induced emission can occur if

$$h\nu = E_2 - E_1, \tag{2.33}$$

where E_2 and E_1 are the energies of the excited electronic level and the ground state, respectively, in a simple two-level scheme. The probability of these two processes depends on the spectral energy density of the radiation field, while the probability of spontaneous emission does not depend on external fields but on the electronic structure of the particle. The probability is called Einstein coefficient of spontaneous

emission and is inversely proportional to the life time of the excited state

$$\tau_2 = \frac{1}{A_{21}}. \tag{2.34}$$

The spontaneous emission process is also referred to as fluorescence, and the life time induces a non-zero natural line width of the corresponding transition

$$\delta\nu_\mathrm{n} = \frac{1}{2\pi\tau_2}. \tag{2.35}$$

The intensity distribution is given by a Lorentz profile, as depicted in Fig. 2.33 (left). While the natural line width is typically very small, experimenters have to handle various additional broadening mechanisms, the most dominant being the *Doppler broadening*. A Doppler profile is depicted in Fig. 2.33 (right). It arises from the velocity vector of the particle under investigation w.r.t. the light source or detector used. Thereby, a particle moving with velocity $\vec{v}$ experiences the light field ν_L Doppler-shifted

$$\nu = \nu_\mathrm{L} + \frac{\vec{k}_\mathrm{L}}{2\pi}\vec{v}, \tag{2.36}$$

where $\vec{k}_\mathrm{L}$ denotes the wave vector of the light field. When a spectroscopic line is recorded in an experiment, the resulting profile is typically a convolution of a Lorentz and a Doppler profile, called Voigt profile. Depending on the fit routine, the Lorentz and Gauss line widths can be extracted separately. Due to the velocity-dependent Doppler line width, the laser-spectroscopic (Voigt) line width of atomic gases at room temperature can easily be a factor of 100 higher than the natural line width. Yet, one of the major challenges of laser spectroscopic experiments is the

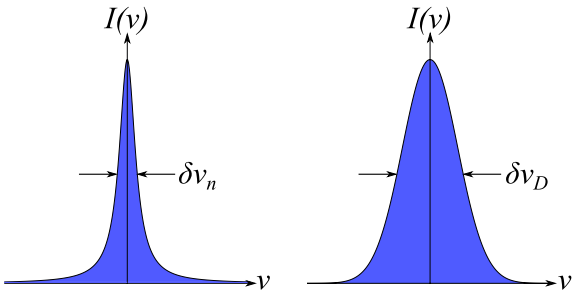

Figure 2.33: Intensity distributions for the absorption and emission of light. Left: Lorentz profile, $\delta\nu_\mathrm{n}$ is typically in the order of tens of MHz. Right: Gauss profile, $\delta\nu_\mathrm{D}$ is typically in the order of a few GHz. A convolution of the two yields the Voigt profile.

precision of the frequency determination of the spectroscopic lines. Therefore, apart from a general need to raise the signal-to-noise ratio of detectors, the experiments

implement techniques to reduce the effects of broadened spectroscopic lines (two-photon excitation, velocity bunching, etc.).
Laser spectroscopy can probe nuclear properties by the determination of shifts in the frequency of an electronic transition of different isotopes of mass A and A'. The total isotope shift includes the nuclear mass shift (MS) and the nuclear field shift (FS) [NG14]:

$$\delta\nu_{\mathrm{IS}}^{AA'} = \delta\nu_{\mathrm{MS}}^{AA'} + \delta\nu_{\mathrm{FS}}^{AA'}. \tag{2.37}$$

Figure 2.34 illustrates the two effects. The mass shift is caused by the different center-of-mass (com) motions for nuclei having different mass. Thus, when a neutron is added to the nucleus, the com of nucleus and electron is shifted towards the nucleus. This changes the kinetic energy of the com motion, and when an electron is excited into a higher-lying state, this energy change has to be compensated by the absorbed photon. The mass shift is divided into the normal mass shift (NMS) and

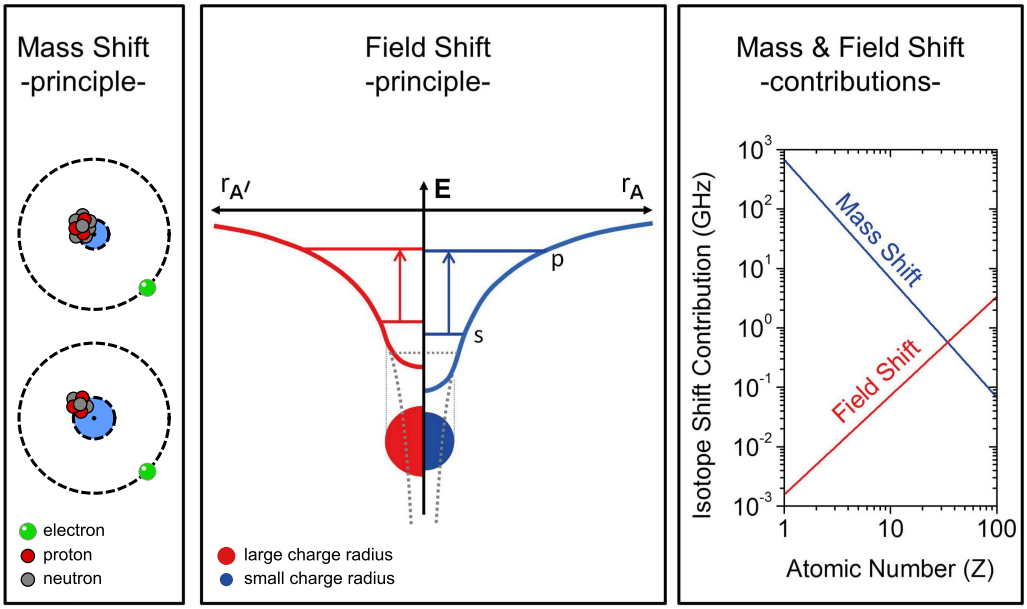

Figure 2.34: Left: principle of the mass shift. Top left: large mass ⇒ smaller com motion, bottom left: small mass ⇒ larger com motion. Mid: Principle of the nuclear mass shift and the nuclear field shift, adapted from [NG14]. Right: Their contributions to the total isotope shift.

the specific mass shift (SMS). The NMS arises from the change in each electron's momentum and can be evaluated with relative ease. The SMS, however, is caused by a change in the electron correlation terms, which cannot be solved analytically. It can be solved only numerically and is already a challenge for a two-electron system [NG14]. The field shift (or volume shift) is caused by the different nuclear charge radii of isotopes. The pure $1/r$ Coulomb potential that confines the electron in the case of a point-like nucleus (dotted gray line) is perturbed for non-zero nuclear

charge radii (red and blue lines). The different shape of the potential implies changes in the energy level structure of the electron.
Both effects contribute to the total isotope shift, but with different ratios depending on the atomic number Z. The general trend is illustrated in Fig. 2.34 on the right. The field shift contribution to the total isotope shift can be written as [NSE+11]

$$\delta\nu_{\mathrm{FS}}^{AA'} = F\delta\left\langle r_{\mathrm{c}}^2\right\rangle^{AA'}, \tag{2.38}$$

where F denotes the field-shift constant and $\langle r_{\mathrm{c}}^2\rangle$ the mean squared nuclear-charge radius. By the determination of F and $\delta\nu_{\mathrm{MS}}^{AA'}$, the nuclear charge radius can be calculated by use of the so-called *King plot* analysis [Kin63, BC95].
Laser spectroscopy can also resolve the hyperfine structure (HFS) of atomic transitions. For nuclei having non-vanishing spin $\vec{I}$, the precise energy of the atomic state depends on the coupling of the nuclear magnetic moment μ_I to the magnetic dipole moment B_J and electric quadrupole moment Q_s of the electron. This leads to a hyperfine multiplet of levels for each atomic state, as shown exemplary in Fig. 2.35 for $^{43}Ca^+$. The energy levels are labeled by the total angular momentum quantum

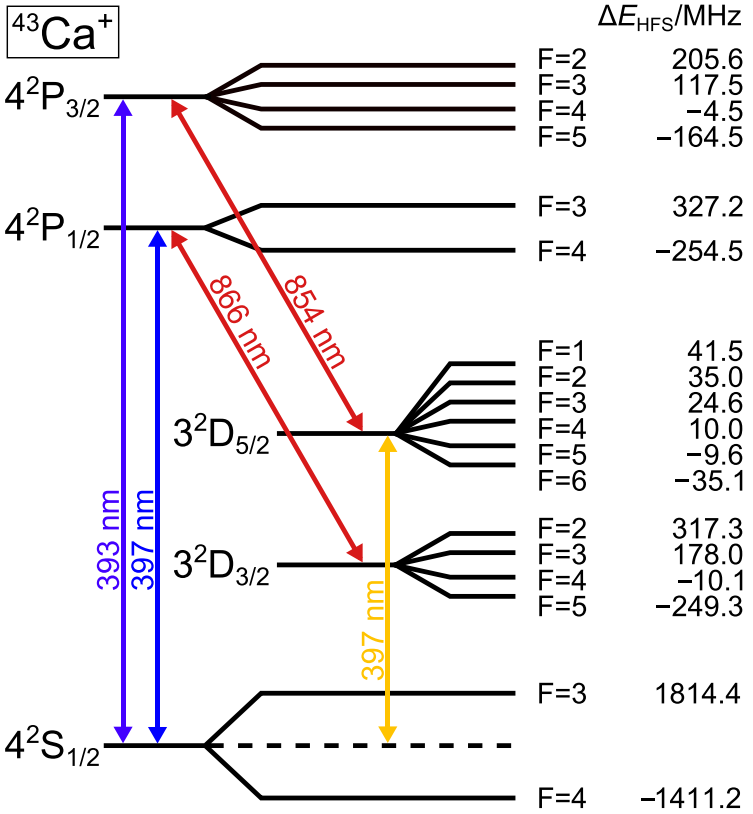

Figure 2.35: Hyperfine levels of the ionic stable odd isotope of calcium, $^{43}Ca^+$. The energy deviations for the hyperfine levels are taken from [BKR+07].

number

$$\vec{F} = \vec{I} + \vec{J}, \tag{2.39}$$

where $\vec{J}$ denotes the total angular momentum of the electron (spin & orbit). The hyperfine splitting of the unperturbed level is given by the Casimir formula [Kop58]

$$\Delta E_{\mathrm{HFS}} = \Delta E_{\mathrm{md}} + \Delta E_{\mathrm{eq}}, \tag{2.40}$$

$$= A\frac{C}{2} + B\frac{\frac{3}{4}C(C+1) - I(I+1)J(J+1)}{2(2I-1)(2J-1)IJ}, \tag{2.41}$$

where ΔE_{md} and ΔE_{eq} are the contributions from the magnetic dipole and electric quadrupole moment, respectively, and

$$C = F(F+1) - I(I+1) - J(J+1) \tag{2.42}$$

is the Casimir factor, for first-order interaction. The hyperfine A and B factors

$$A = \frac{\mu_I B_J}{IJ}, \quad B = eQ_s V_{JJ}, \tag{2.43}$$

are experimentally defined and represent the magnetic dipole and electric quadrupole constant, respectively. Once A and B have been measured for one isotope with static known moments, the moments of other isotopes can be calculated by simple ratios, while a few corrections have to be considered [BC95]. The nuclear spin can usually be determined from the number positions, and intensities of the HFS components. The electric quadrupole moment Q_s is used to investigate the deformation of nuclei (see Fig. 2.36).

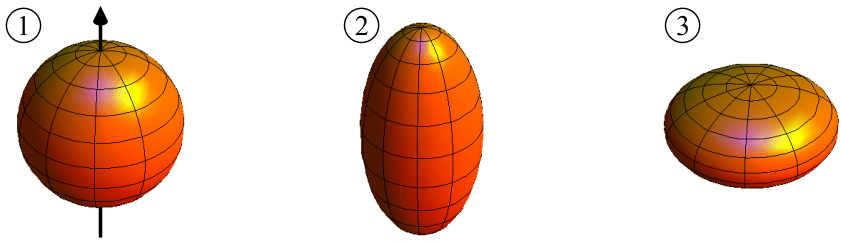

Figure 2.36: The nuclear spin (1) and the deformation of nuclei can be determined by the examination of the hyperfine structure levels. Oblate deformation (2) corresponds to a negative electric quadrupole moment Q_s, and prolate deformation (3) to a positive Q_s.

2.4.2 The TRIGA-LASER beam line

At the collinear laser spectroscopy beam line TRIGA-LASER, the nuclear ground state properties discussed above (spins, moments, and charge radii) of stable and short-lived nuclei will be determined [KKB+08]. To apply this versatile technique, a narrow bandwidth laser beam is collinearly superimposed with an ion beam extracted either from an offline ion source directly adapted to the 10° chamber (Fig. 2.1) or from the online ion source. Fluorescence spectra are obtained by applying a post-acceleration voltage to the optical detection unit (ODU) to tune the Doppler-shifted laser frequency into resonance [Kau76].

The setup of TRIGA-LASER is presented in detail in the thesis of Krämer [Krä10], thus only a minimal introduction will be given. The principle of laser spectroscopy is depicted in Fig. 2.37 and described in the caption therein. However, one aspect of

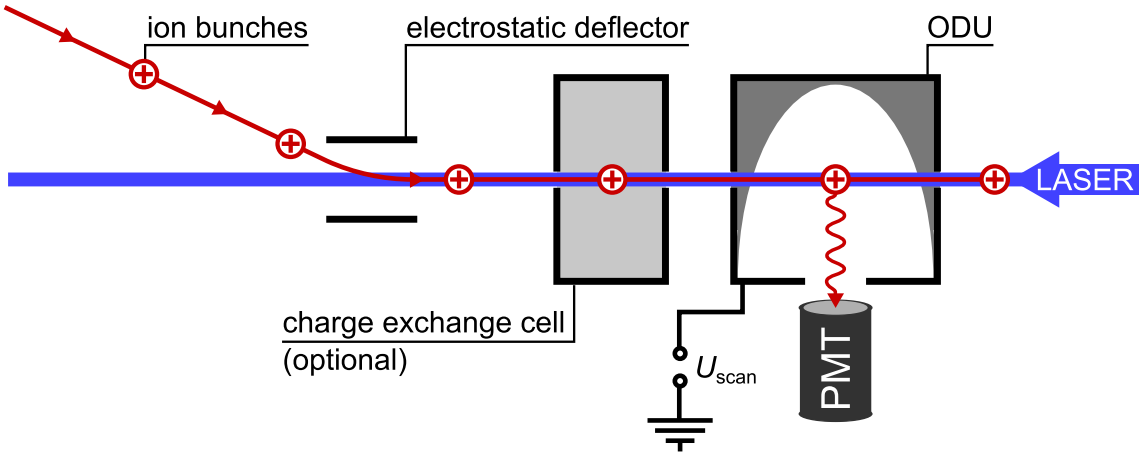

Figure 2.37: Principle of laser spectroscopy. The superposition of the ion bunch and the anti-collinear laser beam is provided by proper deflection of the ion bunch. The ions can be neutralized in the charge exchange cell, if necessary. The ions are then Doppler-shifted into resonance with the laser light by the scan voltage U_{scan}. In the case of atoms, this step happens prior to neutralization. For ions, the resonance condition can be spatially restricted to the optical detection unit (ODU) to avoid optical pumping. An ellipsoidal mirror geometry for high fluorescence-photon visibility is combined with a compound parabolic concentrator for the reduction of stray light. The fluorescence is recorded by a photomultiplier tube (PMT).

laser spectroscopy is presented: the *velocity bunching effect* counteracting Doppler broadening. The width of spectroscopic lines has to be minimal for high-precision measurements and the dominant fraction of the line broadening is caused by the Doppler effect

$$\Delta\nu_{\text{D}} = \nu_0 \frac{\delta v}{c}, \tag{2.44}$$

where δv denotes the velocity uncertainty in an ion ensemble at temperature T and ν_0 the transition frequency in the rest frame[5]. When the particles are electrostatically accelerated by a potential U_{acc}, the energy uncertainty δE stays constant, as depicted in Fig. 2.38. The differential variation of energy with velocity v can be written as

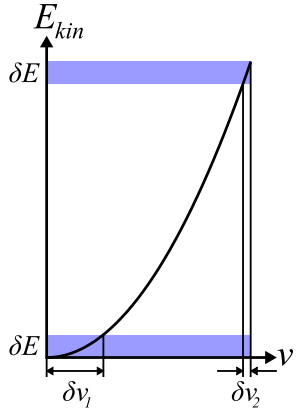

Figure 2.38: Velocity bunching: the energy uncertainty δE is constant under electrostatic acceleration, reducing the velocity uncertainty δv.

$dE{=}mv{\cdot}dv$, thus $\delta E{=}\delta(mv^2/2){=}mv\delta v$. Because $\delta E{=}$const, any increase in velocity must be compensated by a corresponding reduction of δv [BDN13]

$$\delta v = \frac{\delta E}{mv} = \frac{\delta E}{\sqrt{2mqU_{\mathrm{acc}}}}. \tag{2.45}$$

Inserting Eq. (2.45) into Eq. (2.44) yields

$$\Delta\nu_{\mathrm{D}} = \nu_0 \frac{\delta E}{\sqrt{2qU_{\mathrm{acc}}mc^2}}. \tag{2.46}$$

Hence, the Doppler width is reduced by a factor of $1/\sqrt{U_{\mathrm{acc}}}$, which is a factor of more than 100 in the case of TRIGA-SPEC ($U_{\mathrm{acc}}{=}U_{\mathrm{HV}}{=}30\,\mathrm{kV}$), and gets close to the natural line width.

The bottleneck of optical measurements based on the conventional laser-induced fluorescence detection using photomultiplier tubes is the large background caused by scattered laser light along the beam line. One way to enhance the sensitivity by several orders of magnitude is an ion-photon coincidence detection [EWS+86, KBB+12]. However, this requires an almost isobarically pure ion beam, which is rarely available at a radioactive-ion-beam facility. RFQ cooler and bunchers are ideal tools to reduce this background. Typical accumulation times t_{acc} are on the order of a few to a few tens of ms, and the temporal width of the bunch Δt is a few µs or less. Once the bunch is released from the RFQ, it appears at the ODU at

[5]Especially in the case of surface-ionization, the Gaussian velocity distribution of a particle ensemble can be quite broad as $v_{\mathrm{therm}} = \sqrt{2k_{\mathrm{B}}T/m}$.

a well-defined time with a well-defined width. By restricting the photon detection to this time interval, the laser-induced background can be suppressed by a factor $\zeta = t_{\mathrm{acc}}/\Delta t \approx 10^5$ [NCB+02, Nör10], as shown in Fig. 2.39. The optimal parameters

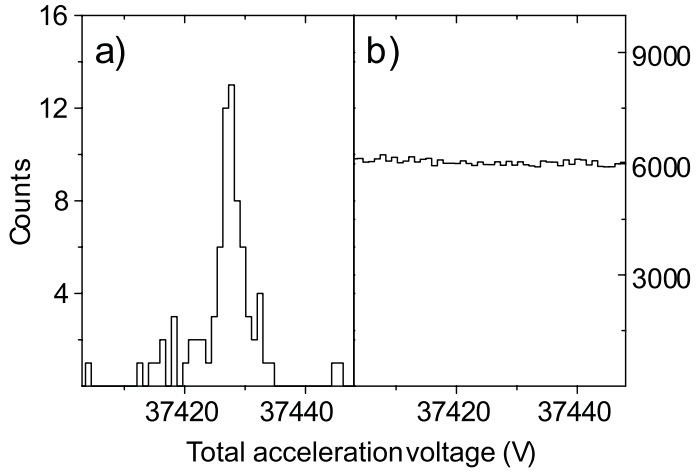

Figure 2.39: Resonance fluorescence spectra for ^{174}Hf a) gated on the ion bunch, and b) ungated. Through bunching of the ions, the signal-to-noise ratio is increased so that the resonance becomes distinguishable from the background. Taken from [NCB+02].

for each ion species depend on several factors such as the half-life of the nuclide of interest, the survival time of ions in the RFQ, and space-charge effects, etc..

2.4.3 Fluorescence-light detection techniques at TRIGA-LASER

There are two distinct ways for the detection of ion bunches by fluorescence light detection. The most precise approach is the one discussed above. However, it requires a laser at the corresponding wavelength to be absorbed by the ions in the bunch. A much simpler method to analyze the temporal structure of the released ion bunches is the residual-gas afterglow method. For this purpose, the pressure in the ODU is increased by switching off the turbo-molecular pumps and stabilized at about $5 \cdot 10^{-5}$ mbar. The higher pressure increases the probability of the ions to collide with residual gas atoms inside the ODU. The residual gas atoms are excited in an inelastic collision and subsequently de-excited by emitting fluorescence photons, which are detected by the photomultiplier (PMT). The PMT signal is recorded with a multi-channel scaler triggered by the bunch ejection. Obviously, this method cannot be used to investigate the energy spread ΔE of the bunch, nor can laser spectroscopy at all be performed. Still, as the method does not require a laser beam and can therefore be set up quickly, it is a feasible way for the commissioning of the RFQ cooler and buncher and to optimize its operation parameters w.r.t. the temporal structure of bunches and their relative intensities.

3 Commissioning of the ion beam preparation transfer line

3.1 Characterization of the dipole magnet

Important parameters for the operation of a separator magnet besides its bending angle are the maximum magnetic field strength, the reproducibility of the magnetic field and its stability. The reproducibility is affected by the remanence, or hysteresis, of the magnet. The separator magnet of TRIGA-SPEC was tested with a Hall probe during the ramp down of the supply current, from the maximum (specified) magnetic field strength of 1.1 T down to 0 T, see Fig. 3.1. The slope in the beginning

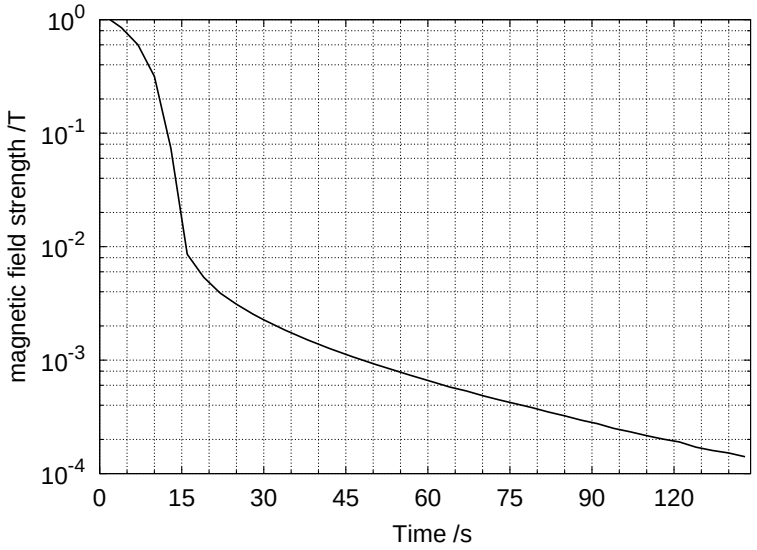

Figure 3.1: Magnetic-field discharge curve of the separator magnet through the ramp down from 1.1 T to 0 T. For details, see the text.

reflects the ramp-down speed of the supply current. The exponential decay starting around t=15 s (consider the logarithmic scale), however, reflects the slowly decaying magnetic field (the 1/e time constant is $\tau \approx 14$ s for the last 5 mT). The absolute value of the magnetic field strength was not measured, but it is assumed that the magnet will reach 0 T after the supply current has been switched off (and sufficient time has passed). For good reproducibility, it is wise to reach for the aimed magnetic field strength always from the same direction (e.g., from a lower value up to the aimed one of $\vec{B}$).

The experiments typically focus on one specific nuclide during a measurement campaign, so the magnetic field will remain unchanged for that time. Of great interest is therefore the stability of the magnetic field, as large deviations could perturb the ion trajectories in the separator magnet and reduce the injection efficiency $\eta_{\text{injection}}$ of the ion beam into the RFQ cooler and buncher. The stability was recorded over several hours of operation for a comparably high magnetic field strength $\vec{B}_0$=0.882 T. The histogram data was fitted with a Gauss profile. The standard deviation is

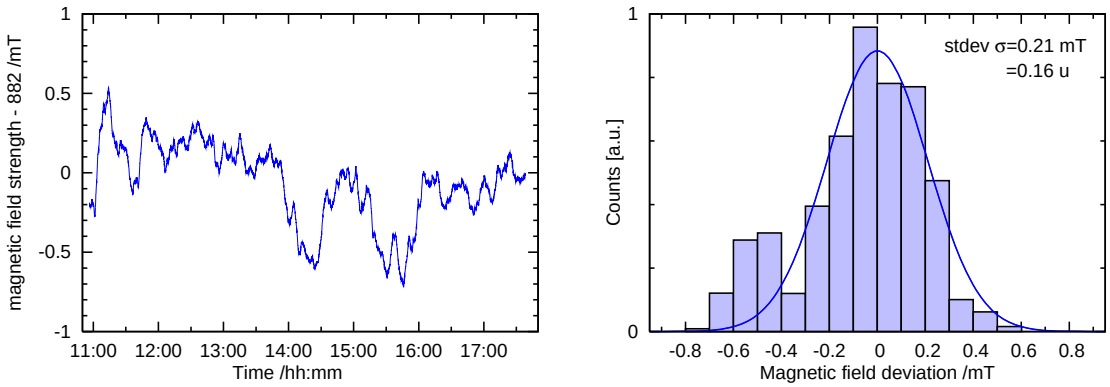

Figure 3.2: Stability of the magnetic field of the separator magnet over approximately 6 h at a relatively high magnetic field strength of 0.882 T (m/q=335 u/e). Left: B-field measured by a Hall probe as a function of time. Right: Histogram of the data points including a Gauss fit (solid line).

σ=0.21 mT, leading to a relative error of the magnetic field of $\Delta\vec{B}/\vec{B}\approx 2.4\cdot 10^{-4}$. The largest influence on $\vec{B}$ results from temperature changes of the coils. The coils are actively cooled by a cooling circuit, the cooling water temperature is regulated to roughly ±2.5°. This cooling-water as well as air temperature changes (the air temperature is also regulated) can cause changes of the magnetic field as shown in Fig. 3.3. The magnetic field strength of 562 mT corresponds to a mass-over-charge ratio of ∼136 u/e according to Eq. (2.6), representing the nuclides of the heavy fission branch. The standard deviation of the Gauss fit can be expressed in atomic mass units to 0.07 u as displayed in the figure, the relative error of the magnetic field stays the same. An improvement of the cooling-water temperature stability, which is controlled by the reactor staff, should increase the stability of the magnetic field strength tremendously. An additional error contribution arises from the current stability of the magnet power supply (Danfysik MPS 853[1]), which is specified to $1\cdot 10^{-5}$.

The mass resolving power of the magnet was investigated with the predecessor of the surface ionization ion source, an ECR ion source, which produced plasma-ionized xenon from residual air or the oxygen supply bottle for the plasma burning

[1] http://www.danfysik.com/853

inside the vacuum. As $B \propto \sqrt{m}$, heavier ions are increasingly difficult to distinguish in the mass spectrum of a dipole magnet. The masses of the Xe isotopes belong to the heavy fission branch of TRIGA-SPEC (Fig. 2.4), making them good candidates to answer the question if the mass resolving power is sufficient for TRIGA-SPEC. Figure 3.4 shows a mass spectrum of Xe which was recorded on the Faraday cup behind the RFQ cooler and buncher. The ion-optical elements are adjusted such that the exit focal point of the double-focusing magnet is located at the entrance of the RFQ. The peaks of $^{131}Xe^{+}$ and $^{132}Xe^{+}$ can be distinguished easily, and given the FWHM of the Gauss fit[2], the mass resolving power $R{=}m/\Delta m$ results to $R{=}244$. It is therefore possible to separate nuclides from the heavy branch as required by the experiments.
The commissioning of the RFQ cooler and buncher was performed mostly with isotopes of K and Ca, which were produced in the surface-ionization ion source by the introduction of the KCl carrier molecules. The spectrum of emitted ions contains abundant amounts of K^{+}, but also Ca^{+} due to low purity, as it is shown in Fig. 3.5.

[2]The Full Width at Half Maximum (FWHM) of the Gauss distribution is given by $2\sqrt{2\ln 2}\sigma$, where σ is the standard deviation.

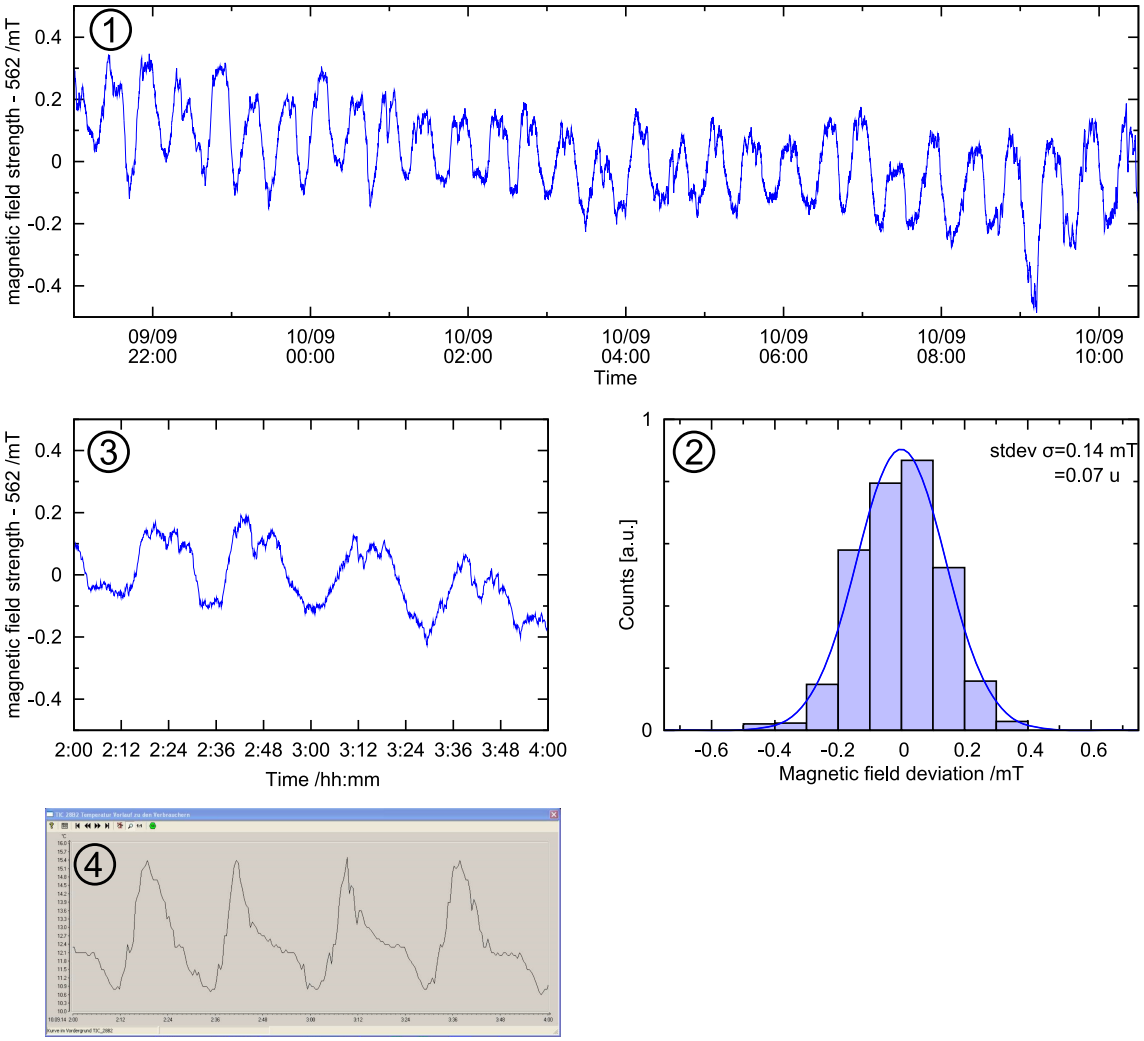

Figure 3.3: Stability of the magnetic field of the separator magnet over approximately 12 h at a magnetic field strength of 562 mT. (1): B-field measured by a Hall probe as a function of time. (2): Histogram of the data points including a Gauss fit (solid line). (3): magnification of (1) for the night time from 2–4 a.m.. (4): temperature of the cooling water for the magnet coils, at exactly the same time. It deviates between 10.6 and 15.4°C.

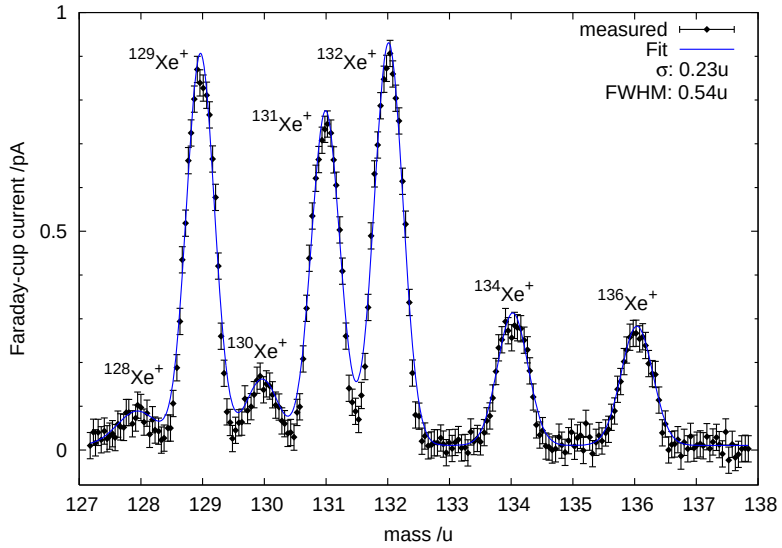

Figure 3.4: Mass spectrum of Xe with natural abundance, recorded on a Faraday cup behind the RFQ cooler and buncher. The sum of Gauss functions fitted to each peak and the mean widths of the three highest peaks are shown. The error bars originate from the specified precision of the measurement device (Keithley 6487 Picoammeter).

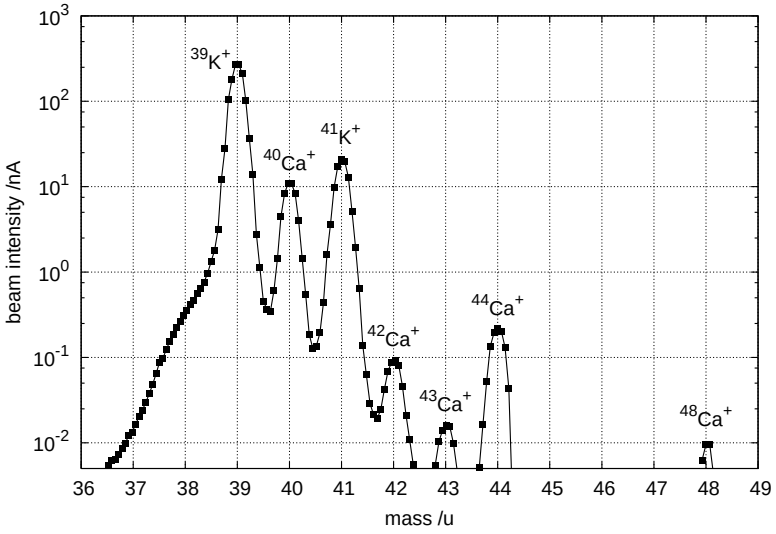

Figure 3.5: Mass spectrum of K^+ and Ca^+ with natural abundance, recorded on a Faraday cup behind the separator magnet. $^{46}Ca^+$ could not be detected on the Faraday cup due to its low natural abundance (0.004%).

3.2 Performance of the ion beam diagnostics

The detector units utilized at TRIGA-SPEC offer the possibility to measure a number of beam parameters, as discussed in Sec. 2.2.6. Ion current measurements using the Faraday cup are presented above. The beam profile is analyzed with the phosphor screen at the back plate of the MCP. As an example, the mass spectrum of Fig. 3.5 can also be observed on the phosphor screen, as shown in Fig. 3.6. The ion

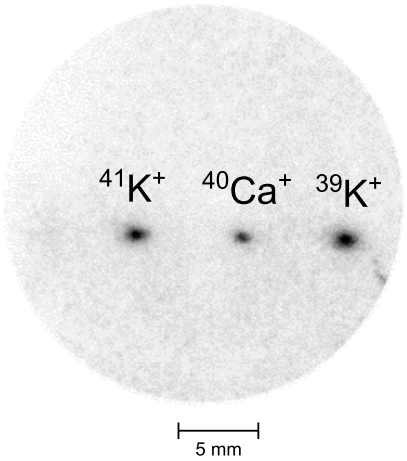

Figure 3.6: Screen capture of the phosphor screen, taken with a CCD camera, behind the mass separator. The spots correspond to the masses A=39–41, the active area on the phosphor screen is a circle with diameter d=25 mm.

beam is focused to a spot size of ∼1 mm by the dipole magnet and the preceding ion optics. When the ion beam is optimized for the injection into the RFQ cooler and buncher, the focal point has to be shifted along the beam propagation axis to the RFQ entrance. The phosphor screen also shows demonstrative pictures of the cooling of a continuous ion beam that takes place inside the RFQ (see Sec. 3.3).
One important property of an ion bunch is the number of ions it contains. A tool to analyze this property is provided by a Faraday cup equipped with a charge amplifier and additional detection electronics. The ion bunch created in the RFQ from an incident ion beam should carry the number of unit charges

$$Q_{\mathrm{bunch}} = \eta_{\mathrm{bunching}} \frac{I_{\mathrm{cooled}} t_{\mathrm{acc}}}{e}, \tag{3.1}$$

where I_{cooled} is the cooled ion beam leaving the RFQ in continuous mode, t_{acc} the accumulation time of ions in the RFQ, and e the elementary charge. The bunching efficiency η_{bunching} is the unitless ratio of ions leaving the RFQ as a bunch and the corresponding fraction of the cooled continuous beam. In order to generate reliable ion numbers, the charge amplifier has to be calibrated independently from

the bunches. This is done with a frequency generator and a subsequent resistor, as depicted in Fig. 3.7. The frequency generator creates a custom voltage signal of amplitude U_{FG} and temporal width t_{width}, similar to a bunch of charges after passing a resistor R. The artificially created bunch carries the number of unit charges

$$Q_{\mathrm{FG}} = \frac{U_{\mathrm{FG}} t_{\mathrm{width}}}{eR}. \tag{3.2}$$

The charge amplifier (Stahl Electronics PR-E3-SMA[3]) amplifies and converts the signal into the one shown in Fig. 3.7, yielding the amplitude U_{out} that is dependent on the number of incident charges. By reading the value of U_{out} on, e.g., an oscilloscope, the number of ions in the bunch can be determined by

$$Q_{\mathrm{bunch}} = k_{\mathrm{amp}} \cdot U_{\mathrm{out}}. \tag{3.3}$$

Incidentally, U_{out} of the PR-E3-SMA is capped at 1.38 V, or $\sim 2{\cdot}10^6$ ions. A calibration with artificial bunches yielded the proportionality factor k_{amp}=1.51(8)$\cdot 10^3$/mV.

[3]http://www.stahl-electronics.com/

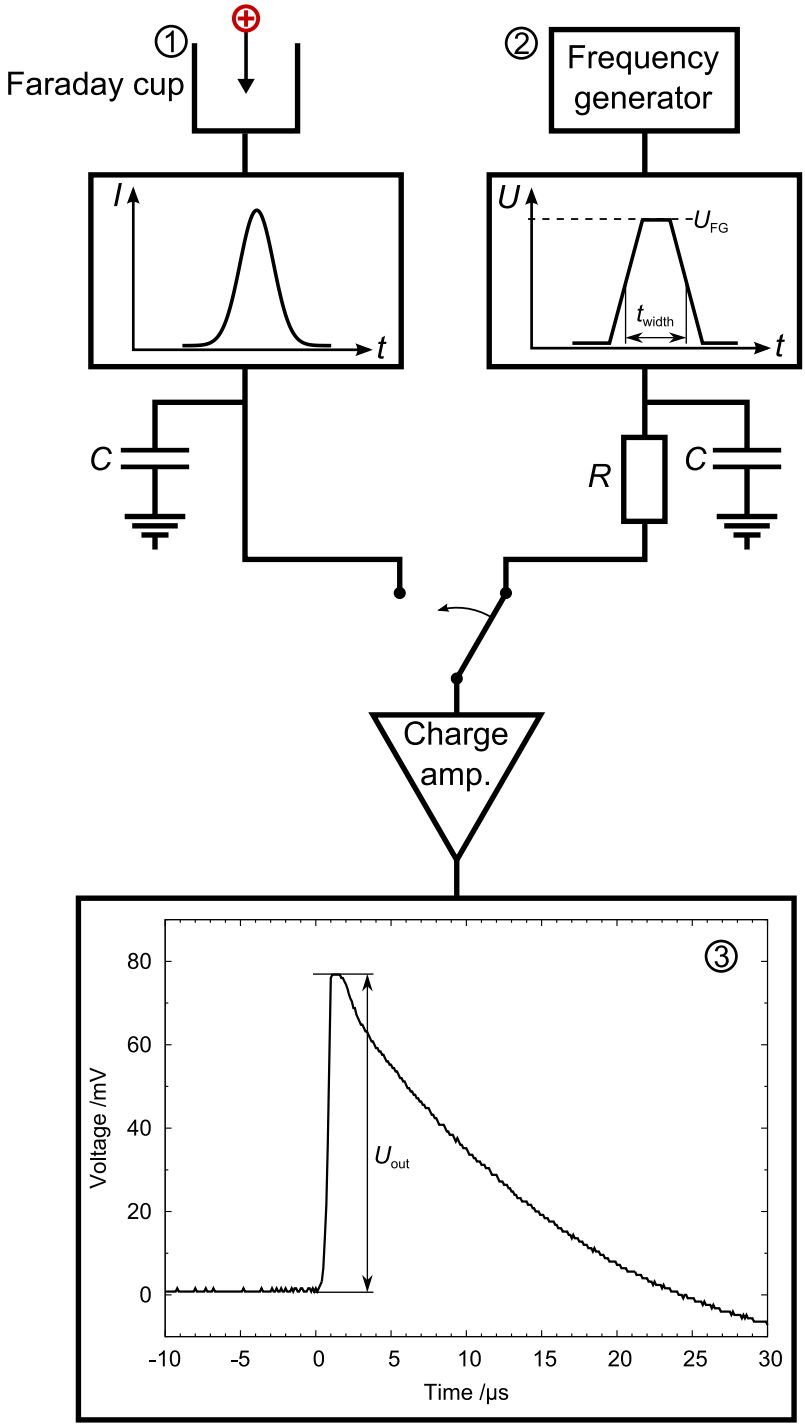

Figure 3.7: (1): signal created by ion bunches impinging on the Faraday cup. (2): creation of artificial bunches used to calibrate the charge amplifier. (3): signal response of the charge amplifier (the signal shape is identical in both cases).

3.3 Characterization of the RFQ cooler and buncher

3.3.1 Cooling of a continuous ion beam

In continuous mode (i.e., no bunching), the cooling of the ion beam can be impressively demonstrated by changing the buffer gas pressure. Two phosphor-screen captures from the phosphor screen behind the RFQ are shown in Fig. 3.8 corresponding to insufficient (left) and optimum (right) cooling, respectively. If no buffer

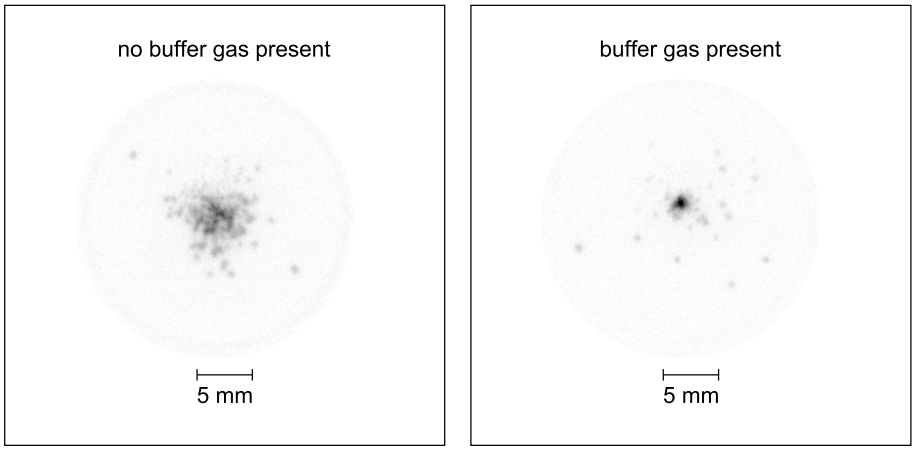

Figure 3.8: Screen captures of the phosphor screen that is attached to the MCP behind the RFQ cooler and buncher (inverted colors). Left: uncooled ion beam, i.e., with a too low buffer-gas pressure. Right: cooled ion beam.

gas is introduced into the structure, the ion motion is not damped. The applied radio frequency confines the ions, but leaves them on trajectories with great extent from the symmetry axis. A fraction of the ions is also lost as the ions having too high motional amplitudes will strike the electrodes. Consequently, the ion beam creates a large spot on the phosphor screen. Once the buffer-gas density in the RFQ is increased, the radial ion motion is gradually damped and the spot diameter consequently reduced. The optimum value for the buffer-gas density is created by a buffer-gas flow rate of 0.18 mbar·l/s, at the point where the beam diameter is minimal. A further increase of the buffer-gas density results in a reduced beam transmission due to a collisional blocking of the beam, showing a degrading spot intensity and an increasing beam diameter on the phosphor screen.
The ion beam current can be measured on Faraday cups in front of (I_0) and behind (I_{cooled}) the RFQ, yielding the transmission

$$T_{\mathrm{RFQ}} = \frac{I_{\mathrm{cooled}}}{I_0}. \tag{3.4}$$

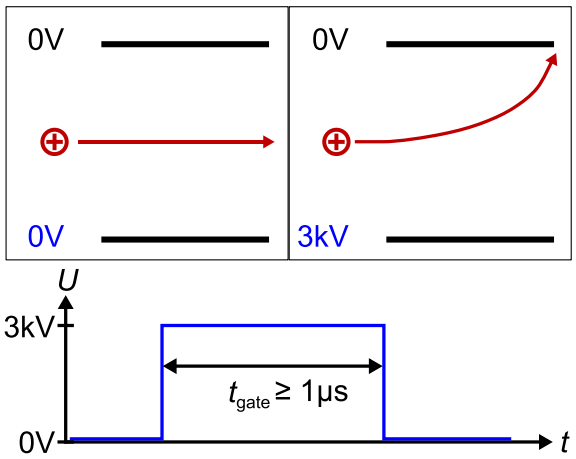

Figure 3.9: Principle of a simple beam gate. By applying a sufficiently high offset voltage to one of the ion optical elements, the beam leaves the optimized trajectory and gets lost.

However, both positions require separate settings of the ion optical elements, as the focal point of the dipole magnet has to be shifted along the propagation axis to fully strike the Faraday cup. For the ion-optical elements presently implemented in the beam line, the transmission of an ion beam created in the surface ionization ion source and cooled in the RFQ was found to be $T_{\mathrm{RFQ}} \approx 25\%$ (tested with K).

3.3.2 Parameters for the bunching mode

For the commissioning of the bunching mode, it is necessary to control the number of ions that enter the RFQ. This can be done by adjusting the intensity I_0 of the continuous ion beam created in the ion source and the time window t_{acc} for beam injection into the RFQ. The latter is not only able to limit the number of injected ions, but can also stop the introduction of ions into the RFQ completely, e.g., during the cooling time. The time window can be accomplished by gating a sufficiently high deflection voltage on one of the preceding electrostatic deflectors, as illustrated in Fig. 3.9. Thus, the number of injected ions is

$$Q_{\mathrm{in}} = \eta_{\mathrm{injection}} \frac{I_0 t_{\mathrm{acc}}}{e}, \tag{3.5}$$

where $\eta_{\mathrm{injection}}$ denotes the injection efficiency into the buncher, which depends strongly on the beam properties (i.e., transverse emittances $\varepsilon_{x,y}$, focal point, etc.). The transmission T_{RFQ} discussed above is proportional to $\eta_{\mathrm{injection}}$, but it differs by the transport efficiency of successfully injected ions along the RFQ structure $\eta_{\mathrm{transport}}$:

$$T_{\mathrm{RFQ}} = \eta_{\mathrm{injection}} \eta_{\mathrm{transport}}. \tag{3.6}$$

The procedure of ion bunch generation is shown schematically in Fig. 3.10. The ac-

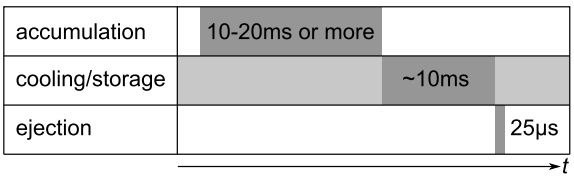

Figure 3.10: Relevant time parameters for the creation of bunches. The bar lengths are not to scale.

cumulation time t_{acc} is controlled to accumulate the experimentally desired number of ions, depending on the specific production rate of the ion. The upper limit is in principle given by the loss rate of ions inside the RFQ, or the required bunch ejection frequency. As discussed in Sec. 3.3.4, the storage half life of ions in the TRIGA-SPEC RFQ is in the order of tens of seconds. The cooling time t_{cool} depends on the ion and buffer-gas species, and is typically in the order of a few tens of ms. Strictly speaking, the cooling does not *start* after the accumulation, as the buffer gas is permanently introduced. Rather, the start of t_{cool} is defined as the minimum cooling time for the last ion that was injected during t_{acc}. The time window for ejection just has to be sufficiently long to empty the RFQ.

3.3.3 Temporal width of ion bunches

The temporal width Δt of ion bunches was investigated first with the residual gas afterglow method as described in Sec. 2.4.3 with $^{39}K^{+}$ ions produced in the surface-ionization ion source. A characteristic ion bunch signal is shown in Fig. 3.11. For $^{39}K^{+}$, the RF parameters were set to V_{RF}=85 V and ν_{RF}=1.0 MHz, leading to a pseudo-potential well depth of D=9 V (Eq. (1.32)). The DC potential well depth along the RFQ axis was set to U_{DC}=10 V and the capture electrode to $U_{15\mathrm{hi}}$=35 V. A Gauss fit yields the temporal width of the bunch, but the absolute number of ions per bunch cannot be determined owing to the measurement method. The photomultiplier signal was taken in the ODU, which is about 6 m upstream from the RFQ exit, or approximately 18 µs in flight time. The Full Width at Half Maximum (FWHM) is in the case of Fig. 3.11 ∼223 ns, and depends on several parameters as shown in the following.

Figure 3.12 shows the dependence of the bunch width on the number of ions in the bunch. For small ion numbers up to a certain value, the width is almost constant. A substantial increase is observed for ion numbers $>10^6$. For even higher ion numbers, the signal smeared out and lost its Gaussian shape. This is a sign that the ions trapped in the RFQ's potential well reach the space-charge limit (see Sec. 1.3.6).

The influence of the kicking electrode's voltage on the bunch width and the number of ejected ions is shown in Fig. 3.13. The number of *injected* ions Q_{in} is kept constant, the ejection voltage was set to $U_{15\mathrm{lo}}$=−250 V. Increasing the kicking voltage $U_{13\mathrm{hi}}$ has the effect of reducing the bunch width, as the electric field gradient gets even steeper during ejection. However, a decreasing trend is observed in the number of

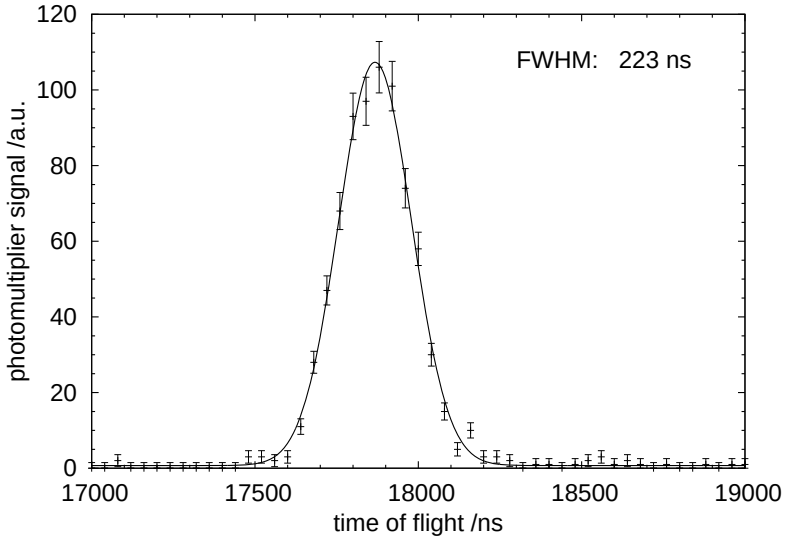

Figure 3.11: Averaged photomultiplier signal of 5000 ion bunches, recorded with the residual gas afterglow method. The line represents a Gaussian fitted to the experimental data. The flight time to the detector is approximately 18 µs.

ions per bunch. This can be due to the fact that ion numbers were very high during the measurement, thus the ensemble was not completely trapped in a small volume above the second-to-last electrode. If the volume of the ensemble extends to or exceeds the kicking electrode, part of the ions are cut off from the ejected bunch, an effect that gets stronger for higher kicking voltages.

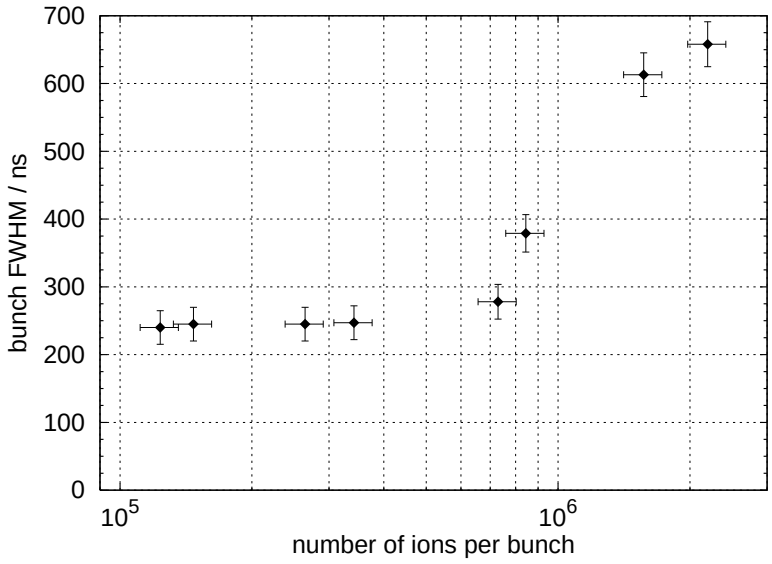

Figure 3.12: FWHM of $^{39}K^+$ bunches as a function of the overall number of accumulated ions in the RFQ Q_{in}, controlled by t_{acc}.

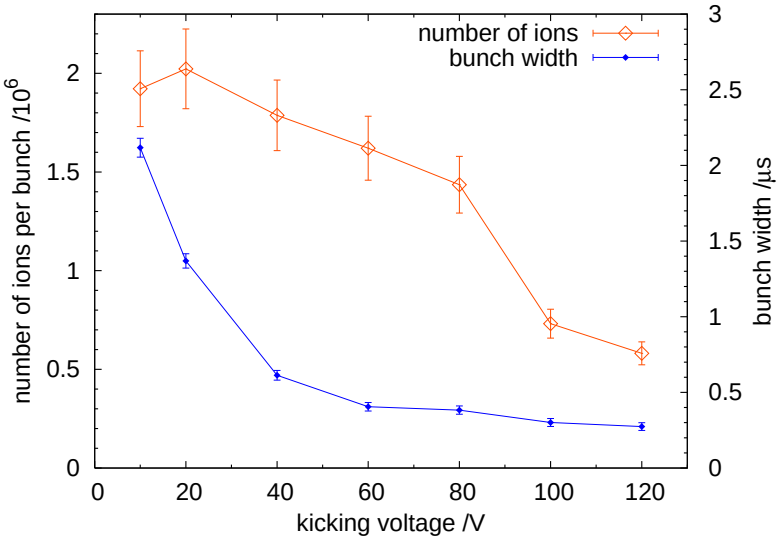

Figure 3.13: Bunch FWHM and number of ejected $^{39}K^+$ ions as a function of the kicking voltage $U_{13\mathrm{hi}}$ at an ejection voltage of $U_{15\mathrm{lo}}$=−250 V. All other parameters were kept constant.

Parameter	**Symbol**	**Value**
radio frequency	ν_{RF}	1.0 MHz
RF amplitude	V_{RF}	100 V
axial well depth	U_{DC}	6–10 V
capture voltage	U_{15hi}	25 V
buffer-gas pressure	p_{RFQ}	$\sim 4.6 \cdot 10^{-3}$ mbar
accumulation time	t_{acc}	0.1–100 ms
cooling time	t_{cool}	10–20 ms
ejection frequency	f_{eject}	40 Hz
ejection voltage	U_{15lo}	40 V
kicking voltage	U_{13hi}	40 V

Table 3.1: Standard parameters for the operation of the TRIGA-SPEC RFQ in bunching mode. During commissioning, these parameters were optimized.

One of the most important parameters for RFQ operation is the buffer-gas density. The density is controlled by the buffer-gas flow rate into the tube containing the rods, as depicted in Fig. 2.12. The following commissioning tests were performed with $^{40}Ca^{+}$. The RFQ parameters were set to the values listed in Tab. 3.1 unless otherwise stated. The number of ions injected into the RFQ was kept well below the space-charge limit to avoid any influence, at around 5–20 thousand ions (which is about two orders of magnitude less than the limit derived from Fig. 3.12). The values for U_{15lo} and U_{13hi} are set to create a *symmetric* $\vec{E}$-field gradient during ejection which is centered at the second-to-last electrode, where the ions are accumulated. Thereby, the energy spread ΔE is much smaller at the cost of a slightly larger temporal width, which is preferred by the experiments. Figure 3.14 shows the dependence of the ejected bunch intensity (i.e., number of ejected ions) on the buffer-gas flow rate. If the flow rate is too little, the motion of the injected ions is not sufficiently damped in the RFQ and a large fraction gets lost. For a flow rate of 0.135 mbar·l/s, the cooling mechanism starts to work and the ions are accumulated. After reaching the optimum value at 0.14 mbar·l/s, the bunch intensity decreases with higher flow rates. This is due to an increased collision rate of the ions during the cooling process (possible loss mechanisms were discussed in Sec. 1.2), and to a worse overall pressure behind the RFQ exit that decreases the beam transmission after ejection. Notably, the optimum value for the buffer-gas flow rate in the bunched mode differs from the optimum value in continuous mode (0.14 mbar·l/s vs. 0.18 mbar·l/s). This is easily understood as the ions are cooled for a much shorter time ($\sim$75 µs) in continuous mode where they pass the buffer-gas region only once.

The effect of the cooling time t_{cool} on the temporal width of the bunch (10%-width, i.e., the width of the bunch at 10% of its maximum height) and the bunching efficiency was investigated, shown in Fig. 3.15. Once the buffer-gas flow is fixed, the damping of the ion motion only depends on the time the ions spend inside the buffer-

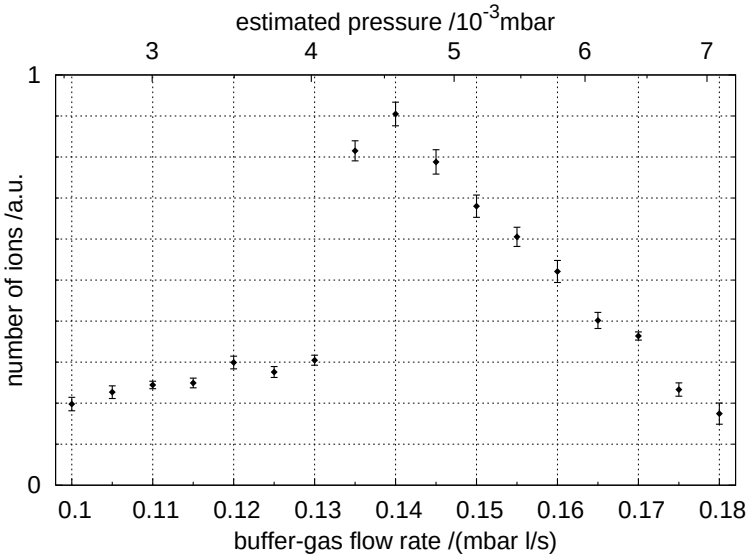

Figure 3.14: Intensity of $^{40}Ca^{+}$ bunches at different buffer-gas flow rates with a cooling time of t_{cool}=10 ms.

gas filled RFQ. It can be observed from the graph that a minimum cooling time of $\sim$1 ms is required. For shorter cooling times, the ion motion does not seem to be damped (larger bunch width) and ions are not efficiently trapped or get lost during ejection (smaller ion numbers), resulting in a lower bunching efficiency. For more than 1 ms, the values still get slightly better. As a compromise between ejection frequency and sufficient cooling, the value was set to 10 ms for further measurements.

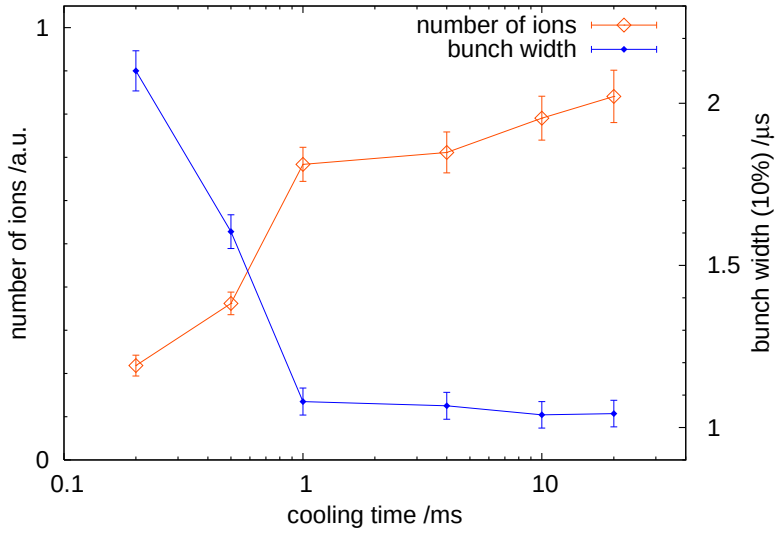

Figure 3.15: Bunch width (10%-width) and number of ejected ions as a function of the cooling time t_{cool}. The number of injected ions Q_{in} is constant. The buffer-gas flow was set to 0.14 mbar l/s, in agreement with Tab. 3.1.

3.3.4 Measurement of the energy spread and longitudinal emittance

A low energy spread ΔE of the emitted ion bunches is of utmost importance for laser-spectroscopic measurements, but is also beneficial for the Penning-trap mass spectrometer as it enables more efficient beam transport and Penning-trap injection. The commissioning data presented in the following shows that there are parameters which decrease the energy spread along with other properties (like temporal width) or are independent thereof, and other parameters that require a trade-off between different properties.
The measurements were performed by time-resolved laser spectroscopy, as described in Fig. 2.37, with an anti-collinear cw laser beam of ∼130 µW power. For the excitation of $^{40}Ca^{+}$, the $4^2S_{1/2}$–$4^2P_{1/2}$ transition was used, the energy diagram is shown in Fig. 3.16. The fluorescence detection is on the same wavelength as the excitation

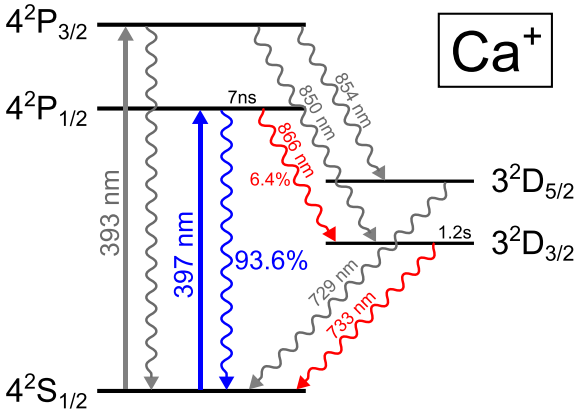

Figure 3.16: Part of the energy diagram of Ca^{+}. The transition used for laser spectroscopy is $4^2S_{1/2}$–$4^2P_{1/2}$, the excitation laser and the fluorescence light are in the visible blue. The spontaneous emission to the $3^2D_{3/2}$ level and back to the ground state (infrared) are not recorded by the PMT due to an optical filter.

laser, the infrared wavelengths are filtered out. The data acquisition consists of a stable voltage source that controls U_{scan}, and a multi-channel scaler (MCA) to record the fluorescence photons and to sort them into time bins of 20 ns. The voltage U_{scan} manipulates the kinetic energy of the ion bunches, and scans the electric transition in steps of 1 V. As $\Delta E_{\mathrm{kin}}{=}{-}q\Delta U$ (with $q{=}{+}1e$), the voltage scan directly translates into a scan of the (longitudinal) kinetic energy. A Voigt profile is then fitted to the resonance, the FWHM and its error can be extracted from the fit [LCS05]. A more detailed description of the data acquisition at TRIGA-LASER can be found in [Kau13].
An instructive example for the trade-off between temporal width Δt and energy spread ΔE is the slope of the electric field gradient used during the ejection of the ion bunch from the RFQ. The field gradient is generated by the last three electrodes

as described before. For a symmetric field gradient, the last electrode is set to $U_{15\mathrm{lo}}{=}{-}x\,\mathrm{V_{DC}}$, the second-to-last electrode to $0\,\mathrm{V_{DC}}$, and the third-to-last electrode to $U_{13\mathrm{hi}}{=}{+}x\,\mathrm{V_{DC}}$ (the AC parts are not changed for ejection). Figure 3.17 shows the influence of the kicking voltage to the temporal width and energy spread of the ejected ion bunch. By the application of stronger field gradients, the bunch is ejected

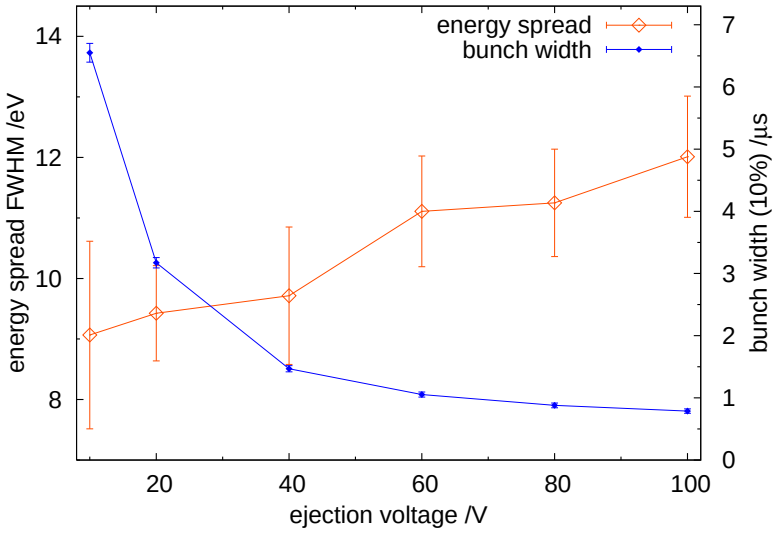

Figure 3.17: Longitudinal energy spread (FWHM) and bunch width (10%) as functions of the DC electric field gradient during ejection, represented by the voltage $U_{15\mathrm{lo}}{=}{-}U_{13\mathrm{hi}}$. As an example, the corresponding electric field gradient for $U_{15\mathrm{lo}}{=}{-}40\,\mathrm{V}$ is $\sim$18.3 V/cm.

faster, resulting in a lower temporal width. However, the energy spread grows at the same time. Due to the geometrical extent of the ion ensemble, individual ions are located at different positions on the slope of the electric field. This results in different kinetic energies during ejection, increasing the total energy spread. To keep the energy spread below 10 eV while maintaining a reasonable temporal width of the ion bunch, the symmetric ejection voltages were set to $U_{13\mathrm{hi}}{=}{-}U_{15\mathrm{lo}}{=}40\,\mathrm{V}$.
A possibility to reduce the energy spread of an ion bunch is to remove the "hottest" ions from it. These are the ions with the largest motional amplitude that leave the RFQ, they are consequently located at the edge of the bunch. By the insertion of an aperture, the radially outermost ions can be cut away from the bunch. However, the anti-collinear laser probes the longitudinal (z-axis) energy spread. The ions with highest longitudinal energy deviation will not be cut away as long as their transverse kinetic energy is sufficiently low. Figure 3.18 shows the result of the measurement. As expected, the energy spread reduction is not significant. The number of ions, however, decreases rapidly for an aperture of 1 mm, indicating that the geometrical beam diameter is larger.

By the measurement of the temporal width and the energy spread of the bunch simultaneously, the longitudinal emittance ε_z (as defined in Sec. 1.1) can be calcu-

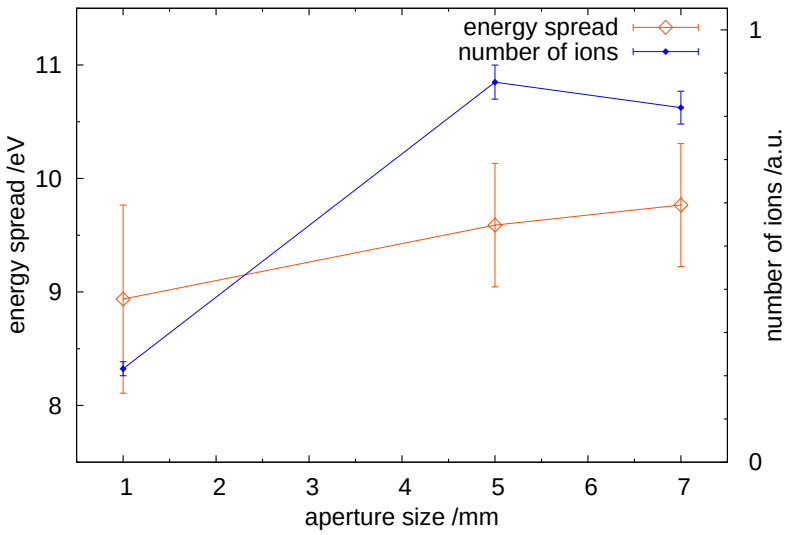

Figure 3.18: Longitudinal energy spread (FWHM) and number of ions in dependence on the inner diameter of an aperture located in front of the ODU.

lated and action diagrams like the ones in Fig. 1.3 can be plotted. In the case of a longitudinal focus at the position of the detector, the longitudinal emittance can be calculated according to Eq. (1.6). The position of the longitudinal (or time) focus can be controlled by the Einzel lens at the RFQ ejection (see Fig. 2.12). The voltages were set such that the focus was positioned at the location of the ODU by optimizing them for smallest bunch width Δt. The bunch can then be visualized in a density plot as shown in Fig. 3.19. Comparing the plot to the ones in Fig. 1.3 with respect to the symmetry of the time axis, it can be seen that the bunch is in the longitudinal focus. It can thus be fitted in both dimensions separately, with a Gauss profile in the time axis and a Voigt profile in the energy axis. Visualizing the two functions in the same type of plot yields Fig. 3.20. The area of the ellipse was defined earlier (see Fig. 1.2), the ellipse axes are given by $\Delta E/2$ and $\Delta t/2$ in the case of a longitudinal focus. For example, the longitudinal emittances for the ellipses marked in Fig. 3.20 are $\varepsilon_{z,\mathrm{FWHM}}$=3.52(53) eVµs and $\varepsilon_{z,10\%}$=13.76(2.06) eVµs. The behavior of the emittance plot can be reviewed for certain parameter changes that were already discussed above. For example, it can be seen that for different cooling times the ions that add to the ejected bunch intensity through a longer cooling time do not increase the bunch's emittance (Fig. 3.21). However, the emittance plots change their shape once the number of incident ions Q_{in} is altered. The relation between number of ions and temporal width of the bunches was already presented in Fig. 3.12, recorded with the residual gas afterglow technique. Through laser spectroscopy, emittance plots can be generated as shown in Fig. 3.22. It can be seen that the energy spread is significantly reduced for 25,000 ions compared to 500,000 ions (as well as the temporal width), again indicating that the ions are not efficiently trapped inside the DC potential well. However, there is no significant

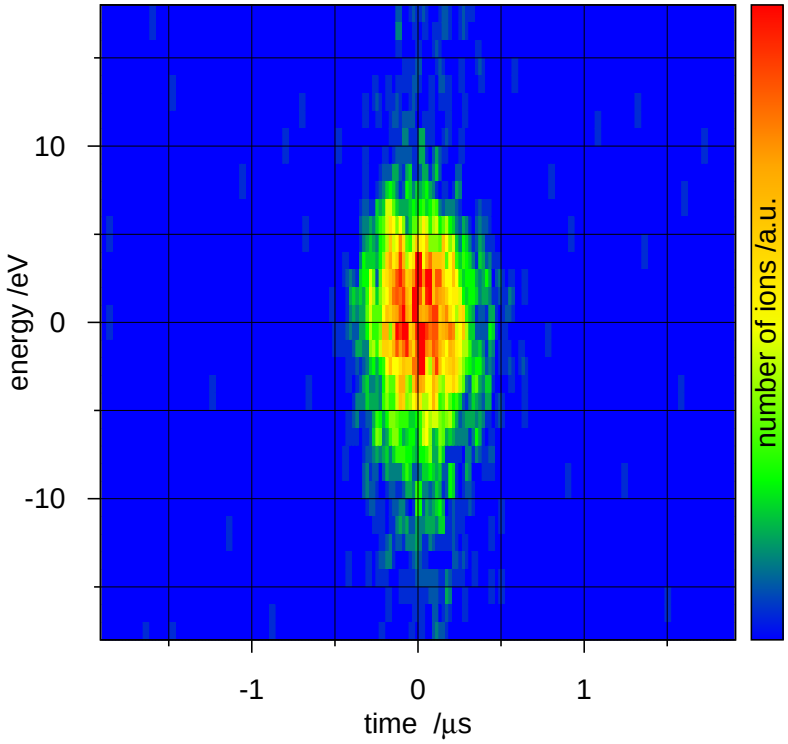

Figure 3.19: Density plot of an ion bunch created by the TRIGA-SPEC RFQ cooler and buncher. The energy and time deviations from the mean energy and time are shown, the color code represents the number of ions per bin. One bin is 1 eV high and 20 ns wide. Parameters are as listed in Tab. 3.1.

energy-spread reduction for another order of magnitude of less ions when comparing the plots for 25,000 and 1,500 ions.

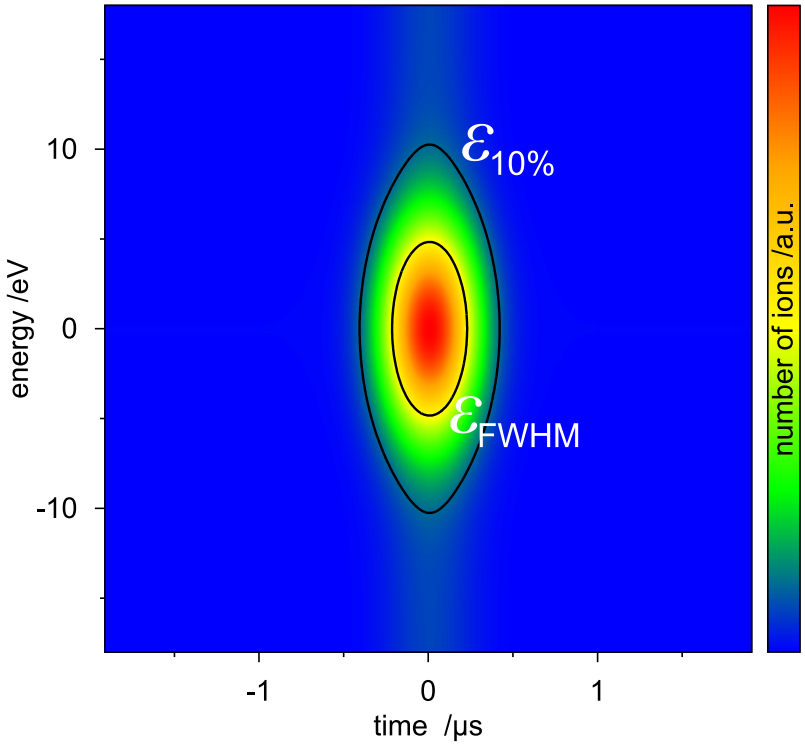

Figure 3.20: Density plot of the fitted ion bunch of Fig. 3.19. The contours that correspond to the full widths at half and 10% of the maximum are drawn, the resulting ellipses are denoted $\varepsilon_{z,\mathrm{FWHM}}$ and $\varepsilon_{z,10\%}$. See the text for details.

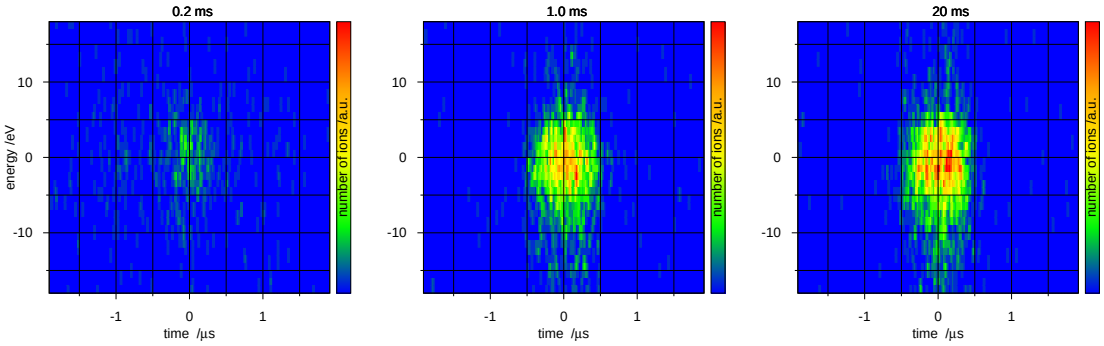

Figure 3.21: Ion bunch density plots for cooling times of t_{cool}=$\{0.2\,\mathrm{ms}, 1.0\,\mathrm{ms}, 20\,\mathrm{ms}\}$ at a constant number of incident ions. The scaling for the color-coded intensity is constant as well.

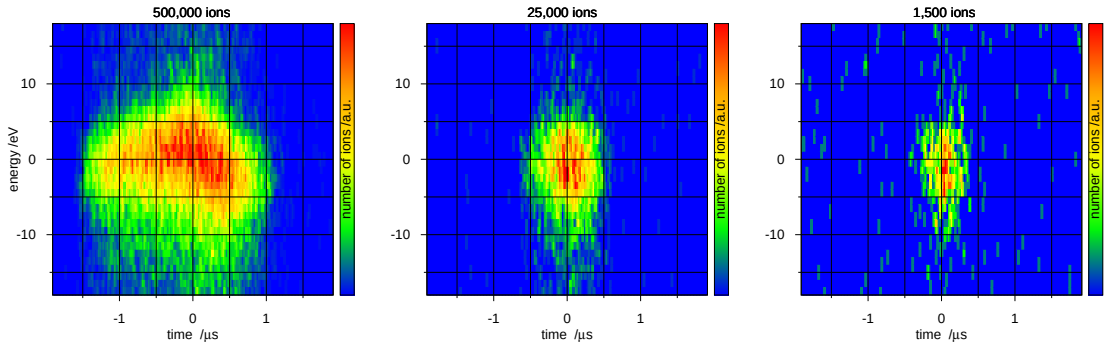

Figure 3.22: Ion bunch density plots for different numbers of ions injected into the RFQ cooler and buncher, controlled by t_{acc}. The color-coded intensity is rescaled for each plot.

Determination of the storage time for ion bunches

In an early measurement campaign with $^{133}Cs^{+}$ ions, the maximum storage time of ions in the RFQ was investigated. The ions were produced by the offline ion source attached to the separator magnet (see Fig. 2.1), and held inside the RFQ for times that are very long compared to typical cooling times. For $^{133}Cs^{+}$, the RF amplitude was set to V_{RF}=250 V at ν_{RF}=1.0 MHz. The number of ions was measured at that time by integrating over the electric voltage drop on one of the MCP plates. The proportionality of the MCP signal is only given for small incident ion numbers and a possibly large distribution of the ions on the MCP surface. It was verified with a beam gate, nevertheless, it cannot be fully guaranteed. Figure 3.23 shows the results. It is observed that storage times of more than 60 s can be achieved, and a storage

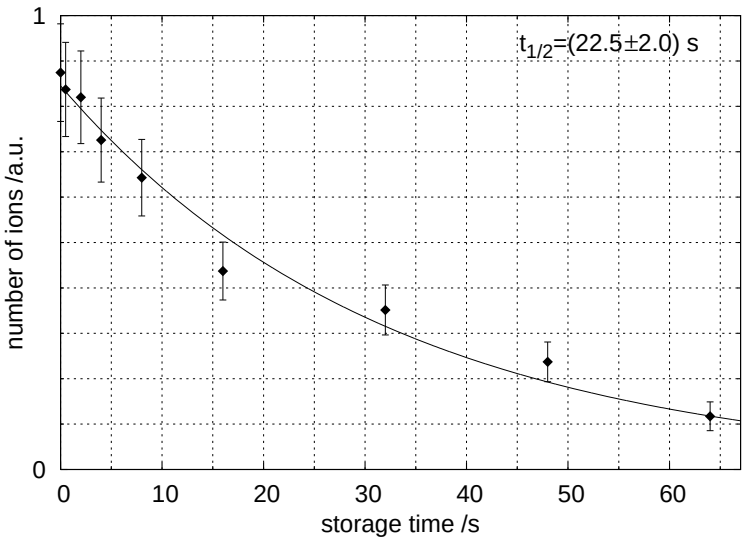

Figure 3.23: The number of ejected ions as a function of the storage, or cooling, time t_{cool} for $^{133}Cs^{+}$ ions inside the RFQ cooler and buncher. The solid line is an exponential fit to the data points. For details, see the text.

life time of $t_{\frac{1}{2}}$=22.5(2.0) s at a buffer-gas pressure of approximately $5{\cdot}10^{-3}$ mbar was determined. The main source for the loss of ions should be charge exchange due to the high number of collisions during long storage times. Though storage times on the scale of several tens of seconds are not at all demanded by the experiments, it is still an important fact for the operation of TRIGA-TRAP that accumulation times of a few seconds for scarcely produced nuclides are possible without major losses. The measurement cycle of TRIGA-TRAP is about 2 s with the TOF-ICR method, thus bunch ejection frequencies f_{eject} greater than 0.5 Hz are not needed.

3.3.5 Determination of the bunching efficiency

The bunching efficiency η_{bunching} as defined in Eq. (3.1) denotes the ratio of ejected ions in bunching and continuous mode of the RFQ cooler and buncher. It can be multiplied by the continuous transmission T_{RFQ} (Eq. (3.6)) for an overall RFQ "device" efficiency for bunches, but T_{RFQ} (in particular its component $\eta_{\text{injection}}$) strongly depends on the properties of the incident ion beam, as discussed earlier. This makes it impossible to give one value covering different ion sources and different working parameters thereof (temperature, gas load, etc.) as these are defining the beam properties.
Dealing with different masses that are accumulated and cooled in the RFQ requires the adjustment of the mass-dependent Mathieu parameters a and q according to Eq. (1.27). For the case of a=0, only the q-parameter has to be changed. It depends on V_{RF} and ν_{RF}, where V_{RF} can be manipulated easier as stated earlier (Sec. 2.2.5). The amplitude V_{RF} is chosen using Fig. 2.14, but it can also be verified experimentally, as shown in Fig. 3.24 and 3.25. If q>0.4, the pseudo-potential approximation

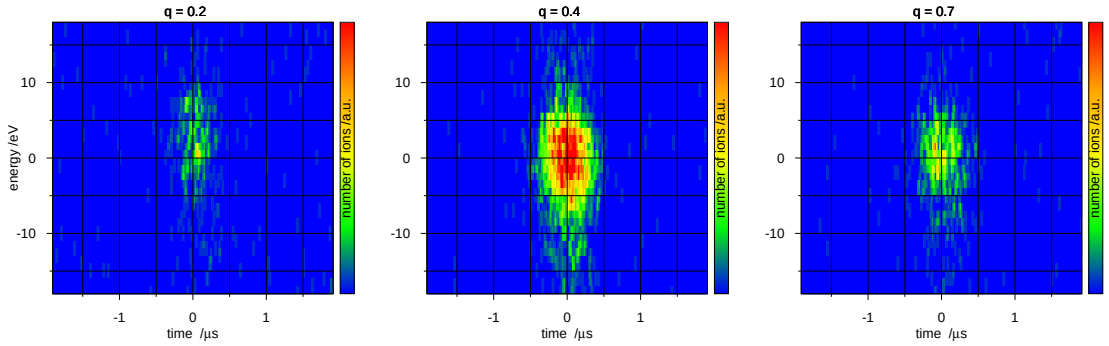

Figure 3.24: Ion bunch density plots for different values of the Mathieu q-parameter, for $^{40}Ca^{+}$ ions and ν_{RF}=1.0 MHz. The intensity scale is kept constant.

does not hold, and ions are not trapped efficiently. For smaller values of q (but identical ν_{RF}), the well D is not deep enough to trap the ions. The optimum value for q can be taken from Fig. 3.25. It seems to be around V_{RF}=80 V, or q=0.4, which is in perfect agreement with the theoretical prediction (see the red area in Fig. 2.14 for ν_{RF}=1.0 Mhz). The verification of the theoretical plot allows to set V_{RF} confidently for the masses of future measurements without the need for experimental optimization.

The bunching efficiency was determined in a separate measurement using a stable $^{39}K^{+}$ beam. The RFQ was set to continuous mode, and the ion beam current behind the RFQ I_{cooled} was measured. The RFQ was then set to bunching mode, and the number of ejected ions was measured with the Faraday cup equipped with the charge amplifier (Fig. 3.7) for different numbers of injected ions, controlled by t_{acc}. By solving Eq. (3.1) for η_{bunching}, the mean bunching efficiency was determined to 54.1(3.9) % [BBB+14].

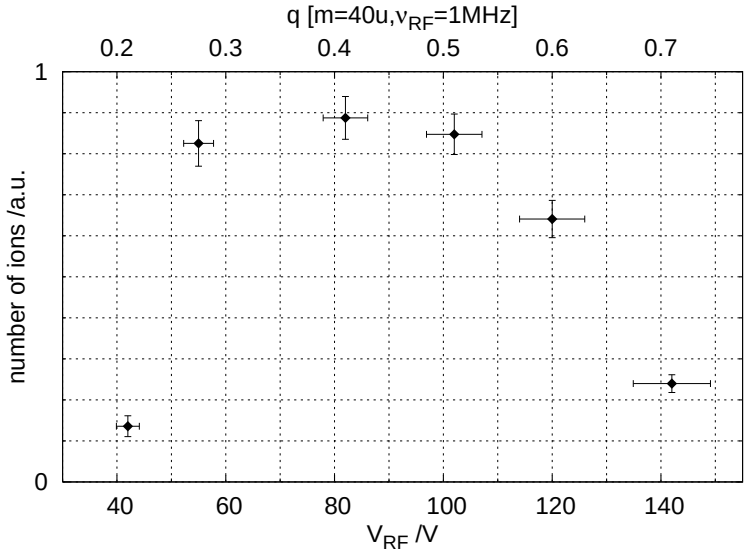

Figure 3.25: Number of $^{40}Ca^{+}$ ions in ejected bunches for different RF amplitudes V_{RF}. The corresponding Mathieu q-parameter is also shown for m=40 u and a fixed radio frequency ν_{RF}=1.0 MHz.

4 Offline measurements at TRIGA-LASER and TRIGA-TRAP

4.1 Measurement of the Hyperfine Structure of $^{43}Ca^{+}$

After the commissioning of the TRIGA-SPEC RFQ cooler and buncher, the parameters were optimized for the measurement of stable Ca^{+} isotopes. The ions of interest were produced in the online ion source by placing a small amount of Ca with natural abundance (see Fig. 4.1) into the tungsten tube. The differences of

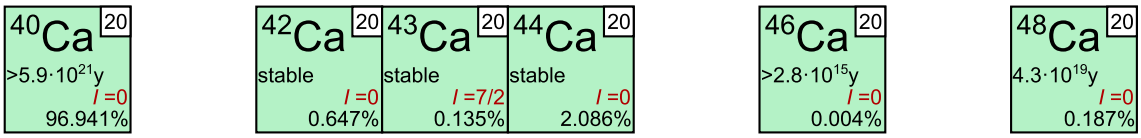

Figure 4.1: Stable isotopes of Ca, including half life, nuclear spin I, and natural abundance (data are taken from www.webelements.com and references therein). Electronic structure of the atom: $[Ar]4s^2$.

orders of magnitude in the natural abundance were compensated by adjusting t_{acc} and the temperature of the ion source to yield constant numbers of ions in ejected bunches of all isotopes (around 6000–20000). The dipole magnet separated the isotopes from each other so that the measurements could be performed without contaminant species. The power of the anti-collinear laser beam[1] at 397 nm was set to 130 µW. The $4^2S_{1/2}$–$4^2P_{1/2}$ resonances of $^{40}Ca^{+}$, $^{42}Ca^{+}$, $^{44}Ca^{+}$, and $^{48}Ca^{+}$ are shown in Fig. 4.2. $^{48}Ca^{+}$ required an accumulation time of t_{acc}=90 ms, the production of $^{46}Ca^{+}$ was too little for a measurement. A Voigt profile was fitted to each resonance to extract the FWHM, which is in the same range for each isotope. The values for the peak centers are in general used to derive the isotopic shifts (however, the required precision is not met in the measurements discussed here). The resonance of $^{42}Ca^{+}$ was taken with a different photomultiplier tube, one that had less photon efficiency, due to a technical problem. Therefore, the height of this resonance can not be compared to the other isotope's resonances. The ^{40}Ca peak shows a slight asymmetry, i.e., there are more slow ions (left side of the peak) than fast ions (right

[1] The continuous-wave laser beam is provided by a *Matisse TS* Ti:sapphire ring laser (794 nm), which is pumped by a *Coherent Verdi-V18* diode-pumped solid-state laser at 532 nm. The 794 nm beam is frequency-doubled in a bow-tie cavity with a BBO crystal for second-harmonic generation (*Spectra-Physics WaveTrain*) at 397 nm.

side of the peak). Such a behavior can be the result of collisions between the ions in the bunch and residual gas, e.g., at the exit of the buncher where the buffer gas is still partly present. The velocity damping of these collisions is velocity dependent (see Sec. 1.2.3), resulting in an asymmetry in the flight time. However, the source of the asymmetry is so far not finally clear and currently under investigation. It was the first time for the TRIGA-LASER experiment to record the resonances of an electronic transition of a mono-isotopic, cooled, and bunched ion beam.

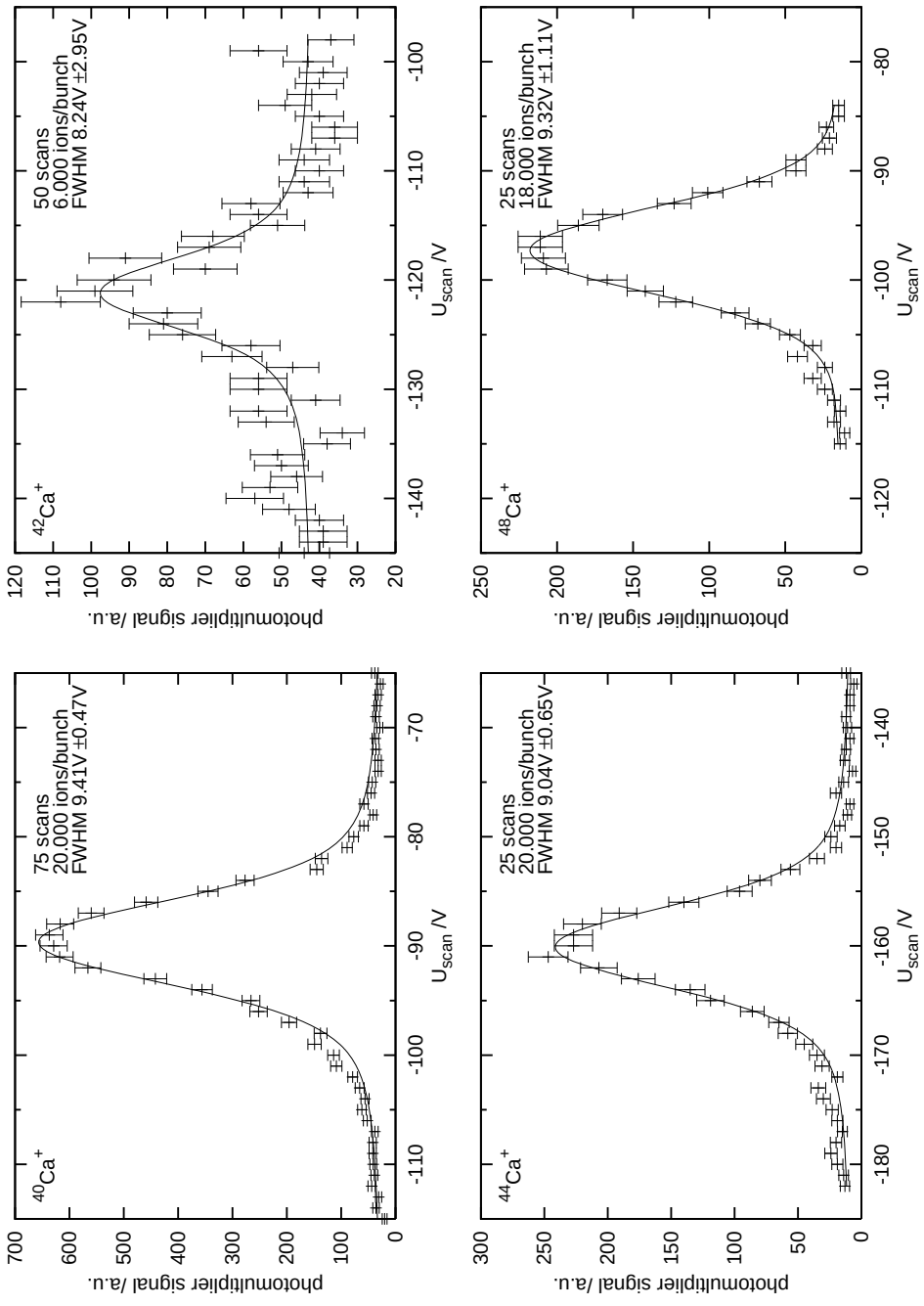

Figure 4.2: Photomultiplier response as a function of the scan voltage U_{scan}, for the stable even isotopes of calcium $^{40}Ca^+$, $^{42}Ca^+$, $^{44}Ca^+$, and $^{48}Ca^+$. The measurements were taken by time-resolved anti-collinear laser spectroscopy with a frequency-stabilized laser beam at 397 nm. A Voigt profile is fitted to the data points. For details, see the text.

With the energy spread and temporal width of the ion bunches generated by the RFQ, it is possible to resolve the Hyperfine Structure (HFS) of the only stable odd-mass isotope $^{43}Ca^+$. $^{43}Ca^+$ has a non-vanishing nuclear spin (I=7/2), the size of the energy shift for the different HFS components is given by Eq. (2.41). The HFS of ^{43}Ca has been investigated in a number of optical transitions mostly in the atomic spectrum (e.g., [KKT+79, PBB+84, SVNL91, NBI+98] and references therein). The energy level diagram showing the HFS of the 397 nm transition in $^{43}Ca^+$ is depicted in Fig. 4.3. Due to the nuclear spin of $^{43}Ca^+$, the energy levels split into several

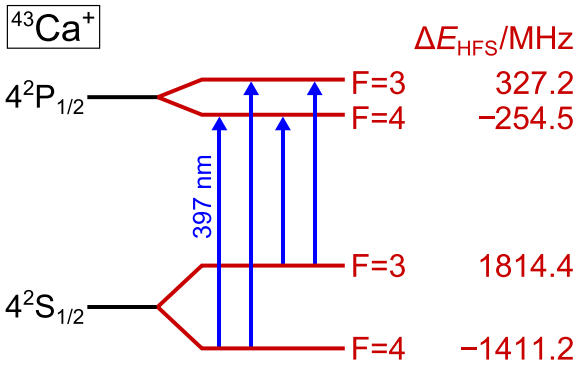

Figure 4.3: Energy level diagram for the $4^2S_{1/2}$–$4^2P_{1/2}$ transition (397 nm) in $^{43}Ca^+$ (excerpt from Fig. 2.35). The numbers in red denote the energy difference to the center (non-split) level.

hyperfine levels according to Eq. (2.39). Since J=1/2 and I=7/2, the total angular momentum quantum number $|\vec{F}|=|\vec{I}+\vec{J}|$ takes the values F=3 and F=4. Therefore, four resonances are expected in the spectrum of $^{43}Ca^+$, if the resolving power is sufficient. At TRIGA-LASER, all HFS levels could be addressed by the variation of U_{scan} over a range of 750 V, in a single scan. The ejection frequency of the RFQ was set to 10 Hz, as $t_{\text{acc}}\approx$90 ms and t_{cool}=10 ms. The resulting resonance spectrum is shown in Fig. 4.4. The four resonances are clearly separated and can be fitted with a routine that includes the hyperfine A and B factors (Eq. (2.43)), the Casimir factor C (Eq. (2.42)), and assumes Voigt profiles. As U_{scan} is negative, the ion bunches are accelerated at the entrance to the ODU, gaining kinetic energy. The laser beam is anti-collinear to the propagation axis of the bunches, thus resonances located on the right side of the spectrum (at smaller re-acceleration voltages) correspond to transitions with higher energies than resonances located on the left side of the spectrum (at higher re-acceleration voltages). Knowing that the energy difference in the $4^2S_{1/2}$ state is greater than the energy difference in the $4^2P_{1/2}$ state, the resonances can be sorted as follows (from left to right in Fig. 4.4):

1. $4^2S_{1/2}$,F=4 → $4^2P_{1/2}$,F=3
2. $4^2S_{1/2}$,F=4 → $4^2P_{1/2}$,F=4
3. $4^2S_{1/2}$,F=3 → $4^2P_{1/2}$,F=3

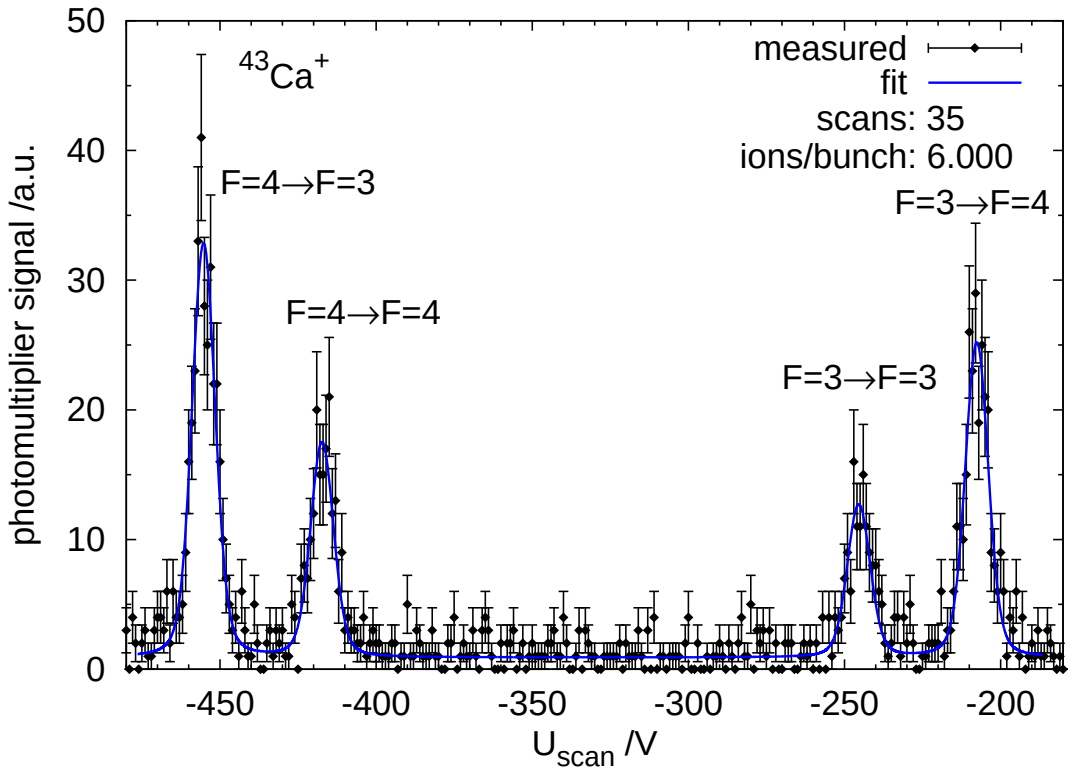

Figure 4.4: Photomultiplier response as a function of the scan voltage U_{scan}, for the stable odd isotope $^{43}Ca^{+}$. For details, see the text.

4. $4^2S_{1/2}$,F=3 $\rightarrow$ $4^2P_{1/2}$,F=4.

Because $B(4^2S_{1/2})$ and $B(4^2P_{1/2})$ do not contribute to the hyperfine splitting (ΔE_{eq} is zero for $J=1/2$ or s-electrons, see second term of Eq. (2.41)), the hyperfine A factor is extracted from the fit by comparing the relative center frequencies of the resonances and their heights. The fit yields

$$A(4^2S_{1/2}) = -803.6\,(1.2)\,\text{MHz}, \tag{4.1}$$
$$A(4^2P_{1/2}) = -145.1\,(1.1)\,\text{MHz}. \tag{4.2}$$

The stated errors are only the *statistical* errors from the fit routine, an extensive error analysis would additionally include *systematic* errors of the measurement technique and the apparatus, which is not deemed necessary for the "proof-of-principle" measurement performed in this case. However, the values do not deviate significantly from the literature values, i.e., $A(4^2S_{1/2})=-806.40207160(8)$ MHz in [ABG+94] and $A(4^2P_{1/2})=-145.4(0.1)$ MHz in [NBI+98] (or theor. values stated in [YWGS04]). Using the Casimir formula (Eq. (2.41)) and the experimentally determined A factors, one can also calculate the values for the energy deviations given in Fig. 4.3, verifying that they match within 0.5%.

4.2 Measurement of the TOF-ICR of $^{85}Rb^{+}$

To prove the performance of the ion beam preparation transfer line for the TRIGA-TRAP experiment, the time-of-flight ion cyclotron resonance (TOF-ICR) of an ion produced in the online ion source was recorded in the precision Penning trap. The element that is produced in the reactor *and* most efficiently ionized in the online ion source is rubidium, thus a stable isotope ($^{85}Rb^{+}$) was chosen for a TOF-ICR measurement.
The KCl carrier particles contain small amounts of natural Rb and Sr, the corresponding part of the mass spectrum is shown in Fig. 4.5. Both elements have

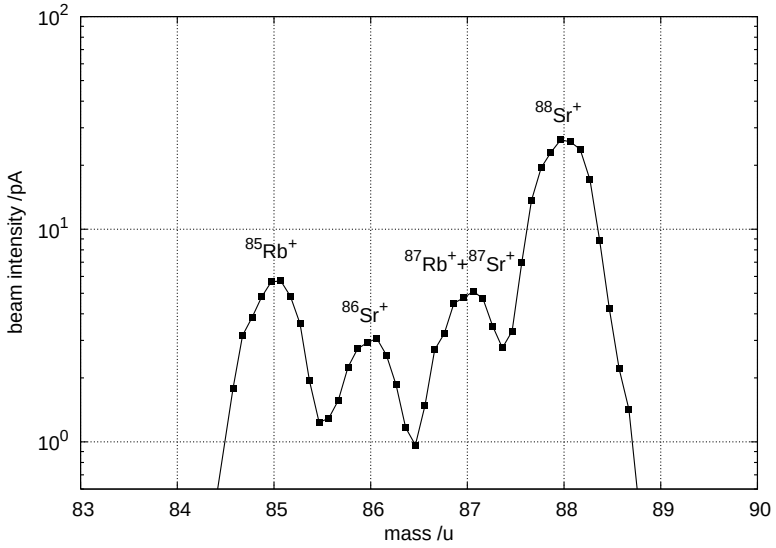

Figure 4.5: Mass spectrum of Rb^{+} and Sr^{+} with natural abundance, recorded on a Faraday cup behind the separator magnet. The nuclides are contained in the KCl carrier molecules as contaminants.

stable isotopes with mass 87 u, so the measurement candidate was the pure $^{85}Rb^{+}$ ion to avoid isobaric contamination. They were injected and prepared in the RFQ cooler and buncher as described in Sec. 2.2.5. The bunches were then decelerated in the electrostatic deceleration stage (Sec. 2.3.3) and transported toward the Penning traps (for an efficiency assessment, see the next section). After injection into the purification trap, the TOF-ICR measurement cycle described in Sec. 2.3.2 is started. A 700-ms continuous excitation at $\nu_c = \nu_+ + \nu_-$ was chosen (see Tab. 2.1). It took about half an hour until 64 scans were completed, each scan consisting of 40 frequency steps of ν_c. The obtained time-of-flight spectrum is shown in Fig. 4.6. The data were taken without Ramsey excitation although that is possible, as a precise mass measurement of this nuclide is not required. Therefore, also the magnetic field B was not calibrated with carbon clusters. However, the ion cyclotron resonance of $^{85}Rb^{+}$ is clearly observed. It was the first time that the cyclotron frequency of a nuclide produced in the online ion source was successfully measured at TRIGA-TRAP.

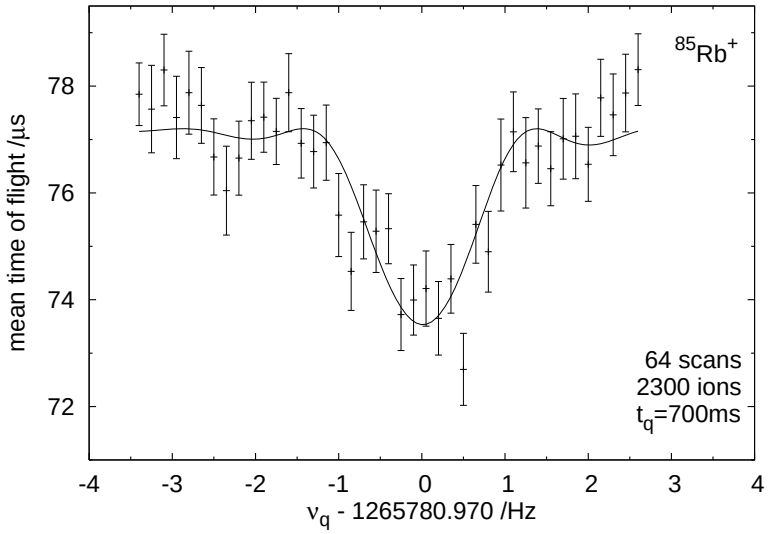

Figure 4.6: First TOF-ICR spectrum at TRIGA-TRAP of an ion produced in the online surface ionization ion source, in this case $^{85}Rb^{+}$. For details, see the text.

4.3 Efficiency assessment of the ion beam preparation transfer line

The total efficiency of the TRIGA-SPEC apparatus determines whether, or to which precision, measurements of the radionuclides of interest can be carried out. In the context of this thesis, the ion beam transfer line was finalized and put into operation, so the efficiencies of the individual sections can be determined. Those parts of the apparatus whose efficiency has to be improved can be identified to enable measurements of scarcely-produced nuclides. The schematic drawing of the TRIGA-SPEC apparatus is shown once again in Fig. 4.7. This time, the efficiencies of the appropriate sections of the beam line are included.

The fact that the fissionable target where the radioactive nuclides are produced is mounted on a target holder (see Fig. 2.5) reduces the available solid angle for fission products leaving the target by more than 50 %, as fission products having a velocity vector towards the target holder or perpendicular to the target are absorbed immediately. Additionally, the target is covered with a 13 µm thick aluminum foil that aims to absorb the fission products of the heavy branch. The reason is the practical decision not to contaminate the apparatus with long-lived fission products (the heavy branch contains a few nuclides with comparably long half lives, e.g., ^{137}Cs) until the commissioning is done and nuclides from the light branch were successfully measured. However, the aluminum foil also creates a lower transmission for the light branch of the fission products, decreasing the transmission for these nuclides to $\eta_{\text{foil}}\approx 5.0\,\%$ (simulated with SRIM[2]). The transport efficiency of the capillary is $\eta_{\text{cap.}}\approx 30\,\%$, and the efficiency of the skimmer is $\eta_{\text{skimmer}}\approx 15\,\%$ (determined by radioactive-particle collections with subsequent γ measurements). Thus, from the radionuclides produced by fission inside the reactor, approximately $1.2\cdot 10^{-3}$ successfully enter the ion source.

The ionization efficiency of the surface ionization ion source is, as explained in Sec. 2.2.3, foremost a function of the atomic species. Rubidium as an alkali metal has an ionization efficiency close to unity (Fig. 2.8), and the transmission of ^{91}Rb through the source exit orifice and the dipole magnet was determined to be $\eta_{\text{IS}}(^{91}\text{Rb})\approx 5\,\%$ by radioactive-particle collections. Latest tests show that the rate of transported ^{91}Rb ions through the mass separator is about 130 ions per second. The injection efficiency into the RFQ cooler and buncher can be estimated with the transmission of an ion beam in the RFQ's continuous mode, $\eta_{\text{inject}}\approx 25\%$ (Sec. 3.3.1). The transmission for Rb and Cs ions is approximately 33 %, most likely due to the increased mass ratio of the ions and the buffer gas, resulting in a more efficient cooling. The bunching efficiency was determined for K to be $\eta_{\text{bunching}}\approx 54\,\%$ (Sec. 3.3.5).

The transmission of the experimental branch TRIGA-LASER for a continuous beam is $\eta_{\text{LASER}}\approx 20\,\%$, determined by a Faraday-cup measurement. It is comparably easy to transport a fast 30 keV beam or bunch through a beam line, but the

[2]SRIM is a software tool to simulate the **S**topping and **R**ange of **I**ons in **M**atter. From www.srim.org

transmission of TRIGA-TRAP with a transport energy of ∼1 keV is more complex. The efficiency of the electrostatic deceleration stage (Sec. 2.3.3) was estimated for very small ion bunches (∼50 ions/bunch) to be $\eta_{\mathrm{EDS}} \approx 50\,\%$[3]. After being decelerated, the bunch is transported with a forward kinetic energy of ∼1 keV through the TRIGA-TRAP transfer line and injected into the purification Penning trap. The transmission of TRIGA-TRAP up to the Penning trap entrance was estimated in earlier times with a continuous Cs ion beam to around 30 % [Ket10], but can not be trustfully measured with the currently installed detection systems. The injection efficiency into the first Penning trap strongly depends on the energy spread of the ion bunch. The fact that the ion bunches are decelerated from the transport energy of 1 keV down to about 50 eV and subsequently have to match the acceptance of the trap makes the adjustment a complicated task. The measurement of $^{85}Rb^{+}$ was only possible by setting the number of ions per bunch to the RFQ limit of about $1{\cdot}10^{6}$ to record a time-of-flight spectrum with up to 50 ions per shot. However, at the time of this measurement the energy spread of the released ion bunches was more than an order of magnitude higher than at the end of the commissioning phase (around 180 eV), which should explain a low transmission and a low injection efficiency into the Penning trap. However, there is still a need that the ion-optical elements have to be optimized to increase the transmission and injection for future online measurements.

[3] Due to the lack of quantitative ion detectors at TRIGA-TRAP, this value was derived from an MCP signal. Different detection efficiencies resulting from different kinetic energies were considered. Although this signal showed a linear behavior for 25, 50 and 100 ions per bunch, the value has to be treated with caution.

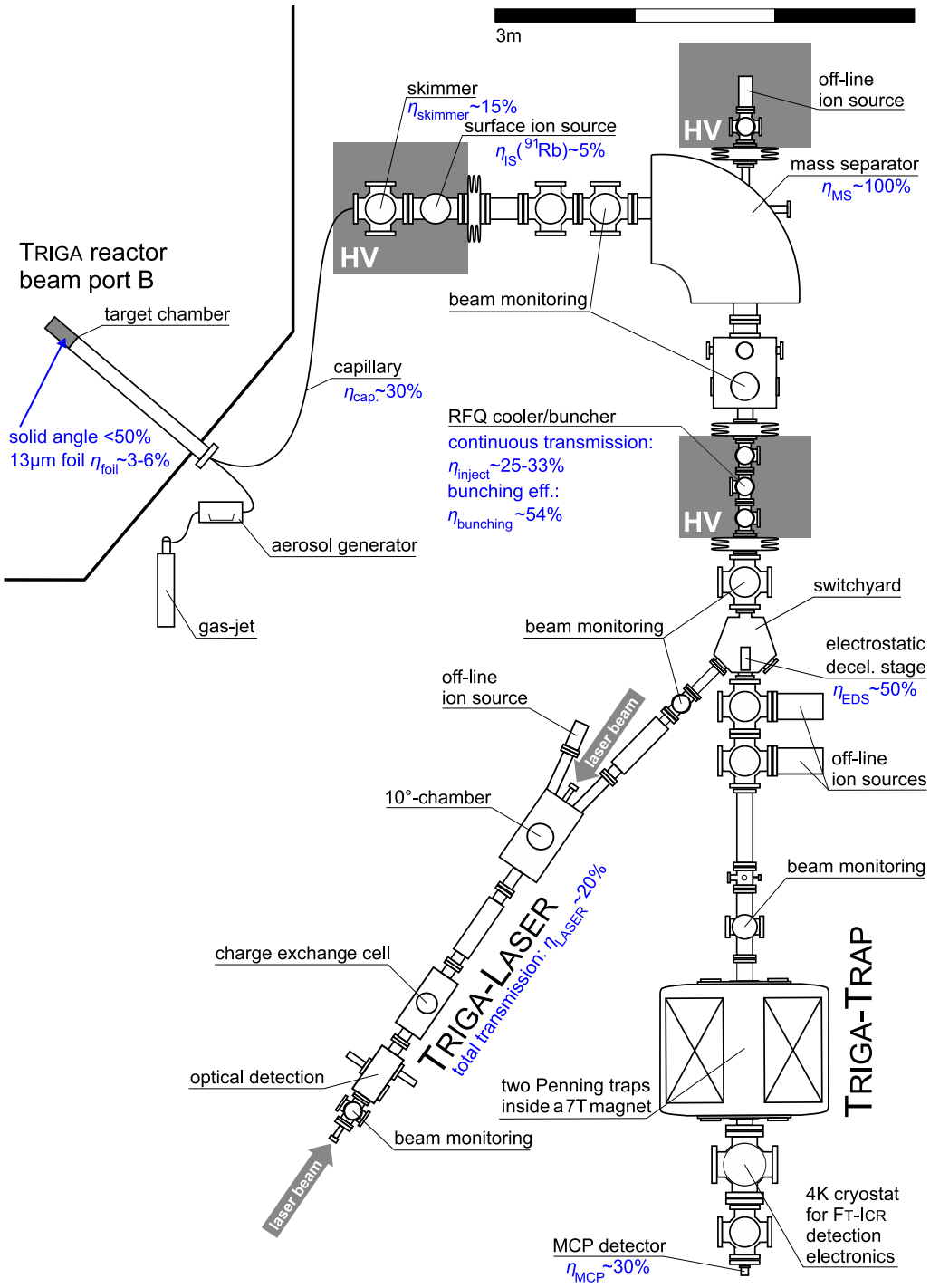

Figure 4.7: The TRIGA-SPEC experimental setup. Determined efficiencies are displayed in blue and explained in the text.

5 Conclusions and Outlook

5.1 Summary

Within this work, a radio-frequency-quadrupole cooler and buncher has been implemented and commissioned at the TRIGA-SPEC ion beam preparation transfer line. To this end, the former COLETTE ion beam cooler has been installed in Mainz and upgraded with the ability to form ion bunches, which is required by the experimental branches TRIGA-LASER and TRIGA-TRAP. In addition, a dipole magnet for in-flight mass separation, an advanced system for ion beam diagnosis, and an electrostatic deceleration stage were implemented and characterized with ion species from various sources. The installation included the setup of a high-voltage platform, the design of a motorized slit system for the separator, and the realization of a LabView©-based remote control for these components.

In a second step, these components were commissioned and their working parameters optimized for maximum efficiency. The mass resolving power of the dipole magnet was determined to R=244, the stability of the magnetic field to $\Delta\vec{B}/\vec{B}$=2.4·10^{-4}, or 0.07 u, for masses around 133 u (heavy fission branch). The ion beam diagnostics are able to detect ion currents from single ions to hundreds of µA, deliver optical images of the intensity distributions of beams and bunches, and can measure the number of ions in bunches from 10^4 to 10^6 ions/bunch. The RFQ cooler and buncher can significantly reduce the motional amplitudes of continuous ion beams, and deliver well-prepared ion bunches of up to 7·10^5 ions/bunch. The longitudinal FWHM energy spread of ejected ion bunches can be as low as 9 eV, their temporal FWHM can be reduced to ∼250 ns at the cost of an increased energy spread. The longitudinal emittance of an optimized ion bunch can reach $\varepsilon_{z,\mathrm{FWHM}}$=3.52(53) eVµs. The storage life time of ions inside the RFQ is $t_{\frac{1}{2}}$=22.5(2.0)s, and the bunching efficiency was determined to η_{bunching}=54.1(3.9) %.

The ion beam preparation transfer line was completed by the incorporation of these components. For the first time, ions produced in the online ion source which is connected to the reactor could be distributed to the experimental branches. To prove the functionality of the of the whole transfer line, offline measurements at both branches with ions produced in the online ion source were performed. At TRIGA-LASER, the $4^2\mathrm{S}_{1/2}$–$4^2\mathrm{P}_{1/2}$ resonances of stable Ca^+ isotopes, and the hyperfine structure of the only stable odd isotope $^{43}\mathrm{Ca}^+$ were observed with time-resolved laser spectroscopy. At the double Penning-trap mass spectrometer TRIGA-TRAP, the electrostatic deceleration stage was able to slow down ion bunches of stable $^{85}\mathrm{Rb}^+$, and a TOF-ICR spectrum of the latter was recorded. Finally, the efficiencies of most beam line components were determined.

5.2 Future efficiency improvements at TRIGA-SPEC

The fact that the experimental branches TRIGA-TRAP and TRIGA-LASER can conduct measurements on nuclides produced by the online source (see Chap. 4) shows that the TRIGA-SPEC apparatus is functional. Yet, further improvements are necessary, including foremost an increase in efficiency as the production rates of radioactive nuclides in the reactor are low compared to those of stable nuclides brought into the source. At the moment, there are several sections at the ion beam preparation transfer line where efficiency improvements are possible. The next sections provide a short overview on improvements that are currently in preparation or even in the commissioning phase.

5.2.1 An aerodynamic-lens–nozzle inlet to improve the skimmer efficiency

An aerodynamic-lens–nozzle inlet installed in front of the skimmer can significantly increase the efficiency of the latter, boosting the injection of radioactive nuclides into the online ion source [ZSW+04]. So far, the skimmer efficiency was determined by γ-measurements of radioactive particle collections to 15 % for a skimmer orifice of 1 mm in diameter. The task of an aerodynamic-lens–nozzle inlet is to contract the heavy particles inside an aerosol gas stream onto the center propagation axis and to reduce their angular divergence at its exit [Gru14].
In short, the aerodynamic-lens–nozzle inlet consists of several circular-shaped plates with a center orifice, arranged in succession inside a cylindrical tube, and separated by spacers. At the positions of the orifices, the particle speed is increased and the stream contracted, altering the divergence angle afterward (hence, the orifice is called "lens"). The contraction ratio, transmission efficiencies and divergence angles are determined by particle Stokes number, flow Reynolds number, and lens geometry [ZSW+02]. Thus, by adjusting the lens geometry and stacking several lenses into the particle stream, a specific particle size and flow can be chosen to yield minimal divergence angle and maximal stream contraction. The simulated trajectories of particles having 500 nm in diameter through an optimized aerodynamic lens are shown in Fig. 5.1.

For TRIGA-SPEC, the parameters of the aerodynamic-lens–nozzle inlet were adapted to the carrier particles. Using KCl, the particle diameter is 75–175 nm, and the optimum transport efficiency was realized at a regulated nitrogen transport gas flow of 400 ml/min. A 3D model of the aerodynamic-lens–nozzle inlet adapted to TRIGA-SPEC is shown in Fig. 5.2.

Preliminary tests show that the transmission through the aerodynamic-lens–nozzle inlet is $\eta_{\text{lens}} \approx 84\,\%$. Due to a much smaller opening angle at its exit, the implementation boosts the skimmer efficiency to $\eta_{\text{skimmer}} \approx 78\,\%$. The total transmission then yields 65(8) %, which is an improvement of more than a factor of 4 when compared

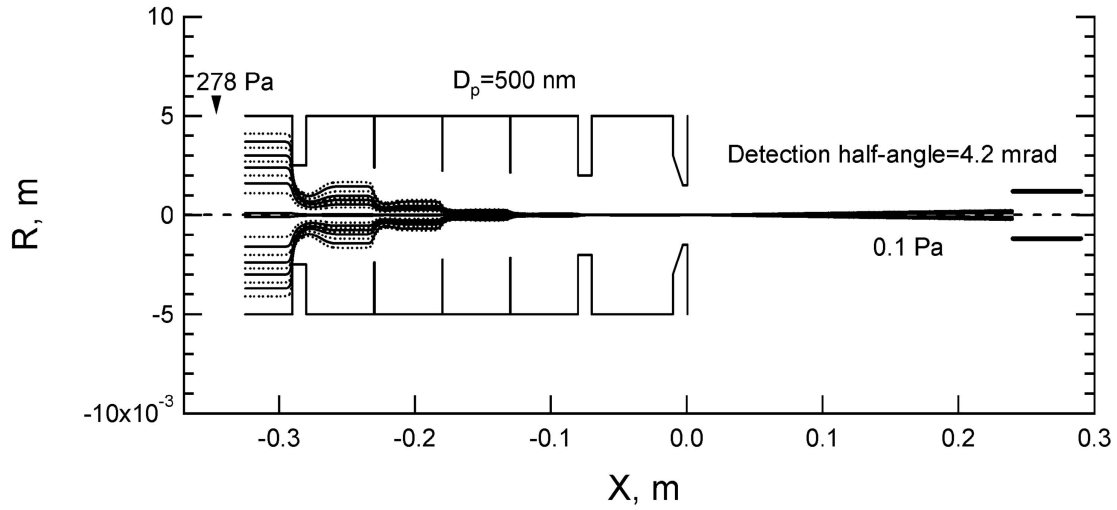

Figure 5.1: Simulated trajectories of particles having 500 nm in diameter through an optimized aerodynamic-lens–nozzle inlet, from [ZSW+04]. A laminar particle stream enters the six-lens system from the left, the different lines represent different distances to the center axis. At the exit nozzle, the particles are contracted to the center axis, showing a small angular divergence after leaving the lens system.

Figure 5.2: 3D model of the aerodynamic-lens–nozzle inlet being tested at TRIGA-SPEC [Gru14].

to the skimmer efficiency without the aerodynamic-lens–nozzle inlet. As the carrier particles with the attached fission products fit more efficiently through the skimmer, even a smaller skimmer diameter can be utilized to reduce the transport gas load in the ion source [Gru17].

5.2.2 A plasma ionization ion source to ionize refractory fission products

As discussed earlier, the current online ion source is limited regarding the elements that can be ionized (Sec. 2.2.3). For the full potential of TRIGA-SPEC, an ion source capable of ionizing every fission product has to be installed. This includes refractory elements (elements with melting points higher than iron, cobalt and nickel) as well as some other metalloids like tellurium or antimony, for which the reactor's production rates are high enough to touch or even cross the expected r-process path (Fig. 2.4).

To this end, an ECR ion source has been installed and tested at the ion beam preparation transfer line, but the efficiency of separating the fission products from the carrier particles and ionizing them did not meet the requirements (details on the commissioning of the ECR ion source can be found in [Smo12]). Thus, a hollow cathode ion source is developed in parallel to the operation of the present ion source [Sch15]. The design follows the one of [MWWL76], a drawing is shown in Fig. 5.3. A stable discharge arc is created in between the anode and cathode, the cathode is

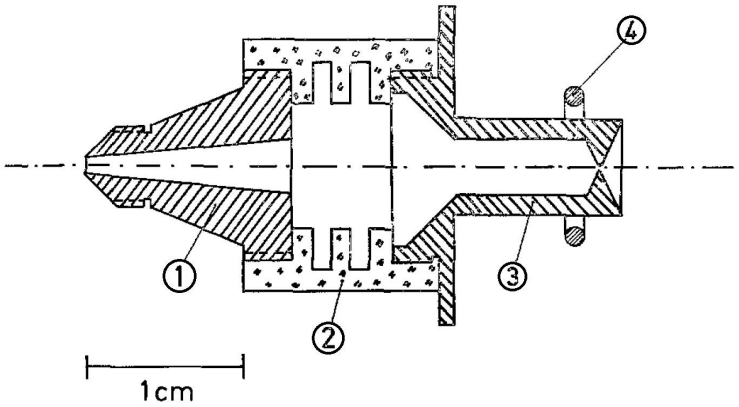

Figure 5.3: Cross section of the hollow cathode ion source, from [MWWL76]. ① Anode (Ta); ② insulator (BN); ③ cathode (Ta); ④ heating filament (Ta).

heated through electron bombardment to increase the number of emitted electrons. Typical arc voltages are 100–150 V at 1.5 A arc current. The generated ion current contains several tens of µA, which is mostly background gas and carrier particle materials [MWWL76]. At that time, ion source efficiencies for different elements have been determined via β-activity measurements of samples collected behind the ion source. K_α peak ratios of 1–3 % have been observed for Te, I, Xe, Cs, Ba, and La. The ionization efficiency was also determined by γ-measurements and was in the 1 % range (e.g., ^{134}Te had 0.8(4) %).

5.2.3 A larger actinide target to increase the radioactive-nuclide production rates

Apart from efficiency improvements at the apparatus, another way to increase the number of radioactive nuclides per time unit is to increase their production rates already inside the TRIGA reactor. This can be done by altering the actinide target, as it is planned for the next online commissioning phase. The 310 µg ^{235}U target will be exchanged by a 1 mg target of the same material, which is an increase of a factor of 3 in fissionable material (and thus in the production of fission products, assuming a similar target thicknesses). Additionally, the Al foil that covers the target material (currently 13 µm) will be substituted by a thinner Al foil of 10 µm thickness. Thereby, the stopping power is reduced, but at the same time the transmission of nuclides from the light fission branch is increased by a factor of 4 [FHKS51]. The free volume of the target chamber for the stopping path of the fission products was designed for He as stopping gas and a 13 µm thick Al cover. Using a thinner Al cover, the energy of the fission products leaving the foil is higher, thus a larger target chamber, a higher gas pressure, or a different gas with a higher stopping power has to be used. As the latest tests were anyhow performed with N instead of He as transport gas, a modification of the target chamber is not necessary. Hence, the combination of a larger actinide target and a thinner Al foil should increase the production rates of the radioactive nuclides by a factor of $\sim$12.

5.2.4 Enhanced ion beam diagnosis at TRIGA-TRAP to increase the transport efficiency

To boost the transmission of bunches in the ion beam transfer line of TRIGA-TRAP, a detection system very similar to the one installed and commissioned in the course of this thesis (see Sec. 3.2) will be implemented shortly after the electrostatic deceleration stage. The system is modified to fit into a slightly smaller volume which is required in the transfer line, the functionality will be the same. Thereby, it will be possible to exactly determine the number of ions per bunch with a charge amplifier attached to a Faraday cup as presented in Sec. 3.2, which is useful to reliably determine the efficiency of the deceleration stage. Moreover, the phosphor screen can be used to optimize the position spread of the decelerated bunch for an increased transmission through the transfer line and more efficient injection into the Penning trap.

5.3 Outlook

With the completion of the ion beam preparation transfer line, the experimental branches TRIGA-LASER and TRIGA-TRAP are coupled to the research reactor. Thus, TRIGA-SPEC has made a large step forward to its aim: the high-precision measurements of ground-state properties of neutron-rich nuclides, which will be used to test the predictive power of astrophysical models. The next step is to perform a mass measurement on one of the nuclides with high production rates and ionization yields (e.g., $^{91}Rb^{+}$). After further optimization and the improvements mentioned above, the full spectrum of fission fragments can be accessed and distributed to both experimental branches. Future perspectives of TRIGA-SPEC include the implementation of advanced ICR detection techniques at TRIGA-TRAP as described in Sec. 2.3.2, or the use of two counter-propagating laser beams for Doppler elimination at TRIGA-LASER. An additional ion-source upgrade involving resonant laser ionization is planned to boost the ionization efficiencies of certain elements. The implementation of efficiency-increasing methods and techniques at the two experimental branches are also part of the preparation for the MATS and LaSpec experiments within the NUSTAR collaboration at the future FAIR facility at GSI. This facility will provide ion beams with unrivaled yields, and TRIGA-SPEC will contribute its knowledge and equipment for high-precision measurements on the properties of the most exotic nuclides.

Bibliography

[AAB+93] K. Abrahamsson, G. Andler, L. Bagge, E. Beebe, P. Carlé, H. Danared, S. Egnell, K. Ehrnstén, M. Engström, C.J. Herrlander, J. Hilke, J. Jeansson, A. Källberg, S. Leontein, L. Liljeby, A. Nilsson, A. Paal, K.-G. Rensfelt, U. Rosengård, A. Simonsson, A. Soltan, J. Starker, M.af Ugglas, and A. Filevich. CRYRING - a synchrotron, cooler and storage ring. *Nucl. Instr. Meth. B*, 79(1-4):269–272, 1993.

[AABR+10] G. B. Andresen, M. D. Ashkezari, M. Baquero-Ruiz, W. Bertsche, P. D. Bowe, E. Butler, C. L. Cesar, S. Chapman, M. Charlton, J. Fajans, T. Friesen, M. C. Fujiwara, D. R. Gill, J. S. Hangst, W. N. Hardy, R. S. Hayano, M. E. Hayden, A. Humphries, R. Hydomako, S. Jonsell, L. Kurchaninov, R. Lambo, N. Madsen, S. Menary, P. Nolan, K. Olchanski, A. Olin, A. Povilus, P. Pusa, F. Robicheaux, E. Sarid, D. M. Silveira, C. So, J. W. Storey, R. I. Thompson, D. P. van der Werf, D. Wilding, J. S. Wurtele, and Y. Yamazaki. Evaporative cooling of antiprotons to cryogenic temperatures. *Phys. Rev. Lett.*, 105:013003, Jul 2010.

[ABB+06] F. Ames, R. Baartman, P. Bricault, K. Jayamanna, M. McDonald, M. Olivo, P. Schmor, D. H. L. Yuan, and T. Lamy. Charge state breeding of radioactive ions with an electron cyclotron resonance ion source at TRIUMF. *Rev. Sci. Instrum.*, 77(3), 2006.

[ABG+94] F. Arbes, M. Benzing, Th. Gudjons, F. Kurth, and G. Werth. Precise determination of the ground state hyperfine structure splitting of ^{43}Ca II. *Z. Phys. D*, 31(1):27–30, 1994.

[AEM+95] M. H. Anderson, J. R. Ensher, M. R. Matthews, C. E. Wieman, and E. A. Cornell. Observation of Bose-Einstein condensation in a dilute atomic vapor. *Science*, 269(5221):198–201, 1995.

[AG89] E. Anders and N. Grevesse. Abundances of the elements: Meteoritic and solar. *Geochim. Cosmochim. Acta*, 53:197–214, 1989.

[AGT07] M. Arnould, S. Goriely, and K. Takahashi. The r-process of stellar nucleosynthesis: Astrophysics and nuclear physics achievements and mysteries. *Phys. Rep.*, 450(4-6):97–213, 2007.

[Alt93] G.D. Alton. Ion sources for accelerators in materials research. *Nucl. Instr. Meth. B*, 73(2):221–288, 1993.

[AS64] M. Abramowitz and I.A. Stegun. *Handbook of Mathematical Functions*. U.S. Govt. Printing Office, 1964.

[BAB+04] J. Bernard, J. Alonso, T. Beier, M. Block, S. Djekić, H.-J. Kluge, C. Kozhuharov, W. Quint, S. Stahl, T. Valenzuela, J. Verdú, M. Vogel, and G. Werth. Electron and positron cooling of highly charged ions in a cooler Penning trap. *Nucl. Instr. Meth. A*, 532(1-2):224 – 228, 2004. International Workshop on Beam Cooling and Related Topics.

[Bau67] E. Baust. Die Anlagerung von radioaktiven Atomen und Ionen an Aerosolteilchen. *Z. Phys.*, 199(2):187–206, 1967.

[BBB+14] T. Beyer, K. Blaum, M. Block, Ch.E. Düllmann, K. Eberhardt, M. Eibach, N. Frömmgen, C. Geppert, C. Gorges, J. Grund, M. Hammen, S. Kaufmann, A. Krieger, Sz. Nagy, W. Nörterhäuser, D. Renisch, C. Smorra, and E. Will. An RFQ cooler and buncher for the TRIGA-SPEC experiment. *Appl. Phys. B*, 114(1–2):129–136, 2014.

[BBFH57] E. M. Burbidge, G. R. Burbidge, W. A. Fowler, and F. Hoyle. Synthesis of the Elements in Stars. *Rev. Mod. Phys.*, 29:547–650, Oct 1957.

[BBH+02] K. Blaum, G. Bollen, F. Herfurth, A. Kellerbauer, H.-J. Kluge, M. Kuckein, E. Sauvan, C. Scheidenberger, and L. Schweikhard. Carbon clusters for absolute mass measurements at ISOLTRAP. *Eur. Phys. J. A*, 15(1–2):245–248, 2002.

[BC95] J. Billowes and P. Campbell. High-resolution laser spectroscopy for the study of nuclear sizes and shapes. *J. Phys. G: Nucl. Part. Phys.*, 21(6):707, 1995.

[BCH+81] M. Bell, J. Chaney, H. Herr, F. Krienen, P. Møller-Petersen, and G Petrucci. Electron cooling in ICE at CERN. *Nucl. Instr. Meth.*, 190(2):237 – 255, 1981.

[BDN13] K. Blaum, J. Dilling, and W. Nörtershäuser. Precision atomic physics techniques for nuclear physics with radioactive beams. *Phys. Scr.*, 2013(T152):014017, 2013.

[BDSW74] A. F. Bernhardt, D. E. Duerre, J. R. Simpson, and L. L. Wood. Separation of isotopes by laser deflection of atomic beams. I: Barium. *Appl. Phys. Lett.*, 25(10):617–620, 1974.

[Bet30] H. Bethe. Zur Theorie des Durchgangs schneller Korpuskularstrahlen durch Materie. *Ann. Phys.*, 397:325–400, 1930.

[BG82] L.S. Brown and G. Gabrielse. Precision spectroscopy of a charged particle in an imperfect Penning trap. *Phys. Rev. A*, 25:2423–2425, Apr 1982.

[BG86] L.S. Brown and G. Gabrielse. Geonium theory: Physics of a single electron or ion in a Penning trap. *Rev. Mod. Phys.*, 58:233–311, Jan 1986.

[BHK+85] M. Brügger, N. Hildebrand, T. Karlewski, N. Trautmann, A.K. Mazumdar, and G. Herrmann. Operation of a high temperature ion source at the helium-jet on-line isotope separator facility HELIOS. *Nucl. Instr. and Meth. A*, 234(2):218–223, 1985.

[BKK+92] G. Bollen, H.-J. Kluge, M. König, T. Otto, G. Savard, H. Stolzenberg, R. B. Moore, G. Rouleau, G. Audi, and ISOLDE Collaboration. Resolution of nuclear ground and isomeric states by a Penning trap mass spectrometer. *Phys. Rev. C*, 46:R2140–R2143, Dec 1992.

[BKQW89] R. Blümel, C. Kappler, W. Quint, and H. Walther. Chaos and order of laser-cooled ions in a Paul trap. *Phys. Rev. A*, 40:808–823, 1989.

[BKR+07] J. Benhelm, G. Kirchmair, U. Rapol, T. Körber, C. F. Roos, and R. Blatt. Measurement of the hyperfine structure of the $S_{1/2}$-$D_{5/2}$ transition in $^{43}Ca^{+}$. *Phys. Rev. A*, 75:032506, Mar 2007.

[Bla06] K. Blaum. High-accuracy mass spectrometry with stored ions. *Phys. Rep.*, 425(1):1–78, 2006.

[BLP+88] R. Blatt, G. Lafyatis, W.D. Phillips, S. Stenholm, and D.J. Wineland. Cooling in traps. *Phys. Scr.*, 1988(T22):216, 1988.

[BNW10] K. Blaum, Y. N. Novikov, and G. Werth. Penning traps as a versatile tool for precise experiments in fundamental physics. *Cont. Phys.*, 51(2):149–175, 2010.

[Brü83] M. Brügger. *Entwicklung einer Hochtemperaturoberflächenionenquelle für den Heliumjet Massenseparator HELIOS und Zerfallsstudien an massengetrennten neutronenreichen Praesodymisotopen.* PhD thesis, Johannes Gutenberg-Universität, Mainz, 1983.

[BS78] G.I. Budker and A.N. Skrinskiĭ. Electron cooling and new possibilities in elementary particle physics. *Sov. Phys. Uspekhi*, 21(4):277, 1978.

[BS85] A.M. Boesgaard and G. Steigman. Big Bang nucleosynthesis: Theories and observations. *Ann. Rev. Astron. Astrophys.*, 23:319–378, 1985.

[Bud67] G.I. Budker. Proceedings of the Intern. Symposium on Electron and Positron Storage Rings, Saclay, 1966. *Atomnaya Énergiya*, 22:346, 1967.

[BZHS86] R. Blatt, P. Zoller, G. Holzmüller, and I. Siemers. Brownian motion of a parametric oscillator: A model for ion confinement in radio frequency traps. *Z. Phys. D*, 4(2):121–126, 1986.

[Car72] J. P. Carrico. *Dynamic mass spectrometry*, volume 3. Heyden and Son, Ltd., 1972.

[CBD+93] J.E. Crawford, F. Buchinger, L. Davey, Y. Ji, J.K.P. Lee, J. Pinard, J.L. Vialle, and W.Z. Zhao. Laser desorption sources and time-of-flight injection for RFQ traps. *Hyperfine Interact.*, 81(1-4):143–149, 1993.

[CCTP97] S. Chu, C. Cohen-Tannoudji, and W. Phillips. The nobel prize in physics 1997, 1997.

[CD69] D. A. Church and H. G. Dehmelt. Radiative cooling of an electrodynamically contained proton gas. *J. Appl. Phys.*, 40(9):3421–3424, 1969.

[CF10] B. Cheal and K.T. Flanagan. Progress in laser spectroscopy at radioactive ion beam facilities. *J. Phys. G: Nucl. Part. Phys.*, 37(11):113101, 2010.

[CJWM70] T.A. Carlson, C.W. Nestor Jr., N. Wasserman, and J.D. McDowell. Calculated ionization potentials for multiply charged ions. *At. Data Nucl. Data Tables*, 2(0):63 – 99, 1970.

[CKW01] E.A. Cornell, W. Ketterle, and C.E. Wieman. The Nobel Prize in Physics 2001, 2001.

[CPBZ96] J.I. Cirac, A.S. Parkins, R. Blatt, and P. Zoller. Nonclassical states of motion in ion traps. *Adv. At. Mol. Opt. Phys*, 37:237–296, 1996.

[CTT91] J.J. Cowan, F.-K. Thielemann, and J.W. Truran. The r-process and nucleochronology. *Phys. Rep.*, 208(4-5):267 – 394, 1991.

[Daw76] P.H. Dawson. *Quadrupole Mass Spectrometry and its applications*. Elsevier Scientific Publishing Company, 1976.

[dDF+99] R. deCarvalho, J.M. Doyle, B. Friedrich, T. Guillet, J. Kim, D. Patterson, and J.D. Weinstein. Buffer-gas loaded magnetic traps for atoms and molecules: A primer. *Eur. Phys. J. D*, 7(3):289–309, 1999.

[Deh67] H.G. Dehmelt. Radiofrequency spectroscopy of stored ions I: Storage. *Adv. Atom. Mol. Phys*, 3:53–72, 1967.

[Dem96] W. Demtröder. *Experimentalphysik III*. Springer-Verlag Berlin, 1996.

[Dem07] W. Demtröder. *Laserspektroskopie*. Springer-Verlag Berlin Heidelberg, 2007.

[DMA+95] K. B. Davis, M. O. Mewes, M. R. Andrews, N. J. van Druten, D. S. Durfee, D. M. Kurn, and W. Ketterle. Bose-Einstein condensation in a gas of sodium atoms. *Phys. Rev. Lett.*, 75:3969–3973, Nov 1995.

[Dre68] M. J. Dresser. The Saha-Langmuir equation and its application. *J. Appl. Phys.*, 39(1):338–339, 1968.

[EBB+10] M. Eibach, T. Beyer, K. Blaum, M. Block, K. Eberhardt, F. Herfurth, C. Geppert, J. Ketelaer, J. Ketter, J. Krämer, et al. Transport of fission products with a helium gas-jet at TRIGA-SPEC. *Nucl. Instr. and Meth. A*, 613(2):226–231, 2010.

[EBB+11] M. Eibach, T. Beyer, K. Blaum, M. Block, K. Eberhardt, F. Herfurth, J. Ketelaer, Sz. Nagy, D. Neidherr, W. Nörtershäuser, and C. Smorra. First investigation of phase-shifted Ramsey excitation in Penning trap mass spectrometry. *Int. J. Mass Spectrom.*, 303(1):27–30, 2011.

[EBB+13] S. Eliseev, K. Blaum, M. Block, C. Droese, M. Goncharov, E. Minaya Ramirez, D. A. Nesterenko, Yu. N. Novikov, and L. Schweikhard. Phase-imaging ion-cyclotron-resonance measurements for short-lived nuclides. *Phys. Rev. Lett.*, 110:082501, Feb 2013.

[EBB+14] M. Eibach, T. Beyer, K. Blaum, M. Block, Ch.E. Düllmann, K. Eberhardt, J. Grund, Sz. Nagy, H. Nitsche, W. Nörtershäuser, D. Renisch, K.P. Rykaczewski, F. Schneider, C. Smorra, J. Vieten, M. Wang, and K. Wendt. Direct high-precision mass measurements on ^{241,243}Am, ^{244}Pu, and ^{249}Cf. *Phys. Rev. C*, 89:064318, Jun 2014.

[EBC+09] G. Eitel, M. Block, A. Czasch, M. Dworschak, S. George, O. Jagutzki, J. Ketelaer, J. Ketter, Sz. Nagy, D. Rodríguez, C. Smorra, and K. Blaum. Position-sensitive ion detection in precision Penning trap mass spectrometry. *Nucl. Instr. Meth. A*, 606(3):475 – 483, 2009.

[Eib13] M. Eibach. *High-precision mass measurements in the realm of the deformed shell closure N=152.* PhD thesis, Combined Faculties for the Natural Sciences and for Mathematics of the Ruperto-Carola-University of Heidelberg, Germany, 2013.

[EK00] K. Eberhardt and A. Kronenberg. The research reactor TRIGA Mainz - a neutron source for versatile applications in research and education. *Kerntechnik*, 65:269–274, 2000.

[EKK+83] T. Ellison, W. Kells, V. Kerner, F. Mills, R. Peters, T. Rathbun, D. Young, and P.M. McIntyre. Electron cooling and accumulation of 200-MeV Protons at Fermilab. *IEEE Trans. Nucl. Science*, 30(4):2636–2638, Aug 1983.

[EMSKB03] J. Eschner, G. Morigi, F. Schmidt-Kaler, and R. Blatt. Laser cooling of trapped ions. *J. Opt. Soc. Am. B*, 20(5):1003–1015, May 2003.

[ER95] T.R. England and B.F. Rider. *Evaluation and compilation of fission product yields 1993*. Los Alamos National Lab., Dec 1995.

[EWS+86] D.A. Eastham, P.M. Walker, J.R.H. Smith, J.A.R. Griffith, D.E. Evans, S.A. Wells, M.J. Fawcett, and I.S. Grant. Optical isotope shifts of ^{80,82}Sr from coincidence laser spectroscopy. *J. Phys. G: Nucl. Phys.*, 12(9):L205, 1986.

[FGM08] B. Franzke, H. Geissel, and G. Münzenberg. Mass and lifetime measurements of exotic nuclei in storage rings. *Mass Spectrom. Rev.*, 27(5):428–469, 2008.

[FHKS51] B. Finkle, E.J. Hoagland, S. Katcoff, and N. Sugarman. Ranges of fission-recoil fragments of known mass numbers (III). *Radio-Chemical Studies: The Fission products, Paper No. 46, National Nuclear Energy Series Plutonium Project Record*, 9:471, 1951.

[Fra02] G.W. Fraser. The ion detection efficiency of microchannel plates (MCPs). *Int. J. Mass Spectrom.*, 215(1–3):13 – 30, 2002. Detectors and the Measurement of Mass Spectra.

[Fri33] R. Frisch. Experimenteller Nachweis des Einsteinschen Strahlungsrückstoßes. *Z. Phys.*, 86(1-2):42–48, 1933.

[GBB+11] S. George, K. Blaum, M. Block, M. Breitenfeldt, M. Dworschak, F. Herfurth, A. Herlert, M. Kowalska, M. Kretzschmar, E. Minaya Ramirez, D. Neidherr, S. Schwarz, and L. Schweikhard. Damping effects in penning trap mass spectrometry. *Int. J. Mass Spectrom.*, 299(2–3):102 – 112, 2011.

[GBH+07] S. George, K. Blaum, F. Herfurth, A. Herlert, M. Kretzschmar, Sz. Nagy, S. Schwarz, L. Schweikhard, and C. Yazidjian. The Ramsey method in high-precision mass spectrometry with Penning traps: Experimental results. *Int. J. Mass Spectrom.*, 264(2):110–121, 2007.

[GFO+89] G. Gabrielse, X. Fei, L. A. Orozco, R. L. Tjoelker, J. Haas, H. Kalinowsky, T. A. Trainor, and W. Kells. Cooling and slowing of trapped antiprotons below 100 meV. *Phys. Rev. Lett.*, 63:1360–1363, Sep 1989.

[Gho95] Pradip K. Ghosh. *Ion traps*. Clarendon press Oxford, 1995.

[GJB+91] H.W. Gäggeler, D.T. Jost, U. Baltensperger, A. Weber, A. Kovacs, D. Vermeulen, and A. Türler. OLGA II, an on-line gas chemistry apparatus for applications in heavy element research. *Nucl. Instr. Meth. A*, 309(1–2):201 – 208, 1991.

[GKT80] G. Gräff, H. Kalinowsky, and J. Traut. A direct determination of the proton electron mass ratio. *Z. Phys. A*, 297(1):35–39, 1980.

[GNA+74] A. Ghiorso, J. M. Nitschke, J. R. Alonso, C. T. Alonso, M. Nurmia, G. T. Seaborg, E. K. Hulet, and R. W. Lougheed. Element 106. *Phys. Rev. Lett.*, 33:1490–1493, Dec 1974.

[Gru14] J. Grund. Optimierung des Gas-Jet-Systems bei TRIGA-SPEC. Diploma thesis, Institut für Kernchemie, Johannes Gutenberg-Universität Mainz, 2014.

[Gru17] J. Grund. *Massenmessung neutronenreicher Spaltprodukte und langlebiger Transuranisotope bei TRIGA-SPEC*. Phd thesis, Institut für Kernchemie, Johannes Gutenberg-Universität Mainz, 2017.

[HAB+00] M. Hausmann, F. Attallah, K. Beckert, F. Bosch, A. Dolinskiy, H. Eickhoff, M. Falch, B. Franczak, B. Franzke, H. Geissel, Th. Kerscher, O. Klepper, H.-J. Kluge, C. Kozhuharov, K.E.G. Löbner, G. Münzenberg, F. Nolden, Yu.N. Novikov, T. Radon, H. Schatz, Ch. Scheidenberger, J. Stadlmann, M. Steck, T. Winkler, and H. Wollnik. First isochronous mass spectrometry at the experimental storage ring ESR. *Nucl. Instr. Meth. A*, 446(3):569 – 580, 2000.

[HBB+89] D. Habs, W. Baumann, J. Berger, P. Blatt, A. Faulstich, P. Krause, G. Kilgus, R. Neumann, W. Petrich, R. Stokstad, D. Schwalm, E. Szmola, K. Welti, A. Wolf, S. Zwickler, E. Jaeschke, D. Krämer, G. Bisoffi, M. Blum, A. Friedrich, C. Geyer, M. Grieser, H.W. Heyng, B. Holzer, R. Ihde, M. Jung, K. Matl, W. Ott, B. Povh, R. Repnow, M. Steck, E. Steffens, D. Dutta, T. Kühl, D. Marx, S. Schröder, M. Gerhard, R. Grieser, G. Huber, R. Klein, M. Krieg, N. Schmidt, R. Schuch, J.F. Babb, L. Spruch, W. Arnold, and A. Noda. First experiments with the Heidelberg test storage ring TSR. *Nucl. Instr. Meth. B*, 43(3):390 – 410, 1989.

[HDK+01] F. Herfurth, J. Dilling, A. Kellerbauer, G. Bollen, S. Henry, H.-J. Kluge, E. Lamour, D. Lunney, R.B. Moore, C. Scheidenberger, et al. A linear radiofrequency ion trap for accumulation, bunching, and emittance improvement of radioactive ion beams. *Nucl. Instr. and Meth. A*, 469(2):254–275, 2001.

[HET06] G. Hampel, K. Eberhardt, and N. Trautmann. The research reactor TRIGA Mainz. *ATW-Int. Z. Kernenergie*, 51:328–330, 2006.

[Hin08] F. Hinterberger. *Physik der Teilchenbeschleuniger und Ionenoptik*. Springer-Verlag Berlin Heidelberg, 2nd edition, 2008.

[HPS+88] C. Habfast, H. Poth, W. Schwab, B. Seligmann, M. Wörtge, A. Wolf, H. Haseroth, C.E. Hill, and J.-L. Vallet. The LEAR electron cooler: Recent improvements and tests. *Physica Scripta*, 1988(T22):277, 1988.

[HS75] T.W. Hänsch and A.L. Schawlow. Cooling of gases by laser radiation. *Opt. Comm.*, 13(1):68 – 69, 1975.

[HSS+11] M. Hobein, A. Solders, M. Suhonen, Y. Liu, and R. Schuch. Evaporative cooling and coherent axial oscillations of highly charged ions in a Penning trap. *Phys. Rev. Lett.*, 106:013002, Jan 2011.

[Hub94] J.D. Huba. NRL Plasma Formulary. Technical report, Plasma Physics Division, Naval Research Laboratory, Washington D.C., 1994.

[IBBW95] W.M. Itano, J.C. Bergquist, J.J. Bollinger, and D.J. Wineland. Cooling methods in ion traps. *Phys. Scr.*, 1995(T59):106, 1995.

[JLPP73] P. Jacquinot, S. Liberman, J.-L. Picqué, and J. Pinard. High resolution spectroscopic application of atomic beam deflection by resonant light. *Opt. Comm.*, 8(2):163 – 165, 1973.

[KAB+11] J. Ketelaer, G. Audi, T. Beyer, K. Blaum, M. Block, R.B. Cakirli, R.F. Casten, C. Droese, M. Dworschak, K. Eberhardt, et al. Mass measurements on stable nuclides in the rare-earth region with the Penning-trap mass spectrometer TRIGA-TRAP. *Phys. Rev. C*, 84(1):014311, 2011.

[Kau76] S.L. Kaufman. High-resolution laser spectroscopy in fast beams. *Opt. Commun.*, 17(3):309–312, 1976.

[Kau13] S. Kaufmann. Spezifikation der Energieunschärfe gekühlter und gepulster Ionenstrahlen mittels Laserspektroskopie. Diploma thesis, Johannes Gutenberg-Universität, Mainz, 2013.

[KBB+08] H.-J. Kluge, T. Beier, K. Blaum, L. Dahl, S. Eliseev, F. Herfurth, B. Hofmann, O. Kester, S. Koszudowski, C. Kozhuharov, G. Maero, W. Nörterhäuser, J. Pfister, W. Quint, U. Ratzinger, A. Schempp, R. Schuch, Th. Stöhlker, R.C. Thompson, M. Vogel, G. Vorobjev, D.F.A. Winters, and G. Werth. Chapter 7 HITRAP: A Facility at GSI for Highly Charged Ions. In S. Salomonson and E. Lindroth, editors, *Current Trends in Atomic Physics*, volume 53 of *Advances in Quantum Chemistry*, pages 83 – 98. Academic Press, 2008.

[KBB+10] J. Ketelaer, T. Beyer, K. Blaum, M. Block, K. Eberhardt, M. Eibach, F. Herfurth, C. Smorra, and Sz. Nagy. Accuracy studies with carbon clusters at the Penning trap mass spectrometer TRIGA-TRAP. *Eur. Phys. J. D*, 58(1):47–52, 2010.

[KBB+12] A. Krieger, K. Blaum, M.L. Bissell, N. Frömmgen, Ch. Geppert, M. Hammen, K. Kreim, M. Kowalska, J. Krämer, T. Neff, R. Neugart, G. Neyens, W. Nörtershäuser, Ch. Novotny, R. Sánchez, and D.T. Yordanov. Nuclear charge radius of ^{12}Be. *Phys. Rev. Lett.*, 108:142501, Apr 2012.

[KBK+95] M. König, G. Bollen, H.-J. Kluge, T. Otto, and J. Szerypo. Quadrupole excitation of stored ion motion at the true cyclotron frequency. *Int. J. Mass Spectrom. Ion Proc.*, 142(1–2):95 – 116, 1995.

[KBW89] F. Kappeler, H. Beer, and K. Wisshak. s-process nucleosynthesis-nuclear physics and the classical model. *Rep. Progr. Phys.*, 52(8):945, 1989.

[KCO01] T. Kinugawa, F.J. Currell, and S. Ohtani. Pulsed evaporative cooling of ion cloud in an electron beam ion trap. *Physica Scripta*, 2001(T92):102, 2001.

[KEH+14] J. Ketter, T. Eronen, M. Höcker, S. Streubel, and K. Blaum. First-order perturbative calculation of the frequency-shifts caused by static cylindrically-symmetric electric and magnetic imperfections of a Penning trap. *Int. J. Mass Spectrom.*, 358(0):1 – 16, 2014.

[Ket10] J. Ketelaer. *The construction of Triga-Trap and direct high-precision Penning trap mass measurements on rare-earth elements and americium.* PhD thesis, Johannes Gutenberg-Universität, Mainz, 2010.

[Kim97] T. Kim. *Buffer Gas Cooling of Ions in a Radio Frequency Quadrupole Ion Guide.* PhD thesis, McGill University, Montreal, Canada, 1997.

[Kin63] W. H. King. Comments on the article "peculiarities of the isotope shift in the samarium spectrum". *J. Opt. Soc. Am.*, 53(5):638–639, May 1963.

[KKB+08] J. Ketelaer, J. Krämer, D. Beck, K. Blaum, M. Block, K. Eberhardt, G. Eitel, R. Ferrer, Ch. Geppert, S. George, et al. TRIGA-SPEC: a setup for mass spectrometry and laser spectroscopy at the research reactor TRIGA Mainz. *Nucl. Instr. and Meth. A*, 594(2):162–177, 2008.

[KKT+79] U. Klingbeil, J. Kowalski, F. Träger, H.-B. Wiegemann, and G. zu Putlitz. Isotope shift and hyperfine structure of ^{43}Ca by laser spectroscopy. *Z. Phys. A*, 290(2):143–148, 1979.

[Kop58] H. Kopfermann. *Nuclear moments*, volume 16. Academic Press, New York, 1958.

[Krä10] J. Krämer. *Construction and Commissioning of a Collinear Laser Spectroscopy Setup at TRIGA Mainz and Laser Spectroscopy of Magnesium Isotopes at ISOLDE (CERN).* PhD thesis, Institut für Kernchemie, Johannes Gutenberg-Universität Mainz, 2010.

[Kre92a] M. Kretzschmar. Excitation of particle motions in a Penning trap: description in the classical canonical formalism. *Phys. Scr.*, 46(6):555, 1992.

[Kre92b] M. Kretzschmar. Single particle motion in a Penning trap: description in the classical canonical formalism. *Phys. Scr.*, 46(6):544, 1992.

[KTM+58] S.L. Koutz, T. Taylor, A. McReynolds, F. Dyson, R.S. Stone, H.P. Sleeper, and R.B. Duffield. *Design of a 10-kW Reactor for Isotope Production, Research and Training Purposes.* Proc. 2nd U.N. Intern. Conf. Peaceful Uses of Atomic Energy, 1958.

[Kul11] P. Kulkarni. *Aerosol Measurement.* John Wiley and Sons, Inc., Hoboken, New Jersey, 3rd edition, 2011.

[LBB+09] Y. Liu, C. Baktash, J. R. Beene, Ch. Geppert, T. Gottwald, C. C. Havener, T. Kessler, H. F. Krause, D. R. Schultz, D. W. Stracener, C. R. Vane, K. Wies, and K. Wendt. Emittance characterization of a hot-cavity laser ion source at Holifield radioactive ion beam facility. *Rev. Sci. Instrum.*, 80(8), 2009.

[LBG+09] M.D. Lunney, C. Bachelet, C. Guénaut, S. Henry, and M. Sewtz. COLETTE: A linear Paul-trap beam cooler for the on-line mass spectrometer MISTRAL. *Nucl. Instr. and Meth. A*, 598(2):379–387, 2009.

[LBM92] D. Lunney, F. Buchinger, and R.B. Moore. The temperature of buffergas cooled ions in a Paul trap. *J. Mod. Opt.*, 39(2):349–360, 1992.

[LBN14] LBNL. *Fission product yields.* Lawrence Berkeley National Laboratory, 2014.

[LCS05] J.M. Luque, M.D. Calzada, and M. Saez. A new procedure for obtaining the Voigt function dependent upon the complex error function. *J. Quant. Spectr. Rad. Transfer*, 94(2):151 – 161, 2005.

[LGR+05] Yu.A. Litvinov, H. Geissel, T. Radon, F. Attallah, G. Audi, K. Beckert, F. Bosch, M. Falch, B. Franzke, M. Hausmann, M. Hellström, Th. Kerscher, O. Klepper, H.-J. Kluge, C. Kozhuharov, K.E.G. Löbner, G. Münzenberg, F. Nolden, Yu.N. Novikov, W. Quint, Z. Patyk, H. Reich, C. Scheidenberger, B. Schlitt, M. Steck, K. Sümmerer, L. Vermeeren, M. Winkler, Th. Winkler, and H. Wollnik. Mass measurement

of cooled neutron-deficient bismuth projectile fragments with time-resolved Schottky mass spectrometry at the FRS-ESR facility. *Nucl. Phys. A*, 756(1–2):3 – 38, 2005.

[LGST06] T. Lamy, R. Geller, P. Sortais, and T. Thuillier. Status of charge breeding with electron cyclotron resonance ion sources. *Rev. Sci. Instrum.*, 77(3):03B101, 2006.

[LK25] I. Langmuir and K.H. Kingdon. Thermionic effects caused by vapours of alkali metals. *Proc. Royal Soc. A*, 107(741):61–79, 1925.

[LLA+05] D. Leitner, C.M. Lyneis, S.R. Abbott, D. Collins, R.D. Dwinell, M.L. Galloway, M. Leitner, and D.S. Todd. Next generation ECR ion sources: First results of the superconducting 28GHz ECRIS-VENUS. *Nucl. Instr. Meth. B*, 235(1):486–493, 2005.

[LM99] M.D. Lunney and R.B. Moore. Cooling of mass-separated beams using a radiofrequency quadrupole ion guide. *Int. J. Mass Spectrom.*, 190:153–160, 1999.

[LMH+88] M.A. Levine, R.E. Marrs, J.R. Henderson, D.A. Knapp, and M.B. Schneider. The electron beam ion trap: A new instrument for atomic physics measurements. *Physica Scripta*, 1988(T22):157, 1988.

[LQG+98] F. Liu, N. Qi, S. Gensler, R.R. Prasad, M. Krishnan, and I.G. Brown. Vacuum arc ion source for heavy ion fusion. *Rev. Sci. Instrum.*, 69(2):819–821, 1998.

[LWY71] G.E. Lee-Whiting and L. Yamazaki. Semi-analytical calculations for circular quadrupoles. *Nucl. Instr. and Meth.*, 94(2):319–332, 1971.

[McL47] Norman W. McLachlan. *Theory and application of Mathieu functions*, volume 4. Oxford U.P., Oxford, 1947.

[McR58] A.W. McReynolds. *Neutron Thermalization by Chemically Bound Hydrogen and Carbon.* U.S. Government Printing Office, 1958.

[MD68] F.G. Major and H.G. Dehmelt. Exchange-collision technique for the rf spectroscopy of stored ions. *Phys. Rev.*, 170(1):91, 1968.

[MDS+88] Naoto Masuhara, John M. Doyle, Jon C. Sandberg, Daniel Kleppner, Thomas J. Greytak, Harald F. Hess, and Greg P. Kochanski. Evaporative cooling of spin-polarized atomic hydrogen. *Phys. Rev. Lett.*, 61:935–938, Aug 1988.

[MGOT69] R.D. MacFarlane, R.A. Gough, N.S. Oakey, and D.F. Torgerson. The helium-jet recoil transport method. *Nucl. Instr. and Meth.*, 73(3):285 – 291, 1969.

[MGW05] F.G. Major, V.N. Gheorghe, and G. Werth. *Charged Particle Traps*. Springer Series on Atomic, Optical, and Plasma Physics, vol. 37, Springer, Berlin, 2005.

[Mon02] C. Monroe. Quantum information processing with atoms and photons. *Nature*, 416(6877):238–246, 2002.

[Moo93] R.B. Moore. The manipulation of charged particles into and out of electromagnetic traps. *Hyperfine Interact.*, 81(1-4):45–70, 1993.

[MS79] V.G. Minogin and O.T. Serimaa. Resonant light pressure forces in a strong standing laser wave. *Opt. Comm.*, 30(3):373 – 379, 1979.

[MTMS93] Y. Moriwaki, M. Tachikawa, Y. Maeno, and T. Shimizu. Laser spectroscopic study of dynamics of laser-cooled ions in paul trap. *AIP Conf. Proc.*, 290(1):38–39, 1993.

[MWK+80] A.K. Mazumdar, H. Wagner, G. Krömer, W. Walcher, M. Brügger, E. Stender, N. Trautmann, and T. Lund. The on-line isotope separation facility HELIOS at the Mainz reactor. *Nucl. Instr. and Meth.*, 174(1):183–188, 1980.

[MWWL76] A.K. Mazumdar, H. Wagner, W. Walcher, and T. Lund. Connection experiments with a hollow cathode ion source and a helium gas jet system for on-line isotope separation. *Nucl. Instr. Meth.*, 139(0):319 – 323, 1976.

[NBI+98] W. Nörtershäuser, K. Blaum, K. Icker, P. Müller, A. Schmitt, K. Wendt, and B. Wiche. Isotope shifts and hyperfine structure in the transitions in calcium II. *Eur. Phys. J. D*, 2(1):33–39, 1998.

[NC10] M.A. Nielsen and I.L. Chuang. *Quantum Computation and Quantum Information: 10th Anniversary Edition*. Cambridge University Press, 2010.

[NCB+02] A. Nieminen, P. Campbell, J. Billowes, D.H. Forest, J.A.R. Griffith, J. Huikari, A. Jokinen, I.D. Moore, R. Moore, G. Tungate, et al. On-line ion cooling and bunching for collinear laser spectroscopy. *Phys. Rev. Lett.*, 88(9):094801, 2002.

[New61] H.W. Newson. Symmetric and asymmetric fission. *Phys. Rev.*, 122:1224–1226, May 1961.

[NG14] W. Nörtershäuser and C. Geppert. Nuclear charge radii of light elements and recent developments in collinear laser spectroscopy. In *The Euroschool on Exotic Beams, Vol. IV*, volume 879 of *Lecture Notes in Physics*, pages 233–292. Springer Berlin Heidelberg, 2014.

[NHTD78] W. Neuhauser, M. Hohenstatt, P. Toschek, and H. Dehmelt. Optical-sideband cooling of visible atom cloud confined in parabolic well. *Phys. Rev. Lett.*, 41:233–236, Jul 1978.

[Nie12] B. Nießen. Entwicklung einer Plasma-Ionenquelle für radioaktive Isotope und Implementierung und Inbetriebnahme einer offline Ionenquelle am TRIGA-Reaktor. Diploma thesis, Institut für Kernchemie, Johannes Gutenberg-Universität Mainz, 2012.

[NMRW58] M. Nelkin, A.W. McReynolds, M. Rosenbluth, and W. Whittemore. *Neutron Thermalization by Chemically Bound Hydrogen*, volume 16. Proc. 2nd U.N. Intern. Conf. Peaceful Uses of Atomic Energy, 1958.

[Nör10] W. Nörterhäuser. Recent developments in collinear laser spectroscopy at COLLAPS/ISOLDE. *Hyperfine Interact.*, 198(1-3):73–83, 2010.

[NS70] L.C. Northcliffe and R.F. Schilling. Range and stopping-power tables for heavy ions. *At. Data Nucl. Data Tables*, 7(3–4):233 – 463, 1970.

[NSE+11] W. Nörtershäuser, R. Sánchez, G. Ewald, A. Dax, J. Behr, P. Bricault, B.A. Bushaw, J. Dilling, M. Dombsky, G.W.F. Drake, S. Götte, H.-J. Kluge, Th. Kühl, J. Lassen, C.D.P. Levy, K. Pachucki, M. Pearson, M. Puchalski, A. Wojtaszek, Z.-C. Yan, and C. Zimmermann. Isotope-shift measurements of stable and short-lived lithium isotopes for nuclear-charge-radii determination. *Phys. Rev. A*, 83:012516, Jan 2011.

[OKN+03] N. Oshima, T.M. Kojima, M. Niigaki, A. Mohri, K. Komaki, Y. Iwai, and Y. Yamazaki. Development of a cold HCI source for ultra-slow collisions. *Nucl. Instr. Meth. B*, 205(0):178 – 182, 2003. 11th International Conference on the Physics of Highly Charged Ions.

[PBB+84] C.W.P. Palmer, P.E.G. Baird, S.A. Blundell, J.R. Brandenberger, C.J. Foot, D.N. Stacey, and G.K. Woodgate. Laser spectroscopy of calcium isotopes. *J. Phys. B*, 17(11):2197, 1984.

[PBL+91] B. M. Penetrante, J. N. Bardsley, M. A. Levine, D. A. Knapp, and R. E. Marrs. Evaporative cooling of highly charged dysprosium ions in an enhanced electron-beam ion trap. *Phys. Rev. A*, 43:4873–4882, May 1991.

[PM82] W.D. Phillips and H. Metcalf. Laser deceleration of an atomic beam. *Phys. Rev. Lett.*, 48:596–599, Mar 1982.

[Pot90] H. Poth. Electron cooling: theory, experiment, application. *Phys. Rep.*, 196(3):135–297, 1990.

[PS53] W. Paul and H. Steinwedel. Ein neues Massenspektrometer ohne Magnetfeld. *Z. Natur A*, 8:448, 1953.

[QW07] Y.-Z. Qian and G.J. Wasserburg. Where, oh where has the r-process gone? *Phys. Rep.*, 442(1-6):237 – 268, 2007. The Hans Bethe Centennial Volume 1906-2006.

[Ram90] N.F. Ramsey. Experiments with separated oscillatory fields and hydrogen masers. *Science*, 248(4963):1612–1619, 1990.

[RBN+10] D. Rodríguez, K. Blaum, W. Nörtershäuser, M. Ahammed, A. Algora, G. Audi, J. Äystö, D. Beck, M. Bender, J. Billowes, M. Block, C. Böhm, G. Bollen, M. Brodeur, T. Brunner, B.A. Bushaw, R.B. Cakirli, P. Campbell, D. Cano-Ott, G. Cortés, J. Crespo López-Urrutia, P. Das, A. Dax, A. De, P. Delheij, T. Dickel, J. Dilling, K. Eberhardt, S. Eliseev, S. Ettenauer, K.T. Flanagan, R. Ferrer, J.-E. García-Ramos, E. Gartzke, H. Geissel, S. George, C. Geppert, M.B. Gómez-Hornillos, Y. Gusev, D. Habs, P.-H. Heenen, S. Heinz, F. Herfurth, A. Herlert, M. Hobein, G. Huber, M. Huyse, C. Jesch, A. Jokinen, O. Kester, J. Ketelaer, V. Kolhinen, I. Koudriavtsev, M. Kowalska, J. Krämer, S. Kreim, A. Krieger, T. Kühl, A.M. Lallena, A. Lapierre, F. Le Blanc, Y.A. Litvinov, D. Lunney, T. Martínez, G. Marx, M. Matos, E. Minaya-Ramirez, I. Moore, S. Nagy, S. Naimi, D. Neidherr, D. Nesterenko, G. Neyens, Y.N. Novikov, M. Petrick, W.R. Plaß, A. Popov, W. Quint, A. Ray, P.-G. Reinhard, J. Repp, C. Roux, B. Rubio, R. Sánchez, B. Schabinger, C. Scheidenberger, D. Schneider, R. Schuch, S. Schwarz, L. Schweikhard, M. Seliverstov, A. Solders, M. Suhonen, J. Szerypo, J.L. Taín, P.G. Thirolf, J. Ullrich, P. Van Duppen, A. Vasiliev, G. Vorobjev, C. Weber, K. Wendt, M. Winkler, D. Yordanov, and F. Ziegler. MATS and LaSpec: High-precision experiments using ion traps and lasers at FAIR. *Eur. Phys. J. Special Topics*, 183(1):1–123, 2010.

[RDP89] N. Ramsey, G. Dehmelt, and W. Paul. The Nobel Prize in Physics 1989, 1989.

[Ren15] D. Renisch. *Development of a high-temperature surface ion source for the online coupling of TRIGA-SPEC to the TRIGA Mainz research reactor*. PhD thesis, Institut für Kernchemie, Johannes Gutenberg-Universität Mainz, 2015.

[RPC+87] E. L. Raab, M. Prentiss, Alex Cable, Steven Chu, and D. E. Pritchard. Trapping of neutral sodium atoms with radiation pressure. *Phys. Rev. Lett.*, 59:2631–2634, Dec 1987.

[SAB+01] H. Schatz, A. Aprahamian, V. Barnard, L. Bildsten, A. Cumming, M. Ouellette, T. Rauscher, F.-K. Thielemann, and M. Wiescher. End point of the *rp* process on accreting neutron stars. *Phys. Rev. Lett.*, 86:3471–3474, Apr 2001.

[SBB+91] G. Savard, S. Becker, G. Bollen, H.-J. Kluge, R.B. Moore, T. Otto, L. Schweikhard, H. Stolzenberg, and U. Wiess. A new cooling technique for heavy ions in a Penning trap. *Phys. Lett. A*, 158(5):247–252, 1991.

[SBB+04] M. Steck, P. Beller, K. Beckert, B. Franzke, and F. Nolden. Electron cooling experiments at the ESR. *Nucl. Instr. Meth. A*, 532(1-2):357 – 365, 2004. International Workshop on Beam Cooling and Related Topics.

[SBB+12] C. Smorra, T. Beyer, K. Blaum, M. Block, Ch. E. Düllmann, K. Eberhardt, M. Eibach, S. Eliseev, Sz. Nagy, W. Nörtershäuser, and D. Renisch. Direct mass measurements of cadmium and palladium isotopes and their double-β transition Q-values. *Phys. Rev. C*, 85:027601, Feb 2012.

[Sch98] S. Schwarz. *Manipulation radioaktiver Ionenstrahlen mit Hilfe einer Paulfalle und direkte Massenmessungen an neutronenarmen Quecksilberisotopen mit dem ISOLTRAP-Experiment.* PhD thesis, Johannes Gutenberg-Universität Mainz, 1998.

[Sch06] F. Schwabl. *Statistische Mechanik.* Springer, 2006.

[Sch07] F. Scheck. *Theoretische Physik 1.* Springer, 8th edition, 2007.

[Sch15] F. Schneider. *Massenmessung und Isotopenseparation von ^{163}Ho für die ECHo Kollaboration.* Phd thesis, Institut für Physik, Johannes Gutenberg-Universität Mainz, 2015.

[SD56] L.G. Smith and C.C. Damm. Mass synchrometer. *Rev. Sci. Instrum.*, 27(8):638–649, 1956.

[SKK+00] C.A. Sackett, D. Kielpinski, B.E. King, C. Langer, V. Meyer, C.J. Myatt, M. Rowe, Q.A. Turchette, W.M. Itano, D.J. Wineland, et al. Experimental entanglement of four particles. *Nature*, 404(6775):256–259, 2000.

[Smo08] C. Smorra. Setup of a carbon-cluster laser ion source for high-precision mass spectrometry. Diploma thesis, Institut für Physik, Johannes Gutenberg-Universität Mainz, 2008.

[Smo12] C. Smorra. *High-precision Q-value and mass measurements for neutrino physics with TRIGA-TRAP and commissioning of an on-line ion*

source for TRIGA-SPEC. PhD thesis, Combined Faculties for the Natural Sciences and for Mathematics of the Ruperto-Carola-University of Heidelberg, Germany, 2012.

[SNBT86] Th. Sauter, W. Neuhauser, R. Blatt, and P. E. Toschek. Observation of quantum jumps. *Phys. Rev. Lett.*, 57:1696–1698, Oct 1986.

[Spi56] L. Spitzer. *Physics of Fully Ionized Gases*. Number 100 in 1. Interscience Publishers Inc., New York, 1956.

[Ste86] S. Stenholm. The semiclassical theory of laser cooling. *Rev. Mod. Phys.*, 58:699–739, Jul 1986.

[STH80] E. Stender, N. Trautmann, and G. Herrmann. Use of alkali halide clusters in a gas-jet recoil-transport system. *Radiochem. Radioanal. Lett.*, 42:291–296, 1980.

[Str92] P. Strehl. Beam diagnostics. *Rev. Sci. Instrum.*, 63(4):2652–2659, 1992.

[SVNL91] R.E. Silverans, L. Vermeeren, R. Neugart, and P. Lievens. Hyperfine structure constants of the Ca II states $4S^2S_{1/2}$ and $4S^2P_{1/2,3/2}$ and the nuclear quadrupole moment of ^{43}Ca. *Z. Phys. D*, 18(4):351–356, 1991.

[SWW72] R. Schieder, H. Walther, and L. Wöste. Atomic beam deflection by the light of a tunable dye laser. *Opt. Comm.*, 5(5):337 – 340, 1972.

[TG89] J. Tan and G. Gabrielse. One electron in an orthogonalized cylindrical Penning trap. *Appl. Phys. Lett.*, 55(20):2144–2146, 1989.

[TGA+04] C. Travaglio, R. Gallino, E. Arnone, J. Cowan, F. Jordan, and C. Sneden. Galactic evolution of Sr, Y, and Zr: A multiplicity of nucleosynthetic processes. *Astrophys. J.*, 601(2):864, 2004.

[TWM80] J.F.J. Todd, R.M. Waldren, and R.E. Mather. The quadrupole ion store (quistor) part IX: space-charge and ion stability. a theoretical background and experimental results. *Int. J. Mass Spectrom. Ion Phys.*, 34(3-4):325 – 349, 1980.

[VAVB83] F. Vedel, J. André, M. Vedel, and G. Brincourt. Computed energy and spatial statistical properties of stored ions cooled by a buffer gas. *Phys. Rev. A*, 27:2321–2330, May 1983.

[WD75] D.J. Wineland and H. Dehmelt. Proposed 10^{14} $\delta\nu/\nu$ laser fluorescence spectroscopy on Tl^+ mono-ion oscillator III (side band cooling). *Bull. Am. Phys. Soc.*, 20(4):637–637, 1975.

[WDW78] D.J. Wineland, R.E. Drullinger, and F.L. Walls. Radiation-pressure cooling of bound resonant absorbers. *Phys. Rev. Lett.*, 40:1639–1642, Jun 1978.

[WIBH87] D.J. Wineland, W.M. Itano, J.C. Bergquist, and R.G. Hulet. Laser-cooling limits and single-ion spectroscopy. *Phys. Rev. A*, 36:2220–2232, Sep 1987.

[WIVDJ83] D.J. Wineland, W.M. Itano, and R.S. Van Dyck Jr. High-resolution spectroscopy of stored ions. *Adv. Atomic Mol. Phys*, 19:135, 1983.

[Wiz79] J.L. Wiza. Microchannel plate detectors. *Nucl. Instr. Meth.*, 162(1–3):587 – 601, 1979.

[WLD+78] H. Wohlfarth, W. Lang, H. Dann, H.-G. Clerc, K.-H. Schmidt, and H. Schrader. The ionic charge distribution of fission products and the influence of internal conversion on highly preionized heavy ions. *Z. Phys. A*, 287(2):153–163, 1978.

[WLL01] D. Wutte, M.A. Leitner, and C.M. Lyneis. Emittance measurements for high charge state ion beams extracted from the AECR-U ion source. *Phys. Scr.*, 2001(T92):247, 2001.

[WLL03] F. Wenander, J. Lettry, and M. Lindroos. Transverse emittance investigation of the ISOLDE target-ion sources. *Nucl. Instr. Meth. B*, 204:261–266, 2003.

[Wol76] H. Wollnik. Principles behind a he-jet system and its application for isotope separation. *Nucl. Instr. and Meth.*, 139(0):311 – 318, 1976.

[Wol87] H. Wollnik. *Optics of Charged Particles*. Academic Press, Inc., 1987.

[Wol88] A. Wolf. Electron cooling of stored ions. *Phys. Scr.*, 1988(T22):55, 1988.

[Wol95] B. Wolf. *Handbook of ion sources*. CRC Press, Boca Raton [u.a.], 1995.

[WW86] S.E. Woosley and T.A. Weaver. The physics of supernova explosions. *Ann. Rev. Astron. Astrophys.*, 24:205–253, 1986.

[YWGS04] K. Yu, L. Wu, B. Gou, and T. Shi. Calculation of the hyperfine structure constants in $^{43}Ca^{+}$ and $^{87}Sr^{+}$. *Phys. Rev. A*, 70:012506, Jul 2004.

[ZSW+02] X. Zhang, K.A. Smith, D.R. Worsnop, J. Jimenez, J.T. Jayne, and C.E. Kolb. A numerical characterization of particle beam collimation by an aerodynamic lens-nozzle system: Part I. an individual lens or nozzle. *Aerosol Sci. Technol.*, 36(5):617–631, 2002.

[ZSW+04] X. Zhang, K.A. Smith, D.R. Worsnop, J.L. Jimenez, J.T. Jayne, C.E. Kolb, J. Morris, and P. Davidovits. A numerical characterization of particle beam collimation: Part II. integrated aerodynamic-lens-nozzle system. *Aerosol Sci. Technol.*, 38(6):619–638, 2004.

[Zud86] F. Zude. Transportverhalten von Spaltprodukten in Gasjetsystemen. Diploma thesis, Johannes Gutenberg-Universität, Mainz, 1986.

[ZXX+10] W.L. Zhan, H.S. Xu, G.Q. Xiao, J.W. Xia, H.W. Zhao, and Y.J. Yuan. Progress in HIRFL-CSR. *Nucl. Phys. A*, 834(1-4):694c – 700c, 2010. The 10th International Conference on Nucleus-Nucleus Collisions (NN2009).

Acknowledgements

I want to thank my supervisor Prof. Klaus Blaum who gave me the opportunity to prepare a thesis in his very exciting research field. His enthusiasm for physics as well as his support for his many students are clearly outstanding. Also, I truly appreciate the offer of Priv.-Doz. José Crespo to jump in as a referee in the last minute.

A big thank goes to all of my colleagues at the TRIGA-SPEC experiment in Mainz. Thank you CS, Dennis, Martin, and Szilard for your helping hands when tons of devices, vacuum chambers, equipment, and cables had to be installed at the experimental site. Thank you Christian, Simon, and Michael for running the laser spectroscopy setup during the characterization of the RFQ cooler and buncher. My gratitude also goes to Wilfried, Christoph, Klaus E., Christopher, Jessica, Fabian, Andreas, Elisa, Nadja, and Benjamin for their support and cooperation in setting up the common beam line. The ideas and expertise of Michael Block and Frank Herfurth from GSI helped a lot for the optimization of the RFQ cooler and buncher.

I appreciate the work of the people of the numerous workshops that were involved in my project through the manufacturing of many parts: I thank Siegbert Felzer from the workshop of the Institute for Physics for high-precision ion optics, Ulli Krille from the workshop of the Institute of Nuclear Chemistry for quick and clean machining, the workshop at GSI for the detector train, and the workshop at MPI-K in Heidelberg for the high-voltage safety system. Especially, I want to thank Mr. Bueckart and his team from the workshop of the MPI-C in Mainz for milling the slit chamber with its many custom connectors (Fig. 2.10) from an 0.5 t solid aluminum block. I also appreciate the help from the electrical workshop and all the other members of the Institute of nuclear chemistry.

I am indebted to David Lunney from CSNSM for donating the former MISTRAL ion beam cooler COLETTE to TRIGA-SPEC and for his help during its shipping from CERN to Mainz, as well as for his continuous support afterward.

During the time of my thesis, many group members became my friends. The time on the soccer field, the endless laps at the Run for Children, the evening discussions at the annual MATS Days, or the Doppelkopf sessions (with w.r.) created a very enjoyable atmosphere in the MATS group during working hours and beyond.

Last but not least I want to express my gratitude to my family and my friends for their everlasting support and encouragement. Thank you, Annemarie, for the love we share and your understanding in times of need.

Erklärung

Hiermit erkläre ich, Thomas Beyer, dass ich diese Arbeit selbst verfasst habe und ausschließlich die angegebenen Quellen verwendet habe.

Heidelberg, den 08.10.2014
Thomas Beyer